

**SPATIAL AND TEMPORAL PROCESSING FOR A COMPACT  
LANDMINE DETECTION RADAR**

**by**

**GURUVAYURAPPAN**

B.E., Electronics and Communication Engineering

MVSR Engineering College, Osmania University

Hyderabad, India - 2000

Submitted to the Department of Electrical Engineering and Computer  
Science and the Faculty of the Graduate School of the University of Kansas  
in partial fulfillment of the requirements for the degree of  
Master of Science

Thesis Committee:

---

James Stiles: Chairperson

---

Christopher Allen

---

Glenn Prescott

Date of Defense: October 29, 2002

## **Acknowledgements**

I would like to thank my advisor Dr. James Stiles for giving me the opportunity to work on this project and guiding me all throughout my studies at The University of Kansas. Thank you! Dr. Stiles, for guiding me towards being the engineer I am today. I would like to thank Dr. Christopher Allen and Dr. Glenn Prescott for accepting to be on my committee. I take this opportunity to thank Ms. Donnis Graham, RSL Office Manager, for helping me with any problems I encountered in RSL and for patiently editing my thesis.

I thank my parents, K. Vasudevan and Prabha Vasudevan, grandparents, P.R. Desikan and Padma Desikan, sisters, Pratibha and Priya, and brothers in law, Sekhar and Murali, for being with me all through my life with their love, guidance and encouragement. I extend a special note of thanks to Murali and Priya, as they have been of great help to me when I came to pursue higher education in America.

I thank all my friends in Lawrence for the wonderful time I spent with them, which I will cherish for the rest of my life. I take this opportunity to thank two of my good friends, Sunil and Arun, for their help and encouragement during my studies at the University of Kansas. I thank Beng Beh, James Kreycik, Nathan Goodman and Travis Olson for helping me with my work at RSL.

Last but never the least I thank God for all the things that have come my way in life.

# TABLE OF CONTENTS

<b>ABSTRACT</b> .....	<b>xi</b>
<b>1. INTRODUCTION AND MOTIVATION</b> .....	<b>1</b>
1.1 RESEARCH IN LANDMINE DETECTION .....	2
1.2 GPR IN LANDMINE DETECTION .....	5
1.2.1 Our Approach.....	6
<b>2. DEVELOPMENT OF DETECTION SCHEME</b> .....	<b>10</b>
2.1 CONCEPT OF SYMMETRY .....	11
2.2 GPR AND SYMMETRY FOR LANDMINE DETECTION .....	14
2.3 MATHEMATICAL REPRESENTATION OF MEASUREMENTS .....	16
2.4 SYMMETRY MEASURE .....	18
2.4.1 Confidence Level in Target Classification .....	20
2.4.2 Decision Threshold .....	21
<b>3. SYSTEM SPECIFICATIONS AND INITIAL EXPERIMENTS</b> .....	<b>23</b>
3.1 SYSTEM SPECIFICATIONS .....	23
3.2 INITIAL EXPERIMENTS IN SANDPIT .....	26
<b>4. SIMULATING A HAND-HELD DETECTOR</b> .....	<b>32</b>
4.1 SENSOR HAND-HELD MODEL .....	32
4.2 DATA COLLECTION SCHEME.....	37
4.2.1 Simulating Multiple Sensor Geometry Hand-Held Detector.....	40
4.2.2 Data Collection System.....	45
4.3 ANALYSIS OF DATA COLLECTED .....	47
<b>5. EXPERIMENTS AND RESULTS</b> .....	<b>51</b>
5.1 DATA PROCESSING .....	51
5.2 EXPERIMENTS AND RESULTS .....	53
5.2.1 Experiments in Sandpit.....	53
5.2.2 Results from Field Experiment .....	65
5.3 SENSOR ARRAY .....	70
5.3.1 Cascade Plots .....	73
5.4 MATCHED FILTER FOR SUBSURFACE TARGET DETECTION.....	91
<b>6. MINIMUM MEAN-SQUARED ERROR GPR PROCESSOR</b> .....	<b>94</b>
6.1 BACKGROUND AND MOTIVATION .....	95
6.2 RADAR RESPONSE MODEL .....	98
6.3 MMSE ESTIMATOR .....	100
6.4 SIMULATION AND RESULTS.....	103
6.4.1 Simulation Model.....	103
6.4.2 Simulation Results .....	106

6.5 RESULTS ON MEASURED DATA.....	111
<b>7. KALMAN FILTER IMPLEMENTATION .....</b>	<b>116</b>
7.1 KALMAN FILTER MODEL .....	116
7.1.1 Fundamentals of Kalman Filter Algorithm.....	117
7.1.2 Kalman Filter Implementation.....	118
7.2 SIMULATION AND RESULTS.....	121
7.2.1 Simulation Model.....	121
7.2.2 Simulation Results .....	123
7.3 KALMAN FILTER PROCESSING ON MEASURED DATA .....	129
<b>8. CONCLUSIONS AND FUTURE WORK.....</b>	<b>134</b>
8.1 SUMMARY .....	134
8.2 SUGGESTED FUTURE WORK.....	135
8.3 CONCLUSIONS.....	136
<b>REFERENCES.....</b>	<b>138</b>

# List of Figures

Figure 1.2.1.1: Pictures of anti-personnel landmine and a natural clutter target, rock..... 6

Figure 2.1.1: Examples to illustrate reflection symmetry: (a) shows an object that exhibits reflection symmetry about the plane XY; (b) illustrates an object that exhibits reflection symmetry about the plane  $X^1Y^1$ ..... 12

Figure 2.1.2: Examples of objects exhibiting rotational symmetry, (a), and a combination of rotational and reflection symmetry, (b). ..... 13

Figure 2.2.1: Diagram explaining the concept of mirrored bistatic observation pairs. The figure also indicates the target reflection symmetric plane..... 14

Figure 3.2.1: Picture of the Styrofoam disc used to simulate a mine in the sandpit experiments. 27

Figure 3.2.2: Mirrored bistatic observation pair used to collect measurements in the sandpit on the Styrofoam disc. .... 28

Figure 3.2.3: Real part of scattering profile for ground and ground + target (the target being the symmetric Styrofoam disc)..... 29

Figure 3.2.4: Real and imaginary parts of the complex scattering for the mirrored bistatic observation shown in Figure 3.2.2. The scattering for bistatic measurement  $T_X^1-R_X^1$  is shown in red and the one for  $T_X^2-R_X^2$  is shown in blue. .... 30

Figure 4.1.1: A model for a single sensor geometry hand-held landmine detector that collects data by performing a single scan..... 33

Figure 4.1.2: A model for a multiple sensor geometry hand-held detector. Each color indicates a different sensor geometry. Each sensor geometry has a pair of bistatic measurements..... 36

Figure 4.2.1: A one-dimensional scan to collect the measurements to the left of the plane MP in Figure 4.1.2 using a single bistatic measurement,  $T_X-R_X$ . .... 38

Figure 4.2.2: A one-dimensional scan to collect the measurements to the right of the plane MP in Figure 4.1.2 using a single bistatic measurement,  $T_X-R_X$ . .... 39

Figure 4.2.1.1: Reconstructing multiple sensor geometries for a single measurement plane. In other words, using the data collection scheme the multiple sensor geometry hand-held detector can be synthesized..... 42

Figure 4.2.1.2: Figure explaining the number of sensor geometries as a function of measurement plane. The scans performed collect N data points. The value of v ranges from  $-N$  to N (indication of measurement plane) and a maximum of N sensor geometries can be synthesized for the measurement plane, 0. .... 43

Figure 4.2.1.3: A single sensor geometry that has multiple measurement planes is similar to the single sensor geometry hand-held detector described in Section 4.1.1.....	44
Figure 4.2.2.1: Mobile machine used to collect data by implementing the scans detailed in Figures 4.2.1 and 4.2.2 and thereby simulate the hand-held detector.....	46
Figure 4.3.1: A diagrammatic representation of either the sum or $m$ value matrices for a few measurements collected using the two scans in Figures 4.2.1 and 4.2.2. The black cells indicate all the possible sensor geometries for all the measurement planes. The cells color coded as gray are obtained by performing a linear interpolation. The interpolation makes the matrices continuous.....	49
Figure 5.2.1.1: Picture of the Styrofoam disc used to simulate a symmetric landmine in the sandpit experiments.....	53
Figure 5.2.1.2: Picture of a crushed milk jug used to simulate a clutter target in the sandpit experiment.....	54
Figure 5.2.1.3(a): Sum plot for the Styrofoam disc with the indication of an approximate location of target based on the energy scattered from the subsurface target.....	56
Figure 5.2.1.3(b): $m$ plot for the Styrofoam disc with indication of the measurement plane that has low $m$ values for almost all sensor geometries. Hence the target can be classified as a symmetric target. ....	57
Figure 5.2.1.4(a): Sum plot for crushed milk jug is shown in (a). Indicated on the sum plot is approximate location of the target. $m$ plot for crushed milk jug is shown in (b). Note absence of measurement plane with low symmetry measures for all sensor geometries.....	59
Figure 5.2.1.5 (a): A sensor geometry for which the symmetry measure is very low for all the measurement planes irrespective of whether the subsurface target is a mine or clutter. (b) The sensor geometry depicted in (a) with $T_X-R_X$ replaced with its reciprocal measurement. ....	60
Figure 5.2.1.6: Sensor geometry for which $m$ coefficient is small only when the measurement plane aligns with plane of target symmetry and the subsurface target is symmetric. ....	61
Figure 5.2.1.7: Sensor geometry as described in Figure 5.2.1.6 with $T_X-R_X$ replaced with its reciprocal measurement. ....	62
Figure 5.2.1.8: Picture of a rock used in laboratory to simulate natural clutter targets in the sandbox experiments. ....	63
Figure 5.2.1.9: Sum and $m$ plots for rock and Styrofoam disc. By comparing the $m$ plots for the rock and Styrofoam disc, it can be seen that the rock can be classified as an asymmetric target and the Styrofoam disc can be classified as symmetric target.....	64
Figure 5.2.2.1: PMA-3 an anti-personnel mine on which data were collected during field experiment at Ft. A.P. Hill, Virginia. Reproduced from [8].....	66

- Figure 5.2.2.2 (a): Sum plot for PMA-3. Indicated on the plot is the approximate location of the subsurface target. (b)  $m$  plot for PMA-3. Measurement plane shows low symmetry measures for almost all sensor geometries. This is an indicator that the subsurface target is a landmine. .... 67
- Figure 5.2.2.3(a): Sum plot for irregular wood, a natural clutter target. Approximate location of the target is indicated in sum plot. (b)  $m$  plot for irregular wood. There is no measurement plane with low  $m$  values for almost all the sensor geometries. .... 69
- Figure 5.3.1: Sum plots for different numbers of elements in the sensor array for target VAL-69. The sum plot with 16 elements in the sensor array detects the target with a high level of confidence. .... 71
- Figure 5.3.2  $m$  plots for different numbers of elements in the sensor array for target VAL-69... 72
- Figure 5.3.1.1(a): Sum plot for the Styrofoam disc using a sensor array with eight elements. Presence of high sum values indicated by dark red and high value pixels. (b)  $m$  plot for Styrofoam disc. Very low symmetry measures seen around measurement plane in region-5 to 5. (c) Cascade plot for sum value matrix. Presence of subsurface target confirmed by huge peak in cascade plot for sum values. (d) Cascade plot for  $m$  value matrix. The target is symmetric as cascade plot for  $m$  values indicates a deep null in the plane shown in the figure. .... 75
- Figure 5.3.1.2(a): Sum plot for the rock using a sensor array with eight elements. Presence of high sum values indicated by dark red and high value pixels. (b)  $m$  plot for rock. Absence of measurement plane with low symmetry measures for almost all sensor geometries indicates subsurface target is asymmetric. (c) Cascade plot for sum value matrix. Presence of subsurface target confirmed by huge peak in cascade plot for sum values (d) Cascade plot for  $m$  value matrix. The null, which was present for the symmetric target, is missing. Therefore subsurface target is asymmetric. .... 77
- Figure 5.3.1.3(a): Sum plot for the crushed milk jug using a sensor array with eight elements. Presence of high sum values indicated by dark red and high value pixels. (b)  $m$  plot for crushed milk jug showing absence of distinct measurement plane with low symmetry measures for almost all sensor geometries. (c) Cascade plot for sum value matrix. Presence of subsurface target confirmed by huge peak in the cascade plot for sum values. (d) Cascade plot for  $m$  value matrix. Some nulls can be seen in cascade plot (shown by arrows in (d)), but they are not deep and also null does not exist for all sensor geometries. .... 79
- Figure 5.3.1.4 (a): Sum plot for PMA-3 using a sensor array with eight elements. Presence of high sum values indicated by dark red pixels and location of target indicated by white dotted line. (b)  $m$  plot for PMA-3. Very low symmetry measures in  $m$  plot indicated on the plot, classifying the target as symmetric object. (c) Cascade plot for sum value matrix for PMA-3. The cascade plot shows peak indicating presence of subsurface target. (d) Cascade plot for  $m$  value matrix shows deep null in the measurement plane. .... 81
- Figure 5.3.1.5 (a): Sum plot for VAL-69 using a sensor array with eight elements. Presence of high sum values indicated by dark red pixels. Location of target indicated by white dotted line. (b)  $m$  plot for VAL-69. Very low symmetry measures in  $m$  plot indicated on plot, classifying the target as symmetric object. (c) Cascade plot for sum value matrix for VAL-

69. The cascade plot shows peak indicating presence of subsurface target. (d) Cascade plot for $m$ value matrix shows deep null in the measurement plane. ....	83
Figure 5.3.1.6 (a): Sum plot for M-14 using a sensor array with eight elements. Presence of high sum values indicated by dark red pixels. Location of target indicated by white dotted line. (b) $m$ plot for M-14. The $m$ plot is completely blue! Is the target symmetric? (c) Cascade plot for sum value matrix for M-14. The cascade plot shows peak indicating presence of subsurface target. (d) Cascade plot for $m$ value matrix shows measurement plane with a null. The maximum $m$ value for all measurements on this target is less than 0.2, which is quite low.....	85
Figure 5.3.1.7 (a): Sum plot for irregular wood using a sensor array with eight elements. Presence of high sum values indicated by dark red pixels. Location of target indicated by white dotted line. (b) $m$ plot for irregular wood. There is no distinct measurement plane for which almost all $m$ values are low. (c) Cascade plot for sum value matrix for irregular wood. The cascade plot shows peak indicating presence of subsurface target. (d) Cascade plot for $m$ value matrix shows no measurement plane with low $m$ values for many sensor geometries.....	87
Figure 5.3.1.8 (a): Sum plot for TM-46 using a sensor array with eight elements. Presence of high sum values indicated by dark red pixels. Location of target indicated by white dotted line. (b) $m$ plot for TM-46. Measurement planes are shown in which $m$ values range from low to high. (c) Cascade plot for sum value matrix for TM-46. The cascade plot shows peak indicating presence of subsurface target. (d) Cascade plot for $m$ value matrix does not show deep null.....	89
Figure 5.4.1: Scattering as a function of time generated using matched filter. The ground is at a delay of 2.2 ns and the subsurface target is at a delay of 6.5 ns. ....	91
Figure 5.4.2: Scattering as a function of time generated using matched filter. The ground is at a delay of 2.2 ns and the subsurface target is at a delay of 2.75 ns. The time-domain side lobes of the dominant scatterer mask the subsurface target.....	92
Figure 6.1.1: Simulation results with Hamming and Blackman windows to reduce the time-domain side lobe problem. The main lobe widens and masks the subsurface target.....	96
Figure 6.2.1: The targets illuminated by the radar are considered as different layers separated by $\Delta\tau$ , the time resolution. $T_X-R_X$ is the bistatic radar measurement. ....	98
Figure 6.4.2.1: Comparison of performance of MMSE GPR processor and matched filter on subsurface target buried at a depth that corresponds to a delay of 3 ns. The ground is at a delay of 2.2 ns. ....	107
Figure 6.4.2.2: Filter response for MMSE filter (in blue) and matched filter (in red). (a) For a target at a delay of 3.9 ns and (b) for a target at a delay of 2.75 ns. ....	109
Figure 6.4.2.3: Comparison of MMSE (in blue) and matched filter (in red) response when the subsurface target is at very shallow depths (2.75 ns). ....	110

Figure 6.5.1: TM-46 anti-tank mine, a target from the field experiment in Ft. A.P. Hill, Virginia. Reproduced from [8]. .....	112
Figure 6.5.2: MMSE GPR and matched-filter responses for TM-46, anti-tank mine. The target seems to be present at a delay equal to 4.5 ns.....	114
Figure 7.1.2.1: Iterative algorithm for Kalman filter processing.....	120
Figure 7.2.2.1: Results of Kalman filter processing as a function of numbers of iterations. The number of frequency point in a single radar data segment changes with the number of iterations. Optimum number of data points in the radar data is 1.....	125
Figure 7.2.2.2: Performance of Kalman filter compared to matched filter and matched filter with prior windowing of the frequency-domain data with Hamming and Blackman windows. Target at a delay of 3 ns. ....	126
Figure 7.2.2.3: Comparison of Kalman filter response with matched filter and matched filter with prior windowing of the frequency-domain data with Hamming and Blackman windows. Target at a delay of 2.75 ns.....	128
Figure 7.3.1: Comparison between Kalman filter and matched-filter response for TM-46, an anti-tank mine from the field experiment.....	130
Figure 7.3.2: Comparison of sum and $m$ plots obtained from Kalman and matched-filter processing. The $m$ plot for the Kalman filter has low $m$ values, indicating that the target is symmetric. ....	131
Figure 7.3.3: Cascade plot of $m$ values for TM-46 with matched filter and Kalman filter. A deep null can be seen in the cascade plot using Kalman filter, indicating that the target is a mine. ....	132

## List of Tables

Table 3.2.1 Physical Properties of the Styrofoam Disc.....	27
Table 5.2.1.1 Physical Properties of the Styrofoam Disc.....	54
Table 5.2.2.1 Physical Properties for PMA-3. Reproduced from [8] .....	66
Table 6.4.1.1 Radar Parameters for Simulation .....	103
Table 6.5.1 Physical Properties of TM-46. Reproduced from [8].....	112

## **Abstract**

Landmines are *Hidden Killers* [1] that maim and kill civilians long after a war has ended. Detecting and neutralizing landmines buried all over the world remains a challenge. Landmine detectors that have been developed are based on exploiting some of the characteristic features of the mines like the metal content or chemical signatures of the explosives. In our research effort, a unique feature present in the landmines and absent in clutter targets has been used to develop a detection scheme.

In general, man-made objects exhibit the property of being symmetric across a plane, which is absent in clutter objects like rocks or bullet casings. Therefore, symmetry in landmines can be used to distinguish them from clutter objects buried beneath the ground. Our approach is to use a Ground Penetrating Radar (GPR) for detecting the presence of subsurface targets and also classifying them as landmines or clutter objects based on the level of symmetry. A GPR operating with a bandwidth of 4 GHz in the frequency range 2 GHz to 6 GHz has been used to extract the reflection symmetry inherently present in the landmines. This thesis investigates the possibility of deploying the detection scheme in the minefield. A sensor hand-held model with GPR to detect and classify the subsurface targets has been put forth in this thesis. The sensor hand-held model developed was validated and tested by performing various experiments in the laboratory and field. The results obtained from the experiments are presented and explained.

The conventional signal-processing algorithm used in the field of radar is the correlation or matched filter, which has the feature of maximizing the Signal-to-Noise

Ratio (SNR). Is a matched filter an optimum signal processor for subsurface target detection? Since the ground is a dominant scatterer and also clutter (in the application of landmine detection), maximizing the Signal-to-Interference Ratio (SIR) should be the criterion for the developing an optimum filter. This thesis aims at developing robust signal-processing algorithms based on the Minimum Mean-Squared Error (MMSE) criterion and principles of the Kalman filter to address the problems of clutter in landmine detection.

# Chapter 1

## Introduction and Motivation

Landmines maim and kill civilians long after a war has ceased. According to estimates from The United Nations, there are approximately 60 to 70 million landmines in at least 70 countries around the world. Some of the worst affected nations are Angola, Afghanistan and Cambodia [3]. These *Hidden Killers* maimed or killed approximately 26,000 civilians, the majority of whom are children [3]. Landmines can be easily manufactured, are very inexpensive and can be deployed with little effort. But the process of demining is slow, expensive and dangerous. Each buried landmine incurs a cost in the range of \$300 to \$1000 to be detected and neutralized [3]. The main problem in eliminating these hidden killers from the earth is the clearance rate, which is the rate at which the mines are cleared. At the present clearance rate it will take years to detect and neutralize the mines buried all over the world. The other requirements for an efficient landmine detection scheme are a low Probability of False Alarm ( $P_{FA}$ ) (i.e., the probability of detecting a mine when the subsurface target is clutter) and a high Probability of Detection ( $P_D$ ).

In the conventional method of clearing a mine field, a person enters the field with a long stick, at the end of which is a detector, and tries to find mines by moving the detector over the surface of the earth. This method of clearing the minefields is slow, inefficient and highly dangerous. The role of technology in solving the global crisis of landmines is to help develop efficient landmine detection tools, which will

not only speed up the demining process but also reduce the risk of loss of human life during the process of clearing a minefield. The science and engineering communities around the world have focused on the problem of landmine detection and have developed some detection schemes. A brief explanation of the research in the field of landmine detection is explained in the following section.

## **1.1 Research in Landmine Detection**

Research in the field of landmine detection aims at developing detection tools that locate the hidden killers based on their different characteristics like the size, shape, chemical signature of the explosives used or thermal radiation. The different detection schemes are explained briefly in this section with their advantages and disadvantages.

Initially, mines had a significant amount of metal content in them. Therefore, metal detectors based on the principle of Electro Magnetic Induction (EMI) were developed to detect the presence of metal in the mines. The advantage of using the metal detector is its compact hand-held structure and a relatively simple principle of operation. But the main problem with the metal detector is the high false-alarm rate because there are many other metallic objects, like bullet casings or shrapnel under the ground in the minefields that can also be detected as mines. Moreover, with mines now being manufactured with very little or no metal content in them, landmine detection using metal detectors will become even more difficult.

Landmines are of different shapes and sizes that cause them to have different thermal radiation patterns. Infrared detectors use this property of thermal radiation to differentiate between a mine and clutter [1]. If a certain level of thermal radiation of the soil without the presence of a target is obtained by measurements, then changes in thermal radiation measurement from that obtained from the soil indicate some subsurface target. But it has been proved that soil moisture can produce variations in thermal radiation, which means the difference in thermal radiation detected might not only be because of some subsurface targets [2]. This leads to a significant false-alarm rate. Moreover, the detection of mines is also dependent on the weather conditions, type of soil and the size and shape of the mine.

In many research efforts the possibility of detecting the landmines based on the chemical signature of the explosives used has been investigated. Landmines are filled with explosive chemicals that detonate on application of pressure. Detectors were developed that can detect the landmines based on the chemicals used in them [1].

- Dogs were used for landmine detection owing to their sensitive olfactory system. The dogs are trained to sniff for specific chemical signatures and taken to the minefield. The main disadvantage of using dogs is that they are not efficient, it takes a lot of time to train them and they wear out after some time, thereby slowing down the detection process.
- Nuclear detectors were developed that work on the principle of transmitting radio waves into the ground and where they react with the

chemical vapors emanating from the explosives used in the landmines.

The detection is performed based on the chemical reaction.

- Research has also been conducted on the possibility of using microorganisms for the purpose of landmine detection, using the chemical vapors emanating from the landmines. The microorganisms are sprayed on the ground where they react with the chemical vapors to produce a fluorescent effect, which can be later detected using a photo detector [2].

The main problem associated with employing the chemical signature of explosives used in the mines to detect the hidden killers is the significant false-alarm rate (i.e., the probability is high that the landmine detection scheme detects a clutter target as a mine). This is because the atmosphere in the minefields is filled with chemical vapors from recent explosions, which can lead the chemical sensors astray.

All the aforementioned methods of detecting landmines have the common problem of significant false-alarm rates. Also they are not able to distinguish clearly between the mines and clutter objects buried beneath the ground (as in the case of metal detectors). The use of Ground Penetrating Radar (GPR) for developing efficient landmine detection schemes is being investigated in many research efforts. Can GPR provide a potential solution for the problem of landmine detection?

## 1.2 GPR in Landmine Detection

A potential solution for the problem of landmine detection has been investigated using the Ground Penetrating Radar (GPR). How can GPR be used to detect landmines, or for that matter, any subsurface target?

A subsurface target has a relative dielectric constant, which will be different from that of the ground, and this dielectric discontinuity can be detected by using GPR. As two targets with different relative dielectric constants will differ in their scattering characteristics, they can be differentiated based on the received scattering by using a GPR. But there might be many subsurface targets that will have a relative dielectric constant different from that of the soil and hence will be detected by the radar. Therefore, by using only the ground penetrating radar, a target beneath the ground can be detected but this subsurface target cannot be classified as a mine or clutter [1, 2].

Landmine detection schemes have been developed in which the electromagnetic signature of the subsurface target is matched with a bank of electromagnetic scattering obtained from different mines buried across the world. But the problem with this method is that there are different types of mines buried all over the world. This will lead to an exhaustive search to match the scattering characteristics of the subsurface target to that of the mine. Moreover, the soil type in which the mine is buried also affects the scattering characteristics. There is a high probability of missed detection if the subsurface scattering is attenuated or distorted significantly due to soil characteristics.

Landmine detectors have also been developed using GPR along with improved and advanced metal detection, which will help in detecting and differentiating between the mines and clutter. Since the detection of anti-personnel or anti-tank mines still depends on a metal detector and thermal radiations (in the case of infrared sensors), false alarm is still a problem. What is the solution for reducing the false-alarm rate? Is there a unique property in landmines that is absent in clutter and can be used to develop an efficient landmine detection scheme?

### 1.2.1 Our Approach

Based on the different relative dielectric constants of the soil and the subsurface targets the GPR can detect, this dielectric discontinuity shows the presence of a subsurface target. To identify a unique property present in the landmines that is absent in the clutter objects buried beneath the ground, consider the picture of an anti-personnel mine and a natural clutter, rock, shown in Figure 1.2.1.1.



**Figure 1.2.1.1: Pictures of anti-personnel landmine and a natural clutter target, rock.**

Looking at the mine and the rock in the Figure 1.2.1.1, it can be inferred that the mine is symmetric across a particular plane whereas the rock is asymmetric.

Therefore, the property of symmetry in landmines is unique and can be used to differentiate between mines and other subsurface objects like rocks, bullet casings, or shrapnel. Moreover, the property of symmetry in landmines is independent of the type of chemicals used as explosives, the shape and size of the mine, the casing of the mine, the depth at which it is buried, and soil moisture. Therefore, if a method of extracting the symmetry information in the subsurface targets is developed, then the probability of false alarm in detecting landmines can be significantly reduced. The question remains as to how the level of symmetry in subsurface targets can be established?

Our approach concentrated on the possibility of using ground penetrating radar to not only detect the presence of a subsurface target but also extract the symmetry information in the subsurface targets. How can GPR be used to extract the level of symmetry in the subsurface targets?

In Chapter 2, *Development of Detection Scheme*, a method is detailed in which a GPR can be used to extract the symmetry information in the subsurface target apart from just detecting it. This chapter will introduce various concepts involved in describing symmetry in objects. A symmetry measure will be defined in which the subsurface target can be classified as symmetric or asymmetric (hence the targets can be classified as mines or clutter objects). The main problem with landmine detection is that the targets are buried at very shallow depths beneath the ground. The radar developed should be able to resolve and separate the two targets (i.e., the ground and the landmine), which are few centimeters apart.

Chapter 3, *System Specifications and Initial Experiments*, details the radar system parameters such as the bandwidth of operation and the number of frequency points. Some initial experiments with a Styrofoam disc (used to simulate a landmine) were conducted in the laboratory, and results are explained. The possibility of developing a compact landmine detector that implements the detection scheme developed in Chapter 2 has been investigated. Hand-Held detectors are compact and the most widely used landmine detectors.

Chapter 4, *Simulating a Hand-Held Detector*, discusses the basic GPR sensor hand-held model and the limitations of such a model with regard to the confidence level in deciding whether the subsurface target is a mine or clutter object. A data collection system with precise positioners was developed to simulate the hand-held detector. A simple and efficient data collection scheme to simulate the hand-held sensor has been explained. An outline of the steps for analyzing the data collected to decide whether the target is symmetric or asymmetric is also dealt with in this chapter.

Chapter 5, *Experiments and Results*, explains the sequence of data-processing steps before the final result is obtained from the raw frequency-domain data. Different experiments were conducted to test the concept of using GPR and simulating a hand-held detector to extract the level of symmetry from subsurface targets. The results of these experiments are presented and discussed. The results obtained for the data collected during the field experiments are also been discussed.

Chapter 6, *Minimum Mean-Squared Error GPR Processor*, details the need for robust signal-processing algorithms for detecting subsurface targets buried at shallow depths. The scattering from the ground is considered clutter for the application of landmine detection. The response from the ground is large when compared to the response from the subsurface target. The processing algorithm used should ideally maximize the signal-to-interference ratio and not just the signal-to-noise ratio (as in the case of a matched filter). An algorithm based on the Minimum Mean-Squared Error (MMSE) criterion is proposed to maximize the signal-to-interference ratio. Simulations were performed to test and validate the MMSE algorithm, and the tested algorithm was used to process the measured data. The results are explained and the performance of the MMSE GPR processor is analyzed. But using the MMSE GPR processor was time consuming and an iterative algorithm to implement the same method was developed based on the principles of the Kalman filter.

Chapter 7, *Kalman Filter Implementation*, explains the Kalman filter algorithm as an iterative implementation of the MMSE processor. Simulations performed are explained and the results are discussed and compared with those obtained from the matched filter and the MMSE GPR processor.

Chapter 8, *Conclusions and Future Work*, summarizes the concepts developed and tested for this thesis, highlights possible future work, and offers conclusions from this research effort.

## Chapter 2

### Development of Detection Scheme

Landmine detectors exploit the properties of the landmines for the purpose of detection. Different methods, as described in Chapter 1, use metal detection, thermal radiation or sensing the chemical signature of the explosives for detecting and differentiating subsurface targets as landmines or natural clutter. Low false-alarm rate is an important criterion when developing a landmine detection scheme. A common problem with all the landmine detection methods mentioned in Chapter 1 is that they have significant probability of false alarm, and the detection performance is dependent on many conditions.

Our research is based on the principle that

*Landmines have a certain level of symmetry across a plane,  
which is absent in other objects such as rocks, shrapnel,  
bullet casings or in general subsurface clutter targets.*

Thus, if we can establish the level of symmetry in the subsurface targets, that information can be used to develop an efficient landmine detection scheme. The use of Ground Penetrating Radar (GPR) to detect the presence of the subsurface target and also classify it as a mine or clutter object based on the concept of symmetry has been investigated; this chapter provides a basic understanding of the landmine detection scheme.

The GPR can be used to detect the presence of the subsurface targets by analyzing the scattering as a function of time. The subsurface target will have different scattering characteristics than that of the ground, owing to its different relative dielectric constant when compared to that of the soil. Therefore, the subsurface target manifests itself as electromagnetic scattering at a delay, which is greater than the delay that corresponds to the ground response.

For the application of landmine detection, the GPR used should not only be in a position to detect the presence of subsurface targets but also classify them as mines or clutter targets. It has been already stated that landmines exhibit a certain level of symmetry, which is absent in clutter objects. But how can GPR be used to differentiate between landmines and natural clutter? The detection scheme described in this chapter will explain the method of extracting the symmetry information in the subsurface targets using radar measurements.

On what basis can an object be declared as symmetric? What are different types of symmetry present in the objects and how can they be used to solve the problem at hand? The answer to the above two questions is detailed in the next section.

## **2.1 Concept of Symmetry**

An object is said to be symmetric with respect to a plane when specific operations performed on the object about that plane result in the same object. The

type of symmetry exhibited by the object is dependent upon the type of operation that when performed with respect to a plane, essentially gives the same object.

Consider the objects shown in the Figure 2.1.1. When a reflection operation is performed on the object in 2.1.1(a) with respect to the plane  $XY$ , the resulting

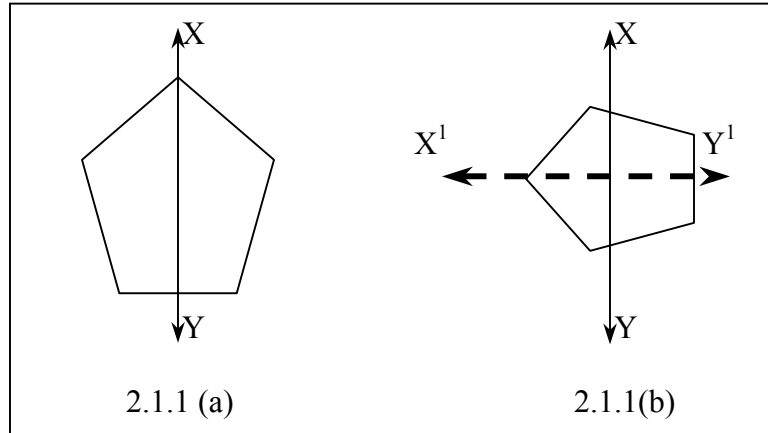


**Figure 2.1.1: Examples to illustrate reflection symmetry: (a) shows an object that exhibits reflection symmetry about the plane  $XY$ ; (b) illustrates an object that exhibits reflection symmetry about the plane  $X^1Y^1$ .**

object is also the same, which means that the object exhibits reflection symmetry with the plane of reflection symmetry being  $XY$ . However the object in Figure 2.1.1(b) will not result in the same object on reflection across the plane  $XY$  and hence does not possess reflection symmetry across the plane  $XY$ . Note that the object in Figure 2.1.1 (b), however, does exhibit reflection symmetry with respect to the plane  $X^1Y^1$  [4].

Consider the cases shown in Figure 2.1.2(a) and (b). The circular object is symmetric when rotated about any of the planes. It also possesses reflection

symmetry about the planes shown in Figure 2.1.2 (a). For the square in Figure 2.1.2 (b), the two planes shown are planes of reflection symmetry. But if the square is

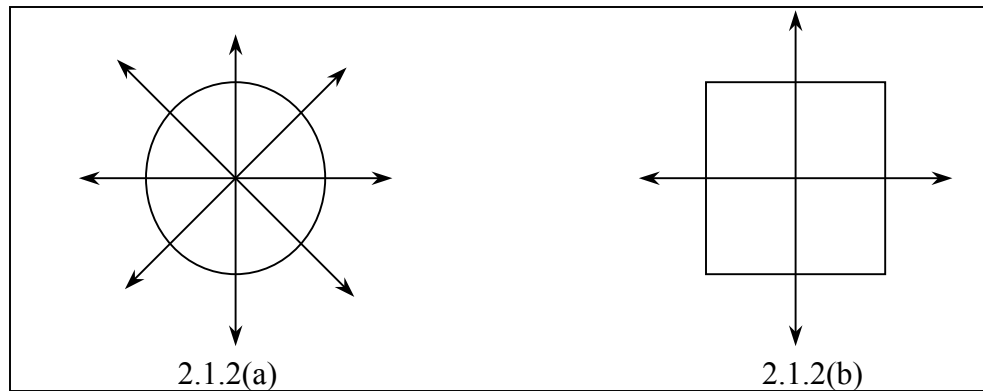


**Figure 2.1.2: Examples of objects exhibiting rotational symmetry, (a), and a combination of rotational and reflection symmetry, (b).**

rotated  $90^\circ$  and then reflected, the resulting object is again the same. This means that the square also possesses a combination of reflection and  $90^\circ$  rotational symmetry.

How can different types of symmetry be used to classify mines? Landmines, like many man-made objects, exhibit reflection symmetry, and they are buried in such a manner that this symmetry is not destroyed [4]. This property of reflection symmetry in landmines can be used to distinguish them from clutter targets such as rocks, which do not possess reflection symmetry.

The question still remains as to how GPR can be used for extracting symmetry information in the subsurface targets and hence classify them as landmines (symmetric) or clutter (asymmetric). The most important question that needs to be answered is: How does the symmetry in subsurface targets manifest itself in the electromagnetic scattering?

## 2.2 GPR and Symmetry for Landmine Detection

Landmines buried all over the world exhibit reflection symmetry across some plane. Our research investigated the possibility of using GPR for extracting the level of reflection symmetry in the subsurface targets to develop an efficient landmine detection scheme.

The plane across which the landmines exhibit reflection symmetry will generally be perpendicular to the plane of the ground (and the mine itself will be buried parallel to the ground). Consider the configuration of sensors shown in Figure 2.2.1. This figure shows a top view with the surface of the ground parallel to this page, the target is buried beneath the ground, and the sensors are positioned on a plane above and parallel to the ground.  $T_X$  is the transmit antenna and  $R_X$  is the receive antenna. The dimension of the rectangular box (used to denote the transmit and receive antennas in the figure) indicates the effective aperture of the antennas

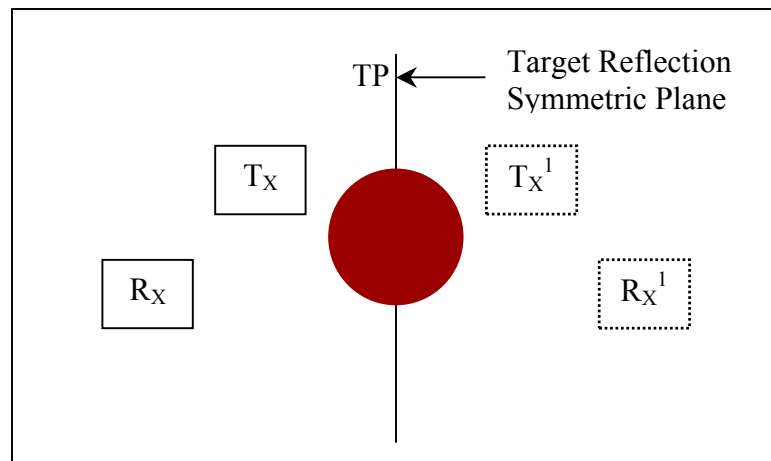


**Figure 2.2.1: Diagram explaining the concept of mirrored bistatic observation pairs. The figure also indicates the target reflection symmetric plane.**

used. The transmit antenna ( $T_X$ ) and the receive antenna ( $R_X$ ) constitute a bistatic sensor measurement. The target buried below the surface of the ground exhibits reflection symmetry with respect to the plane TP. The plane TP is called the *Target Reflection Symmetric Plane* (a plane that is perpendicular to the ground). The bistatic measurements ( $T_X$ - $R_X$ ) before and after the reflection of the target are identical since the object exhibits reflection symmetry [4, 5]. For the application to landmine detection, reflecting the object (i.e., the landmine) about its plane of reflection symmetry is not practical. However, instead of reflecting the object and collecting the measurements, the bistatic configuration  $T_X$ - $R_X$  can be reflected about the plane TP and the bistatic measurement ( $T_X^1$ - $R_X^1$ ) can be recorded. The measurements from both the bistatic sensor configurations will be identical since the object is symmetric [4]. The bistatic measurements  $T_X$ - $R_X$  and  $T_X^1$ - $R_X^1$  form a mirrored bistatic observation pair across the plane TP.

The plane about which the bistatic pair forms a mirror image is called the *Measurement Reflection Symmetric Plane*. The bistatic observation pair shown in Figure 2.2.1 is one of the many possible observation pairs that can be formed with the measurement reflection symmetric plane being TP. Also, if the bistatic sensor measurement  $T_X$ - $R_X$  is reflected about a plane that is different than the target reflection symmetric plane, the responses from the bistatic measurements will not be identical. Thus, symmetry in the subsurface target manifests itself as identical electromagnetic scattering when the measurement reflection symmetric plane aligns with the target reflection symmetric plane.

Clutter objects do not possess reflection symmetry, which leads to an inference that the mirrored bistatic observation pair will not produce identical measurements. Therefore ground penetrating radar can detect the presence of the subsurface targets and more importantly subsurface targets can be classified as landmines (symmetric targets) or clutter objects (asymmetric targets) based on the concept of symmetry.

A mathematical representation of the radar measurements is essential for further analysis.

### **2.3 Mathematical Representation of Measurements**

Let  $x_1(t)$  and  $x_2(t)$  represent the complex scattering as a function of time obtained from the bistatic sensor measurements  $T_X-R_X$  and  $T_X^1-R_X^1$  constituting a mirrored bistatic observation pair (one such observation is shown in Figure 2.2.1). The scattering obtained as a function of time consists of the antenna coupling, ground response, the response from the subsurface target (if any) and noise. But the important scattering is that from the subsurface target only. The response from other components constitutes interference for the application of landmine detection. Therefore, the response obtained from the sensor measurements are gated using a window function,  $w(t)$ . The function  $w(t)$  is non zero only from time  $t_1$  to  $t_2$ , where time  $t_1$  and  $t_2$  are chosen such that the response  $f(t)$  after time gating has only the subsurface scattering. The time-gated radar responses as a function of time are given

in (2.3.1)

$$\begin{aligned} f_1(t) &= x_1(t)w(t) \\ f_2(t) &= x_2(t)w(t) \end{aligned} \quad (2.3.1)$$

where

$$\begin{aligned} w(t) &= 1 \quad t_1 \leq t \leq t_2 \\ &= 0 \quad \text{elsewhere} \end{aligned}$$

Having put forth a mathematical representation of the radar measurements and subsurface scattering, we need to see how the measurements  $f_1(t)$  and  $f_2(t)$  can be used to detect the presence of a subsurface target and more importantly classify it as landmine or clutter object. How can the presence of a subsurface target be established using the subsurface scattering  $f_1(t)$  and  $f_2(t)$ ?

The presence of the subsurface target can be established if the complex response  $f_1(t)$  or  $f_2(t)$  is non zero and significantly greater than noise. A measure of how much energy is scattered by the subsurface target is given by the expression in (2.3.2)

$$\Sigma = \int |f_1(t) + f_2(t)|^2 dt \quad (2.3.2)$$

The value  $\Sigma$  obtained after evaluating the expression in (2.3.2) is termed as **sum** value. The sum value will be a non zero and of significantly high value if the subsurface target is present, irrespective of whether the subsurface target is either symmetric or asymmetric. The sum value will be used in this thesis to detect the presence of a subsurface target. Detecting the presence of a subsurface object is one of the requirements for developing a landmine detection scheme. The other requirement is to classify the subsurface targets as mines or clutter.

The possibility of using the inherent reflection symmetry of landmines for differentiating them from clutter targets has been investigated in our research effort. There is need for a mathematical representation to quantify the level of symmetry in subsurface targets.

## 2.4 Symmetry Measure

A mathematical representation of the level of symmetry in the subsurface targets is obtained by defining a dimensionless value called the  $m$  coefficient [5]. The  $m$  coefficient is mathematically defined as in (2.4.1)[5]

$$m = \frac{\int |f_1(t) - f_2(t)|^2 dt}{\int |f_1(t) + f_2(t)|^2 dt} \quad (2.4.1)$$

$$= \frac{\int |f_1(t) - f_2(t)|^2 dt}{\Sigma}$$

Note that the time-gated radar responses have been used for the calculation of the symmetry measure. This is done to avoid inducing a bias in the  $m$  coefficients due to the interference. A bias in the calculation of the symmetry measure can lead to a false alarm or missed detection. What are the typical values for the  $m$  coefficients for symmetric and asymmetric targets?

If the subsurface target is symmetric, the bistatic measurements will be identical provided they form a mirrored observation pair such that the measurement reflection symmetric plane aligns with the plane of target symmetry. When the complex bistatic measurements are identical, then the numerator in (2.4.1) will ideally

be zero, the denominator will be non zero (indicating the presence of the subsurface target), and the magnitude of the  $m$  coefficient will also be equal to zero. But the radar measurements will not be exactly identical owing to measurement error and noise. Therefore, the typical value for the  $m$  coefficient for a symmetric target is very small (provided the measurement reflection symmetric plane is aligned with the target reflection symmetric plane).

For an asymmetric target, the denominator of (2.4.1) (i.e., the sum value,  $\Sigma$ ), should be non zero and high, indicating the presence of a subsurface target. The mirrored bistatic radar measurements for an asymmetric target should be ideally dissimilar and thereby yielding a high value for numerator in (2.4.1). But this is not always true as the responses  $f_1(t)$  and  $f_2(t)$  depend on how asymmetric the target is with respect to the measurement reflection symmetric plane. Moreover, for mirrored bistatic observation pairs in which the sensor elements are right above the target (as shown in Figure 2.2.1), the sum values will be higher when compared to other locations of the mirrored observation pairs. This high sum value can reduce the magnitude of  $m$  coefficient even if the subsurface target is asymmetric. Therefore, the typical  $m$  values for an asymmetric target can range from a low value to a high value. The term  $m$  value and  $m$  coefficient are one and the same and indicate the symmetry measure defined in (2.4.1); they will be used interchangeably in the rest of the thesis.

But is a single  $m$  value sufficient to decide whether the subsurface target is symmetric (mine) or asymmetric (clutter) with a high level of confidence?

### 2.4.1 Confidence Level in Target Classification

If the target is symmetric and radar measurements are collected such that a mirrored bistatic observation pair is formed so that the measurement reflection symmetric plane is aligned with the target reflection symmetric plane, then the radar responses will yield a low  $m$  value. Even if the target is asymmetric, there is a possibility of the  $m$  value having a low magnitude (see explanation in Section 2.4.). Therefore, based on one measurement and a single  $m$  coefficient, the confidence level with which the subsurface target can be classified as a mine or natural clutter is low and can lead to a high Probability of False Alarm ( $P_{FA}$ ).

The solution for this uncertainty is to collect many mirrored bistatic observation pairs where the measurement reflection symmetric plane aligns with the plane of target symmetry. The configuration shown in Figure 2.2.1 is one of the many possible mirrored bistatic observation pairs. All the observation pairs mirrored across the target reflection symmetric plane can be used to generate a set of  $m$  values. Ideally, for a symmetric target, all the  $m$  values should have a low magnitude, whereas for an asymmetric target, the  $m$  values will range from low to high (without any specific pattern). The larger the number of  $m$  values acquired to decide on symmetry in the subsurface target, the higher the confidence level in target classification.

Is there any decision threshold for target classification? What should be an appropriate threshold based on which the subsurface targets can be classified as mines or clutter?

## 2.4.2 Decision Threshold

Based on the  $m$  coefficients, a decision threshold can be set for deciding whether the subsurface target is a mine or clutter. If the majority of  $m$  values are less than the threshold, then the subsurface target can be classified as symmetric. Ideally, this threshold should be a small value to minimize  $P_{FA}$ . But the threshold should not be exceptionally small because it will lead to higher Probability of Missed Detection ( $P_M$ ). On the other hand, if the decision threshold is set high to reduce  $P_M$ , the  $P_{FA}$  increases. Therefore, setting the decision threshold is a trade-off and depends on the acceptable values of  $P_{FA}$  and  $P_M$ .

Consider an example where the  $m$  coefficient of 0.2 is obtained from the math in (2.4.1) for a symmetric target. If the decision threshold is set at 0.1 to reduce the  $P_{FA}$ , then, based on the  $m$  value obtained, the target is declared to be a clutter object. This is a missed detection. To avoid this problem, the decision threshold should be increased. By increasing the decision threshold, the  $P_{FA}$  increases because there is a possibility that the  $m$  value for the asymmetric target (clutter) can be low and hence it will also be classified as a symmetric target (landmine). Therefore the optimum value of the decision threshold depends on the requirements of  $P_M$  and  $P_{FA}$ .

A theoretical concept has been put forth for landmine detection using the concept of symmetry and GPR. A mathematical representation for the subsurface scattering has been given. The sum value ( $\Sigma$ ) and  $m$  value have been introduced and will be used in the thesis for detecting the presence of a subsurface target (sum value) and classifying it as a mine or clutter based on the concept of symmetry ( $m$  value).

The concept has to be tested in the laboratory using different bistatic radar measurements. To test the concept, a radar system first has to be developed with the required specifications suitable for the application of detecting subsurface targets.

What are the different parameters that have to be taken into consideration for developing a GPR for landmine detection? Using the developed system, it remains to be seen whether the theoretical concept of symmetry will be an efficient landmine detection scheme.

## **Chapter 3**

### **System Specifications and Initial Experiments**

A theoretical concept for developing an efficient landmine detection scheme based on the concept of symmetry has been put forth in Chapter 2. It has been stated that the mirrored bistatic observations using ground penetrating radar can be used to extract symmetry information in the subsurface target, and therefore the subsurface target can be classified as a landmine or clutter. One of the main challenges in landmine detection is that the mines are buried at shallow depths. This poses a problem since the radar has to be designed so that it can resolve the two targets, the ground and the subsurface target, which are close together.

The motive of this chapter is to explain the radar parameters used and give reasons why the parameters chosen are optimum. Initial experiments were conducted in the laboratory to prove that our GPR is able to detect the objects buried beneath the ground and also extract the level of symmetry in the subsurface target.

#### **3.1 System Specifications**

The system used for data collection is a network-analyzer based step-frequency radar. The radar parameters such as bandwidth and number of frequency points in the frequency of operation were set in the network analyzer.

For the problem of landmine detection, this GPR must be in a position to resolve closely spaced targets, the ground and the landmine. In many cases the

landmines are buried a few centimeters beneath the surface of the ground. The parameter of the GPR, which controls its capability to resolve closely spaced targets, is the radar bandwidth. The range resolution of the radar is the minimum distance between two targets that can be resolved without ambiguity. The radar range resolution is inversely proportional to the bandwidth and is mathematically expressed in (3.1.1) [6, 7].

$$\Delta r = \frac{v}{2B} \quad (3.1.1)$$

where  $v$  is the velocity of propagating electromagnetic wave and is given by  $\frac{c}{\sqrt{\epsilon_R}}$  (where  $c$  is the velocity of light and  $\epsilon_R$  is the relative dielectric constant of the medium in which the electromagnetic wave propagates). For landmine detection the value of  $\epsilon_R$  is assumed to be equal to four, which is approximately the dielectric constant of sand. In (3.1.1)  $\Delta r$  is the radar range resolution and  $B$  is the bandwidth of operation of the radar.

For most landmine detection experiments, the subsurface target is buried a few centimeters (6 cm to 7 cm) below the surface of the ground. Therefore the bandwidth has to be huge so the radar has good range resolution. The bandwidth of the radar was selected so the range resolution is close to 2 cm. This means that the radar can resolve two targets separated by a distance of 2 cm without any ambiguity. Using the velocity of light in free space for  $c$  ( $3 \times 10^8$  m/s) and  $\Delta r \approx 2$  cm, the bandwidth of the radar was set equal to 4 GHz spanning from 2 GHz to 6 GHz [5]. The reason why the bandwidth of operation ranged from 2 GHz-6 GHz is because

high frequencies tend to extract symmetry information in the subsurface targets better than low frequencies [5].

Having set the radar bandwidth, the number of frequency points to be collected in the bandwidth of operation needs to be defined. The number of frequency points defines the frequency increment and therefore sets the unambiguous range of the radar. If  $N$  is the total number of frequency steps, then the unambiguous range  $R$  is defined as in (3.1.2) [7]

$$R = \frac{(N-1)v}{2B} \quad (3.1.2)$$

The unambiguous range  $R$  (as defined in (3.1.2)) corresponds to a one-way propagation distance in meters. To calculate the number of frequency points in the bandwidth of operation, the unambiguous range  $R$  is chosen as 3.5 m. Why 3.5 m? This is because there is no significant scattering from a depth greater than 3.5 m owing to the attenuation of the propagating electromagnetic wave through the soil. Using the value of  $R = 3.5\text{m}$ , the velocity of propagation  $v$ , and the radar bandwidth  $B$ , the number of frequency points  $N$  was calculated to be equal to 175. Since the network analyzer allows an option of only specific settings for the number of frequency points, it was set equal to 201.

A network analyzer is used to generate a transmit signal and also collect the data (the  $S_{21}$  parameter), which is stored in a desktop. A General Purpose Interface Bus (GPIB) is used to interface the network analyzer and the computer. The network analyzer is calibrated before it is used to collect data. The calibration procedure

includes the microwave cables and the amplifier on the transmit side, but does not include the transmit and receive antennas.

Thus the important parameters of the radar system have been explained with reasons as to why the selected parameters are optimum. Some initial experiments were conducted with the motive of whether symmetric targets could be detected and, more important, classified as symmetric based on radar measurements.

### **3.2 Initial Experiments in Sandpit**

Initial experiments to test the concept were performed in the *Sandpit* in Radar Systems and Remote Sensing Laboratory. The sandpit is a huge concrete hollow structure filled with sand where different targets can be buried and ground penetrating radars can be tested. The experimental setup in the laboratory constitutes a computer, antenna positioner, antennas and a network analyzer. A computer program controls the antenna positioner so that the antennas can be moved and data can be collected at different points. The antenna positioner consists of motors, which move the antennas to different points, and an optical encoder is used to help the motors accurately position the antennas [5]. The computer establishes a connection with the network analyzer and the data collected by the network analyzer are transferred into the computer. The experiments conducted in the sandpit were on a symmetric target.



**Figure 3.2.1: Picture of the Styrofoam disc used to simulate a mine in the sandpit experiments.**

A Styrofoam disc was chosen as a target for the initial experiments in the sandpit. The picture of the Styrofoam disc is shown in Figure 3.2.1 and its physical properties are tabulated in Table 3.2.1.

**Table 3.2.1 Physical Properties of the Styrofoam Disc**

Physical Property	Value for the Styrofoam Disc
Diameter	14.73 cm
Height	3.17 cm
Weight	50grams
Dielectric Constant	$\approx 1.02^*$

\*Source for the value: <http://www.csgnetwork.com/dieconstantstable.html>

The Styrofoam disc was buried approximately 10 cm below the ground and bistatic radar measurements were collected so that mirrored observation pairs across the target reflection symmetric plane could be formed. To ascertain that the target was detected, the ground data (without the target buried) and the ground plus target data were collected and the respective measurements of scattering as a function of time

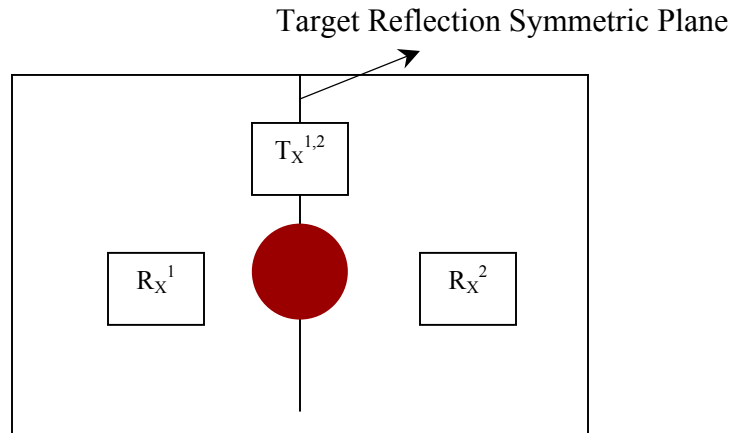


**Figure 3.2.2: Mirrored bistatic observation pair used to collect measurements in the sandpit on the Styrofoam disc.**

were compared. The data collected were in the frequency-domain and matched-filter processing (with a frequency domain Hamming window) was performed to obtain the scattering as a function of time. The mirrored bistatic observation pair for which the data were processed is shown in Figure 3.2.2, which is a top view with the plane of ground parallel to the surface of the page.

The real part of the complex radar response as a function of time for the ground and ground plus target is shown in Figure 3.2.3. The real part of the complex scattering for the ground measurement shows energy at 1.2 ns, which is the direct coupling between the transmit and receive antennas, whereas the ground response, which is the dominant scatterer, can be seen at a delay around 2 ns. The radar response as a function of time for the data recorded for ground plus target indicates energy at a delay around 3 ns, which is absent in the ground measurement. This is the

Styrofoam disc, which was buried under the ground! Therefore, the presence of a subsurface target is reflected as electromagnetic scattering at a delay that is greater

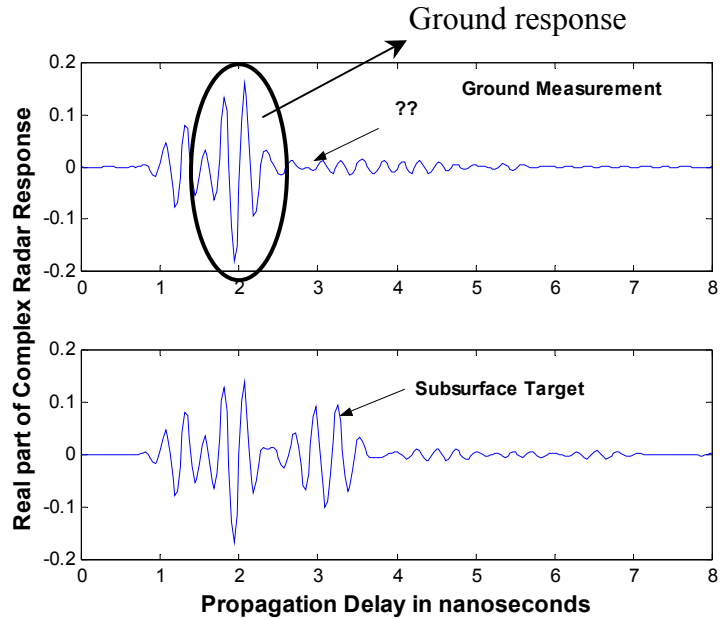


**Figure 3.2.3: Real part of scattering profile for ground and ground + target (the target being the symmetric Styrofoam disc).**

than that which corresponds to the ground response.

The presence of the subsurface target has been detected using radar measurements and now must be classified as symmetric or asymmetric. The bistatic measurements, which form the mirrored bistatic observation pair as shown in Figure 3.2.2, were processed and the real and imaginary parts of the complex scattering obtained for both the bistatic measurements are shown in Figure 3.2.4 in different colors ( $T_X^1-R_X^1$  in red and  $T_X^2-R_X^2$  in blue).

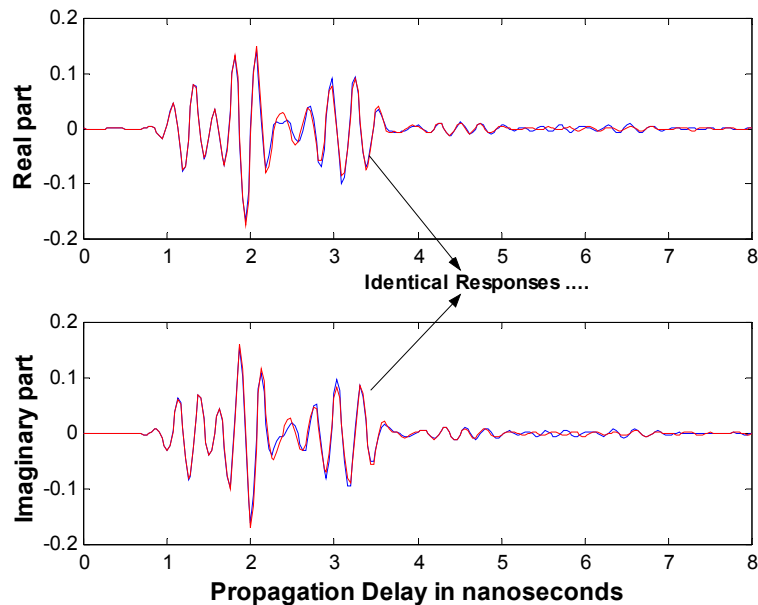


**Figure 3.2.4: Real and imaginary parts of the complex scattering for the mirrored bistatic observation shown in Figure 3.2.2. The scattering for bistatic measurement  $T_X^1-R_X^1$  is shown in red and the one for  $T_X^2-R_X^2$  is shown in blue.**

It can be seen from Figure 3.2.4 that the complex subsurface scattering at around 3 ns for both bistatic measurements is identical (to within measurement error and noise). A time gate can be applied, which is non zero in the region  $t_1 = 2.5$  ns to  $t_2 = 4.5$  ns, and then the gated radar responses can be used to compute the sum and the  $m$  value. The sum value will be high, as the gated responses are non zero and significantly higher than noise, and the  $m$  value will be very low, as the gated responses from both the bistatic measurements are almost identical. This indicates that the subsurface target has been detected and, more important, classified as a symmetric target.

Thus, using the ground penetrating radar, the presence of the subsurface target was detected and mirrored bistatic radar measurements were identical (to within measurement error and noise) when the subsurface target has reflection symmetry across the measurement reflection symmetric plane. But from a practical implementation standpoint, a compact landmine detector needs to be developed so that the detection scheme can be deployed in the minefield. The most widely used landmine detectors are hand-held detectors. Can GPR be used to develop a hand-held detector that can classify subsurface targets as mines or clutter based on the level of symmetry in subsurface targets?

## Chapter 4

### Simulating a Hand-Held Detector

The most popular and widely used commercial landmine detectors are hand-held detectors. A hand-held detector is used to scan from one end to the other over a piece of land where a mine might be present. Hand-Held detectors use one of many methods (e.g., detecting the presence of metal content in the subsurface target) for detecting and differentiating landmines and clutter. This type of hand-held detectors can lead to a significant false-alarm rate. The concept of extracting symmetry information in the buried subsurface targets using bistatic radar measurements has been put forth as an efficient landmine detection scheme in Chapter 2. Can this method of differentiating subsurface objects as landmines or natural clutter based on symmetry be used in hand-held detectors?

#### 4.1 Sensor Hand-Held Model

To use ground penetrating radar in the hand-held detectors to detect and classify subsurface targets as symmetric or asymmetric, the formation of mirrored bistatic observation pairs is required. A potential model of a hand-held detector that uses GPR to extract symmetry information in subsurface targets is shown in Figure 4.1.1. Figure 4.1.1 is a top view of the sensor hand-held model, with the surface of the ground being parallel to the plane of this page. All the figures in this chapter, which includes sensors, are drawn as a top view. Four sensors can be used to form a mirrored bistatic observation pair with “MP” as the measurement reflection

symmetric plane. Two mirrored bistatic observation pairs, in which the spacing between the bistatic measurements (which constitute the mirrored observation pair) is constant, is said to have the same *Sensor Geometry*. One such sensor geometry is shown in Figure 4.1.1. The hand-held detector, which is formed using the four sensors, will scan across with the sensor geometry depicted in Figure 4.1.1 in increments of  $\Delta x$  cm. It stops after every  $\Delta x$  cm and collects data that will be processed later for extracting the level of symmetry in the subsurface target.

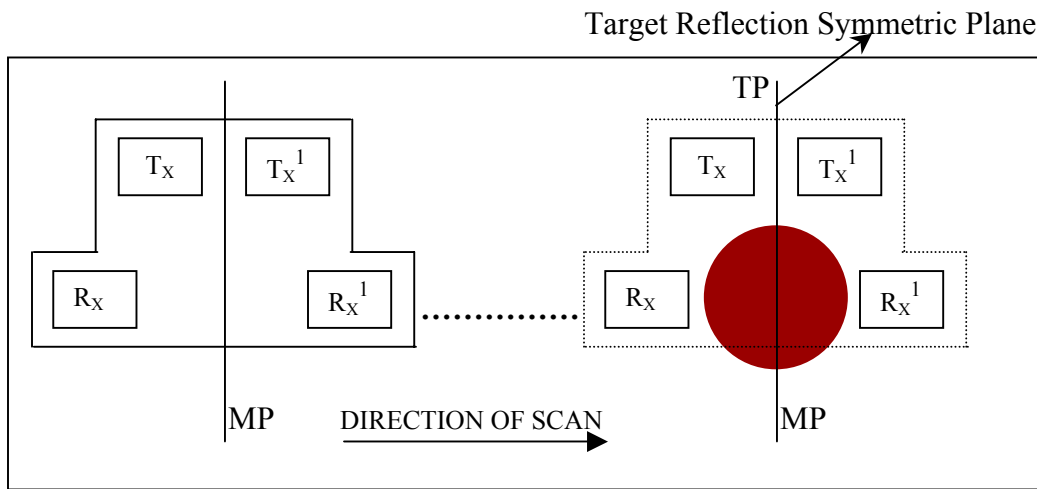


**Figure 4.1.1: A model for a single sensor geometry hand-held landmine detector that collects data by performing a single scan.**

As the hand-held detector moves and collects data, the plane about which the four sensors form a mirrored bistatic observation pair also changes. This measurement reflection symmetric plane for every data point actually corresponds to a physical plane perpendicular to the ground and is termed as *Measurement Plane* (MP). Through out the scan the sensor geometry remains the same (because the

spacing between the bistatic sensor measurements remains constant), but the measurement plane changes with every step.

The data collected from the fixed sensor geometry scan (Figure 4.1.1) have to be processed for detecting the presence of a subsurface target and also for classifying the subsurface target as a mine or a clutter object based on the concept of symmetry.

For detecting the presence of a subsurface target, the sum value ( $\Sigma$ ) defined in Section 2.3 will be used. The sum values are calculated as a function of the measurement plane for the scan performed with the sensor geometry shown in Figure 4.1.1. The presence of a subsurface target is shown as a high sum value for some measurement planes that correspond to the radar measurements for which the sensor geometries are in close proximity of the target (as shown in Figure 4.1.1). Therefore it can be concluded that:

***The measurement plane that corresponds to high sum values indicates the approximate location of the target.***

For target classification,  $m$  values using the math defined in (2.4.1), need to be computed as a function of the measurement plane. If the subsurface target is symmetric, then the calculated  $m$  coefficients will be low when the measurement plane aligns with the target reflection symmetric plane (TP). Therefore, for a specific sensor geometry,  $m$  coefficients are obtained as a function of the measurement plane. For a symmetric target the  $m$  value is very small only for a single measurement plane (when the measurement plane aligns with the plane of target symmetry). But is one

scan with a specific sensor geometry sufficient to decide whether the subsurface target is a mine or clutter?

Scanning with only one sensor geometry will lead to one data point for which the measurement plane aligns with TP and, hence, only one  $m$  value for target classification. If the  $m$  value for that specific data point is low, then the subsurface target can be classified as a mine. But the possibility of the target being natural clutter is also high. This is because the  $m$  coefficient for a clutter object need not always be a high value. Therefore target classification based on a scan with a single sensor geometry (this results in a single  $m$  value for target classification) is prone to a high probability of false alarm. The solution for this uncertainty is to perform the experiment of scanning with different sensor geometries and calculating the symmetry measures as a function of measurement plane. If the target is symmetric, the  $m$  coefficient for the data point for which the measurement plane aligns with the plane TP will have a low  $m$  value for all the sensor geometries. But for a clutter target, the symmetry measures will vary between low and high values with no specific pattern.

Scanning the hand-held detector can be performed repeatedly with different sensor geometries. However, instead of changing the sensor geometry and scanning several times, a hand-held detector with multiple sensor geometries can be developed as shown in Figure 4.1.2. Figure 4.1.2 shows a four-sensor geometry (each sensor geometry has been indicated in a different color) hand-held model in which each sensor geometry forms a mirrored bistatic observation pair across the measurement

plane indicated in Figure 4.1.2. The multiple sensor geometry hand-held detector is scanned from one end to the other of the experimental setup. With four sensor geometries, each measurement plane (which is separated by  $\Delta x$  cm, a user-defined value) will result in four  $m$  values, one from each of the sensor geometries.

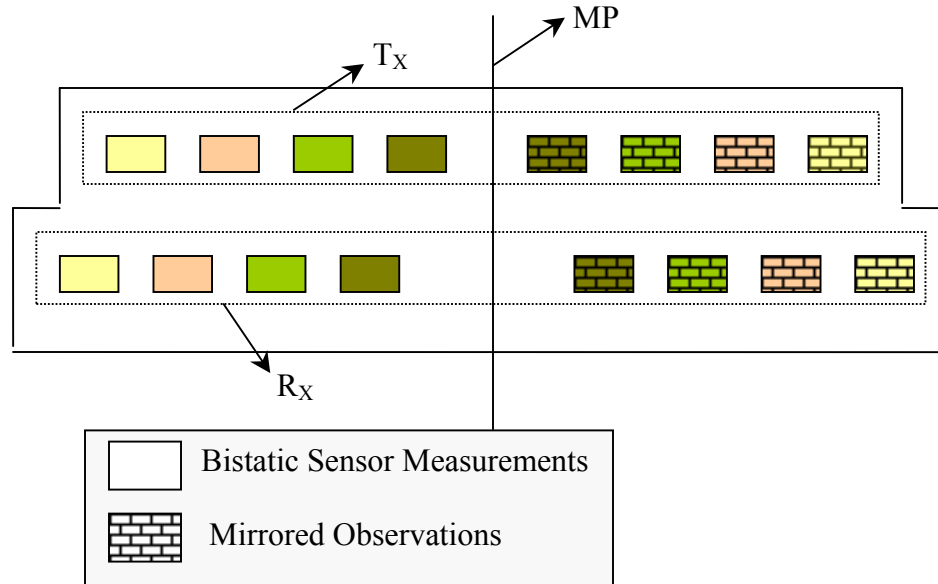


**Figure 4.1.2: A model for a multiple sensor geometry hand-held detector. Each color indicates a different sensor geometry. Each sensor geometry has a pair of bistatic measurements.**

If all the four  $m$  coefficients are small when the measurement plane aligns with the target reflection symmetric plane, the subsurface target is declared as a mine. If majority of the  $m$  values are high then the target can be declared as clutter (asymmetric). But are four  $m$  values a good representation of the level of symmetry in the subsurface target?

The larger the number of  $m$  values, the higher the confidence level in classifying subsurface targets as mines or clutter objects. For example, if 25 different sensor geometries are considered, this results in 25  $m$  values that can be used for

target classification. If the target is symmetric, all the 25  $m$  values will be ideally very low, whereas if the target is asymmetric, all the 25  $m$  values will definitely not be very low and no specific pattern in the  $m$  values will be observed. Therefore the target can be classified as symmetric or asymmetric based on these  $m$  values with a high level of confidence.

For this to be implemented in a hand-held sensor, 50 transmit antennas and 50 receive antennas have to be used to construct the multiple sensor geometry hand-held detector as shown in Figure 4.1.2. This increases the hardware complexity and also leads to a huge investment in hardware. The other option is to use a single sensor geometry hand-held detector, change the sensor geometry and scan again. As the number of sensor geometries increases, this method proves to be very time consuming. Is there an efficient method of collecting an adequate amount of data that can be processed and analyzed to decide whether the subsurface target is symmetric (landmine) or asymmetric (clutter) with a high level of confidence?

## **4.2 Data Collection Scheme**

As detailed in the previous section, adequate data need to be collected so that the subsurface target can be classified as symmetric or asymmetric with a high level of confidence. Using the multiple sensor geometry hand-held model, data can be collected for many sensor geometries, but the downside of such a model is hardware complexity and cost. Moreover, if such a model is used to reduce the false-alarm rate, the purpose of using a hand-held detector is defeated as a hand-held detector using

multiple sensor geometries will no longer be compact and simple. Both solutions proposed to address the issue of target classification with high level of confidence seem to have a disadvantage. Is there no solution to this problem? There is one and it lies in developing an efficient data collection scheme. The data collection scheme proposed should greatly reduce the complexity and also be in a position to synthesize the multiple sensor geometry hand-held detector.

On close observation of Figure 4.1.2 (which depicts the multiple sensor geometry hand-held model), it can be seen that the bistatic sensor measurements to the left of plane MP can be collected using a single bistatic sensor configuration ( $T_X$ - $R_X$ ). This is because the bistatic measurements collected on the left side of the plane MP are different only in the sense that one measurement is just a spatially shifted version of the other. All the bistatic measurements to the left of the plane MP can be collected by implementing the scan as shown in Figure 4.2.1.

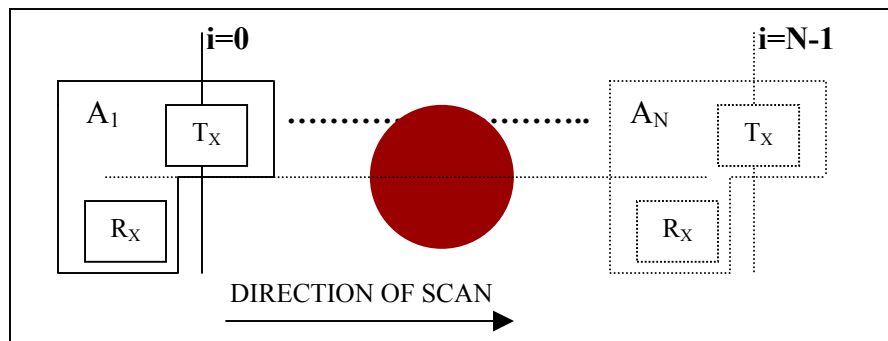


**Figure 4.2.1: A one-dimensional scan to collect the measurements to the left of the plane MP in Figure 4.1.2 using a single bistatic measurement,  $T_X$ - $R_X$ .**

For the scan shown in Figure 4.2.1, the bistatic sensor configuration ( $T_X$ - $R_X$ ) is named  $A_i$ , where  $i$  is the position of the bistatic measurement ( $A_i$ ) during the scan. The value of  $i = 0$  corresponds to the initial position of the bistatic sensor configuration.

Similarly, the bistatic measurements to the right of the plane MP in Figure 4.1.2 can be collected using a single scan as shown in Figure 4.2.2. For the scan

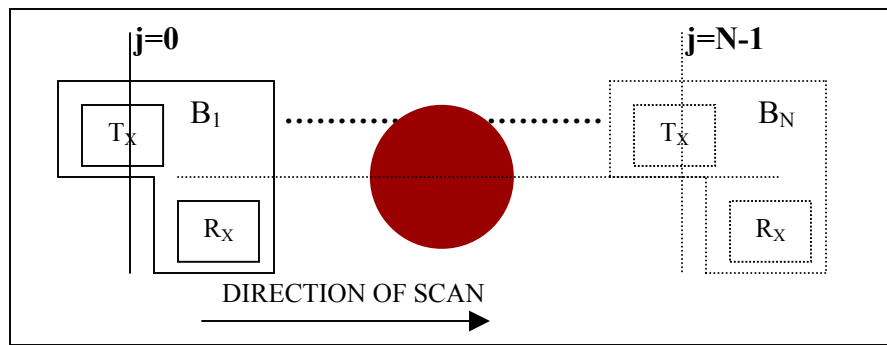


**Figure 4.2.2: A one-dimensional scan to collect the measurements to the right of the plane MP in Figure 4.1.2 using a single bistatic measurement,  $T_X$ - $R_X$ .**

shown in Figure 4.2.2, the bistatic sensor configuration is named  $B_j$ , where  $j$  is the position of the bistatic measurement ( $B_j$ ) during the scan.

The bistatic configurations shown in Figures 4.2.1 and 4.2.2 scan across (in the direction indicated in the figure), collecting  $N$  points with successive points separated by a user-defined step size  $\Delta x$  cm.

Therefore, the data collection scheme proposed collects all the required data with just two scans and two antennas! But by collecting the data using the scheme proposed, how can we reconstruct a multiple sensor geometry hand-held detector?

### 4.2.1 Simulating Multiple Sensor Geometry Hand-Held Detector

Having collected all the required data using the two scans as stated in Section 4.2, it remains to be seen how the measurements can be used to synthesize a multiple sensor geometry hand-held detector. It is time to define some variables for ease in analysis and understanding how a multiple sensor geometry hand-held detector can be synthesized.

The variable  $i$  in Figure 4.2.1 and variable  $j$  in Figure 4.2.2 indicate the location of the bistatic sensor configuration ( $T_X$ - $R_X$ ) in their respective scans. Let two other variables  $u$  and  $v$  be defined such that

$$\begin{aligned}u &= i - j \\v &= i + j\end{aligned}\tag{4.2.1.1}$$

The variable  $u$  gives the distance between the bistatic measurement  $A_i$  in Figure 4.2.1 and  $B_j$  in Figure 4.2.2. If one starts combining the measurements collected by both the scans to form mirrored bistatic observation pairs, then the magnitude of  $u$  gives the spacing between the bistatic measurements that constitute the mirrored bistatic observation pair being reconstructed. It is known that mirrored bistatic observation pairs in which the spacing between the bistatic measurements is fixed constitute a specific *sensor geometry*. Therefore the value of  $u$  can be used to identify sensor geometry. A set of mirrored bistatic observation pairs synthesized using the bistatic measurements from both the scans is said to have the same sensor geometry if the value of  $u$  computed using the math in (4.2.1.1) is constant. What does the value of  $v$  signify?

The magnitude of  $\frac{v}{2}$  is the average of the magnitudes of  $i$  and  $j$ . When trying to reconstruct a mirrored bistatic observation pair with the bistatic measurements  $A_i$  and  $B_j$ , a plane at the value  $\frac{v}{2}$  indicates the location of a plane exactly between  $i$  and  $j$ . This plane corresponds to the measurement reflection symmetric plane for the mirrored bistatic observation pair formed using  $A_i$  and  $B_j$ . In other words, the plane at location  $\frac{v}{2}$  is the measurement plane. Therefore the magnitude of the variable  $v$  uniquely identifies the measurement plane.

To explain how to reconstruct the multiple sensor geometry hand-held detector, assume that measurements have been collected by performing the scans as shown in Figures 4.2.1 and 4.2.2 (where the values of  $i$  and  $j$  range from 0 to  $N-1$ ). There exist values of  $i$  and  $j$  that yield the same values of  $v$  but different values of  $u$ . This implies that for a given measurement plane ( $v$ ) different sensor geometries ( $u$ ) could be reconstructed. A pictorial representation of the previous statement is shown in Figure 4.2.1.1. The Figure 4.2.1.1 is similar to a model described earlier in this chapter. What is it?

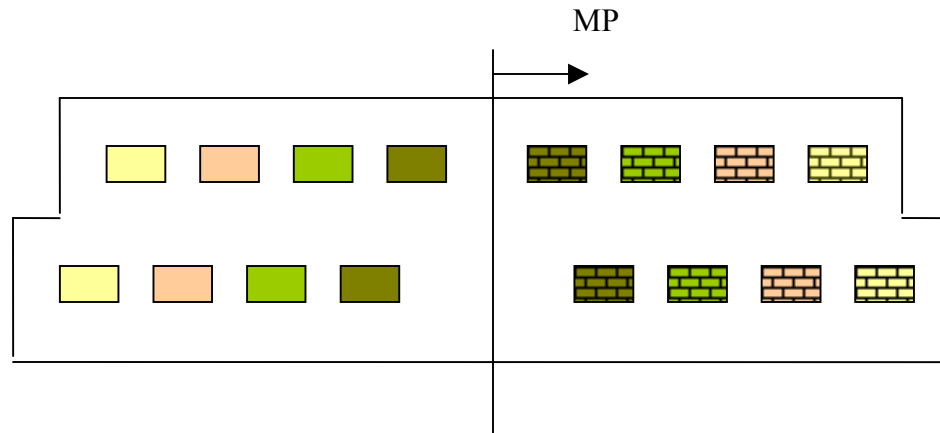


**Figure 4.2.1.1: Reconstructing multiple sensor geometries for a single measurement plane. In other words, using the data collection scheme the multiple sensor geometry hand-held detector can be synthesized.**

It is a multiple sensor geometry hand-held detector! Therefore, using the data collected, the multiple sensor geometry hand-held detector could be synthesized.

The next question is how many sensor geometries can be synthesized for a measurement plane? The answer to this question is it depends on the location of the measurement plane or the value of  $v$ . The maximum number of sensor geometries that can be synthesized for the value of  $v$  is defined by  $\frac{\min(v) + \max(v)}{2}$ . In the case of the scan shown in Figure 4.2.1 or Figure 4.2.2, the maximum number of sensor geometries (equal to  $N$ ) can be synthesized when  $v$  is equal to  $N$ , where  $N$  is the total number of points in the scan. The value of the variable  $v$  is reassigned such that the measurement plane for which the maximum number of sensor geometries can be synthesized has a value of  $v = 0$ . Therefore the value of  $v$  ranges from  $-N$  to  $N$ .

A pictorial representation of the number of sensor geometries that can be reconstructed as a function of the measurement plane is shown in Figure 4.2.1.2.

Therefore it has been shown that a multiple sensor geometry hand-held detector can be simulated with the data collection scheme.

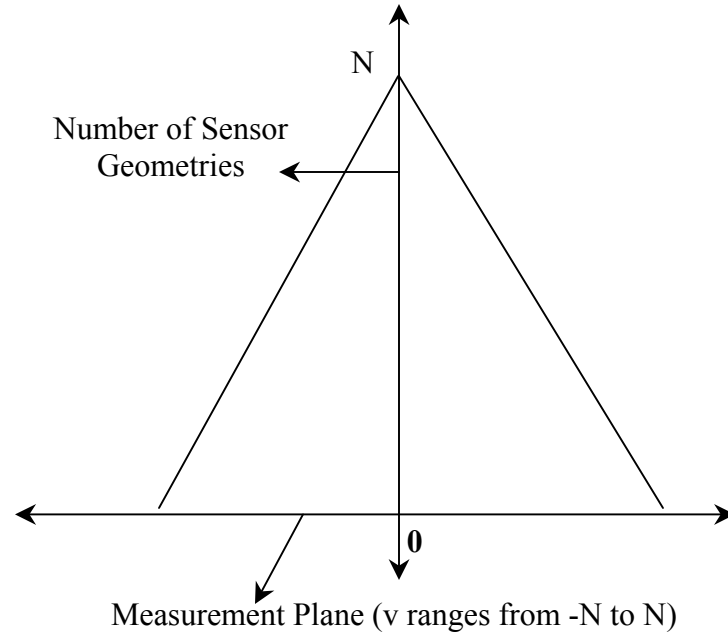


**Figure 4.2.1.2: Figure explaining the number of sensor geometries as a function of measurement plane. The scans performed collect N data points. The value of v ranges from -N to N (indication of measurement plane) and a maximum of N sensor geometries can be synthesized for the measurement plane, 0.**

On the other hand, there exists values of i and j that yield the same value of u but a different value of v. This implies that for a given sensor geometry (u) there exists a different measurement plane (v). The scenario is shown in the Figure 4.2.1.3, which resembles a model described earlier in this chapter. What is it?

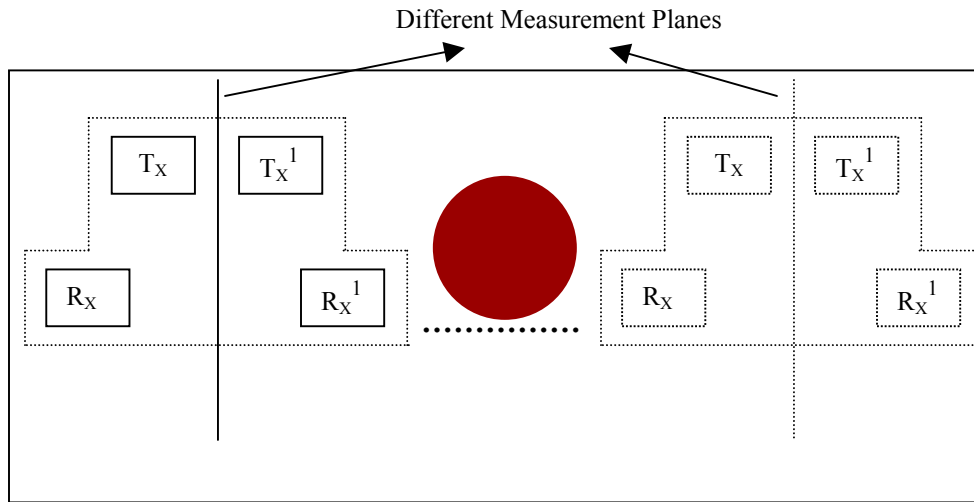


**Figure 4.2.1.3: A single sensor geometry that has multiple measurement planes is similar to the single sensor geometry hand-held detector described in Section 4.1.1.**

It is a single sensor geometry hand-held detector scanning across and collecting measurements! The sensor geometry indicated in Figure 4.2.1.3 is the same at both the measurement planes. Another scan with a different sensor geometry (than the one depicted here) has a different value of  $u$ . This is similar to changing the sensor geometry and scanning again!

Therefore for a single measurement plane, multiple sensor geometries can be synthesized and for a single sensor geometry there exist multiple measurement planes.

Thus the data collection scheme proposed is a potential solution to the problems

- of cost and complexity in the case of a multiple sensor geometry hand-held detector.
- of time in the case of repeating the scans with different sensor geometries.

One of the requirements for good results and symmetry measures is to preserve the symmetry in measurements collected. If there is an asymmetry in the measurements (caused by an error in positioning the bistatic sensor configurations in Figures 4.2.1 and 4.2.2), it will induce asymmetry in an otherwise symmetric target. To preserve the symmetry in the measurements, the planes indicated as  $i = 0$  in Figure 4.2.1 and  $j = 0$  in Figure 4.2.2 have to be aligned. Therefore, to collect the data, a precise positioning system should be used so that an error is avoided in moving the antennas with the desired step size. An error in positioning the antennas can lead to destroying the symmetry in the measurement and will lead to erroneous results.

#### **4.2.2 Data Collection System**

An efficient data collection scheme for synthesizing the multiple sensor geometry hand-held detector while avoiding the hardware complexity in the multiple sensor hand-held model has been put forth in Section 4.2. To implement the data collection scheme in laboratory and field experiments, two undergraduate students at the Radar Systems and Remote Sensing Laboratory (RSL), The University of Kansas, built a mobile machine. A picture of the mobile machine is shown in Figure 4.2.2.1.

The mobile machine is a structure that resembles a table, onto which is mounted a wooden plank. The wooden plank has holes drilled in it for allowing the antennas to be fixed onto it. The board is mounted in such a way that it can be moved



**Figure 4.2.2.1: Mobile machine used to collect data by implementing the scans detailed in Figures 4.2.1 and 4.2.2 and thereby simulate the hand-held detector.**

with the help of a motor. The complete data collection process is automated and the movement of the board is controlled using software. The input to the data collection program is the input file, which incorporates the step size  $\Delta x$  cm and the data points at which the data need to be collected. When the program is executed, the board moves from its initial position in increments of the step size defined by the user. Each data point in the input file causes the board to move from its initial position a distance equal to the step size times the data point values. For example, if the step size is 1 cm and one of the data points is 10, this point in the scan corresponds to a distance of 10 cm from the board's initial position. Using this setup the scan with bistatic sensor configuration ( $T_X-R_X$ ), as shown in Figure 4.2.1, is performed. To preserve the symmetry in the measurements, the board has to return to the initial position with high precision. After all the measurements for a specific scan have been collected, the board is forced by the program to return to a position within 1 mm of its initial

position. This high level of accuracy is obtained with the help of optical encoders. The bistatic sensor configuration is then changed so the other scan (as shown in Figure 4.2.2) can be performed. After performing both scans, the multiple sensor geometry and single sensor geometry hand-held detectors can be synthesized using the scanning measurements, as explained in Section 4.2.1.

Having collected the data, how can it be analyzed to detect the presence of a subsurface target and, more important, classify the subsurface targets as mines or clutter? What sort of results are expected?

### **4.3 Analysis of Data Collected**

Once the data have been collected, it then needs to be processed and analyzed so that the subsurface targets can be classified as symmetric and asymmetric targets with a high level of confidence. The goal of collecting radar measurements is to

- detect the presence of subsurface target and
- classify the subsurface target as a landmine or clutter based on the concept of symmetry.

The presence of the subsurface target can be confirmed by using the sum values ( $\sum$ ), and the target classification is based on  $m$  coefficients. In Section 4.2, it has been shown that for a single sensor geometry there exist multiple measurement planes and for a single measurement plane there exist multiple sensor geometries. The sum values and the  $m$  values can be calculated for each sensor geometry-measurement plane combination. This results in a matrix of sum values and  $m$  values.

Consider that the bistatic measurement at location  $i$  in Figure 4.2.1 (i.e.,  $A_i$ ) and the bistatic measurement at a location  $j$  from Figure 4.2.2 (i.e.,  $B_j$ ) can be combined to form a sensor geometry. Then, according to (2.3.2) the sum value can be written as

$$\Sigma(u, v) = \int |f_{A_i}(t) + f_{B_j}(t)|^2 dt \quad (4.3.1)$$

and the  $m$  value can be written as

$$m(\mathbf{u}, \mathbf{v}) = \frac{\int |f_{A_i}(t) - f_{B_j}(t)|^2 dt}{\int |f_{A_i}(t) + f_{B_j}(t)|^2 dt} \quad (4.3.2)$$

In (4.3.1) and (4.3.2)  $u$  and  $v$  are defined as in (4.2.1.1) and are indicators of the sensor geometry and measurement plane. Equation (4.3.1) represents a matrix of sum values in which each entry is a sum value for a specific sensor geometry-measurement plane combination. Similarly, (4.3.2) can be used to form an  $m$  value matrix. In both the sum value and  $m$  value matrices the rows indicate different sensor geometries and the columns indicate different measurement planes. All the values in a single row in either the sum or  $m$  value matrix correspond to a single sensor geometry but for different measurement planes. This approximates having a single sensor geometry fixed and scanning across. On the other hand, all the values in a column in either the  $m$  or sum value matrix correspond to a single measurement plane but for different sensor geometries. This is similar to a multiple sensor geometry hand-held detector.

A diagrammatic representation of the matrix of either sum values or  $m$  coefficients is shown in Figure 4.3.1. The horizontal axis is the measurement plane and the vertical axis is the sensor geometry. Figure 4.3.1 is actually an  $m$  or sum

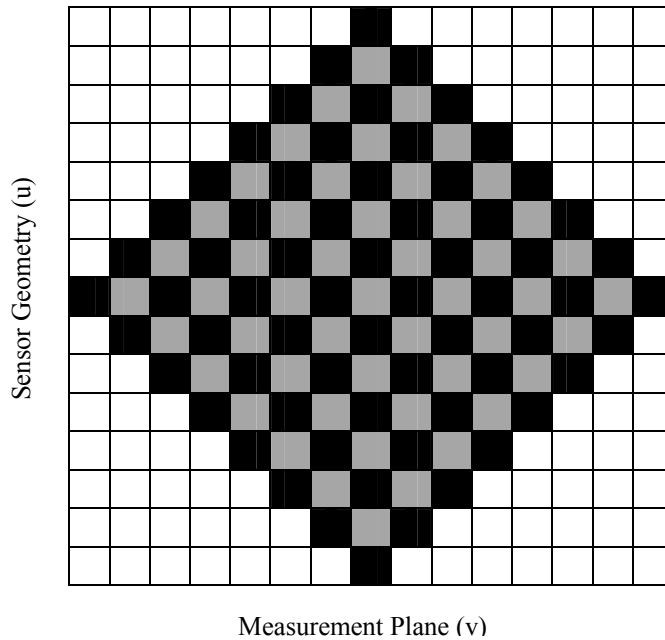


**Figure 4.3.1: A diagrammatic representation of either the sum or  $m$  value matrices for a few measurements collected using the two scans in Figures 4.2.1 and 4.2.2. The black cells indicate all the possible sensor geometries for all the measurement planes. The cells color coded as gray are obtained by performing a linear interpolation. The interpolation makes the matrices continuous.**

matrix only for a few measurements collected using the scans in Figures 4.2.1 and 4.2.2. The black cells in Figure 4.3.1 indicate the presence of an  $m$  or sum value for that specific sensor geometry-measurement plane combination. These black cells indicate all possible sensor geometries that can be synthesized for all the measurement planes for the given set of data. The gray cells are the  $m$  and sum values obtained after a linear interpolation. This interpolation must be performed to obtain a

smooth matrix of sum and  $m$  values that can later be used for visual interpretation of the results.

For detecting the presence of the subsurface target, the sum value ( $\Sigma$ ) matrix will be used. The presence of a subsurface target is reflected as high sum values for some measurement planes in close proximity to the target. The sum values should be high irrespective of the level of symmetry in the subsurface target (whether the subsurface target is a landmine or clutter). If the subsurface target is a landmine, the  $m$  coefficients will be very low for a single measurement plane and for almost all the sensor geometries. If the subsurface target is clutter, the  $m$  values should vary from low to high values with no specific pattern. The  $m$  value or sum value matrices can be used in many ways to analyze the results; this will be detailed in Chapter 5.

In this chapter the possibility of implementing a hand-held detector, which uses GPR to classify subsurface targets as clutter objects or mines based on the concept of reflection symmetry, has been investigated. A theoretical foundation along with the data collection scheme has been detailed. This methodology must be validated and tested. The best validation for the hand-held model is to conduct controlled experiments in the laboratory. Experiments were conducted using different targets in the sandpit. The data were collected using the mobile machine and analyzed as discussed in Section 4.3. Are the results obtained conclusive enough to differentiate between the mines and clutter objects?

## Chapter 5

### Experiments and Results

The possibility of implementing a hand-held detector that uses GPR to detect and classify subsurface targets as mines or natural clutter based on the symmetry in the subsurface target was investigated in Chapter 4. The question this chapter tries to answer is whether the results obtained from the experiments are as expected and, more important, are the results conclusive with regard to subsurface target detection and target classification. To answer these questions different experiments were conducted, first in the laboratory (sandpit) and then at the Ft. A.P. Hill test site in Virginia, during August 2001.

The raw data collected will help very little in extracting the electromagnetic signature of the subsurface target and therefore must be processed before it can be subjected to further analysis. How are the raw data processed so they can be used to make conclusive decisions about subsurface targets?

#### 5.1 Data Processing

The raw data obtained by performing the scans as described in Section 4.2 are a function of frequency. The network analyzer measures the  $S_{21}$  parameter for 201 different frequencies in the bandwidth of operation (2 GHz – 6 GHz), which are separated by the frequency step size  $\Delta f = 20\text{MHz}$ . To collect the radar measurements and to simulate the hand-held detector, two scans (detailed in Section 4.2) need to be performed. Both scans use the same input to the program, which positions the board

and collects data. Once the radar measurements have been recorded, they need to be processed for further analysis.

The first step in processing the raw data is to obtain the scattering as a function of time. A Hamming window is used on the frequency-domain data (to reduce the time-domain side lobes due to the dominant scatterer) prior to matched-filter processing. The radar response as a function of time is obtained by correlating the raw data with the expected response. This operation of correlation is nothing but a matched-filter operation. The program for performing the matched-filter processing was written in MATLAB.

It has been already shown that the data collected using the data collection scheme detailed in Section 4.2 allow the reconstruction of all possible sensor geometries for all measurement planes. Using the math detailed in Section 4.3, the  $m$  value and sum value matrices can be formed. Each row in this matrix represents different sensor geometry and each column represents a distinct measurement plane. The matrix obtained is discontinuous and a linear interpolation is performed. Thus after interpolation, smooth and continuous  $m$  value and sum value matrices are obtained. Using MATLAB, color coded plots of the  $m$  coefficient and sum value matrices can be generated.

The data processing steps discussed above have been used to process the raw data from the experiments and the results obtained are presented in the form of color coded plots for better interpretation in the following sections.

## 5.2 Experiments and Results

The mobile machine as described in Chapter 4 was used for collecting data in the sandpit and also in the field experiment in Ft. A.P. Hill, Virginia, during August 2001. Experiments were first conducted in the sandpit with different targets that simulate mines and clutter targets. Targets at the test site included anti-personnel, anti-tank mines and natural clutter like wood. In this section, the experiments will be explained along with the characteristics of the targets used and the results obtained will be presented and discussed.

### 5.2.1 Experiments in Sandpit

Experiments in the sandpit involved collecting data using the mobile machine on symmetric and asymmetric targets. The symmetric target used was a Styrofoam disc, and it was buried at a depth of approximately 8 cm below the ground. The picture of the Styrofoam disc is shown in Figure 5.2.1.1 and its physical properties are detailed in Table 5.2.1.1.



**Figure 5.2.1.1: Picture of the Styrofoam disc used to simulate a symmetric landmine in the sandpit experiments.**

**Table 5.2.1.1 Physical Properties of the Styrofoam Disc**

Physical Property	Value for the Styrofoam Disc
Diameter	14.73 cm
Height	3.17 cm
Weight	50grams
Dielectric Constant	$\approx 1.02$

The board with the antennas, which is mounted on the mobile machine, was programmed to move in steps of 1 cm and collects 66 data points from its initial position. The two scans detailed in Section 4.2 were performed to collect the required data to synthesize a hand-held detector.

In a similar manner data were also collected on an asymmetric target. The asymmetric target used was a crushed milk jug, shown in Figure 5.2.1.2. The milk jug is made out of plastic and for the experiment it was buried approximately 8 cm below the surface of the ground.



**Figure 5.2.1.2: Picture of a crushed milk jug used to simulate a clutter target in the sandpit experiment.**

The data collected for both targets (i.e., the Styrofoam disc and crushed milk jug) were processed using the data processing steps detailed in Section 5.1 and the  $m$  value and sum value matrices were formed. When analyzing the results, two questions need to be answered.

- Is there a target beneath the ground?
- If there is a subsurface target, is it a mine (symmetric object) or a clutter target (asymmetric object)?

The MATLAB plots generated using the interpolated sum matrix for the Styrofoam disc are shown in Figure 5.2.1.3(a). The plots are color coded such that the dark blue indicates the lowest value and dark red, the highest value in the matrix. The vertical axis on the plots corresponds to different sensor geometries (as detailed in Section 4.3) and the horizontal axis corresponds to the measurement plane. The number zero on the horizontal axis corresponds to the measurement plane for which maximum number of sensor geometries could be synthesized with the available set of data. This measurement plane corresponds to the average of the first and last data points in the input file. All other measurement planes have a lesser number of sensor geometries.

To detect the presence of a subsurface target, the sum value matrix will be used. If the target is indeed present, this will be reflected as high sum values for some measurement planes that are close to the location of the target. In the MATLAB plots the high values are color coded in dark red. The sum value plot for the Styrofoam disc is shown in Figure 5.2.1.3 (a). From this Figure, it can be seen that there exist high

sum values (indicated by dark red pixels) for sensor geometries ranging from  $-10$  to  $+5$  and for measurement planes in the range of  $-5$  to  $+5$ . These sensor geometries ( $-10$  to  $+5$ ) are the ones in which the spacing between the two bistatic measurements (which constitute the sensor geometry) is small.

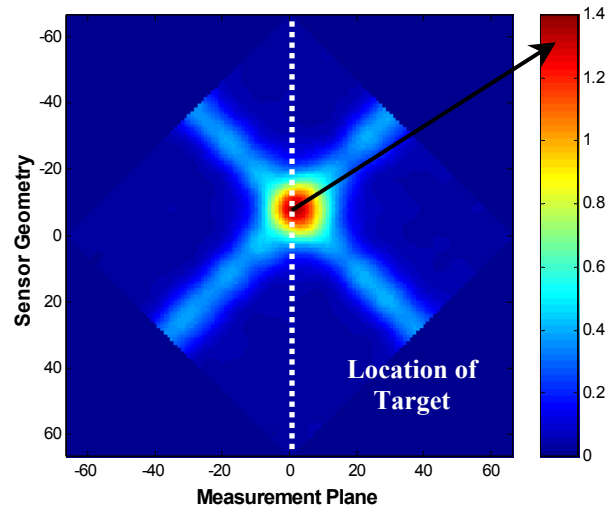


**Figure 5.2.1.3(a):** Sum plot for the Styrofoam disc with the indication of an approximate location of target based on the energy scattered from the subsurface target.

Therefore the presence of high values in the sum plot indicates the presence of a subsurface target. To restate, *the measurement plane for which the sum values are high gives an approximate location of the subsurface target*. From the sum plot in Figure 5.2.1.3(a), the target is located at a measurement plane in the region  $-5$  to  $+5$ . Therefore, it can be concluded that a subsurface target is present and its approximate location has also been obtained using the sum plot. Now we need to discover if the target is symmetric or asymmetric.

For classifying the subsurface target, the  $m$  value matrix will be used. Having established the approximate location of the target (from the sum plot), the plane of

target symmetry (if the subsurface target is symmetric) should be in the vicinity of the approximate location of the target. Therefore, one of the measurement planes in the region  $-5$  to  $+5$  should align with the target reflection symmetric plane (if the subsurface target is symmetric). For a symmetric target, when the measurement plane aligns with the target reflection symmetric plane, the  $m$  values for all the sensor geometries should have a low magnitude. What are the results expected for a symmetric Styrofoam disc? In the  $m$  plot one of the measurement planes in the range  $-5$  to  $+5$  should have very low symmetry measures for all the sensor geometries.

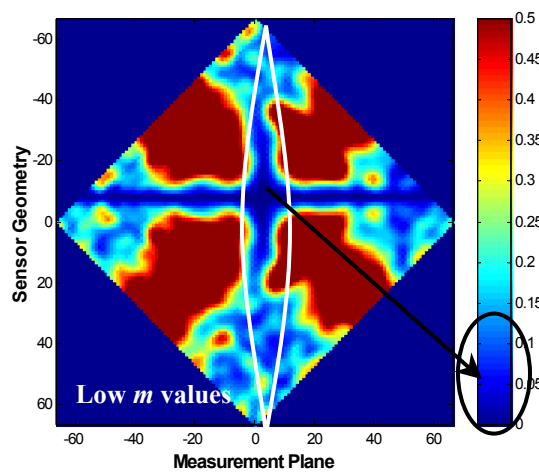


**Figure 5.2.1.3(b):  $m$  plot for the Styrofoam disc with indication of the measurement plane that has low  $m$  values for almost all sensor geometries. Hence the target can be classified as a symmetric target.**

It can be seen from Figure 5.2.1.3(b), the  $m$  plot for the Styrofoam disc, that almost all the sensor geometries for a measurement plane in the range  $-5$  to  $+5$  have low  $m$  coefficients. Therefore the target could be detected as a symmetric object.

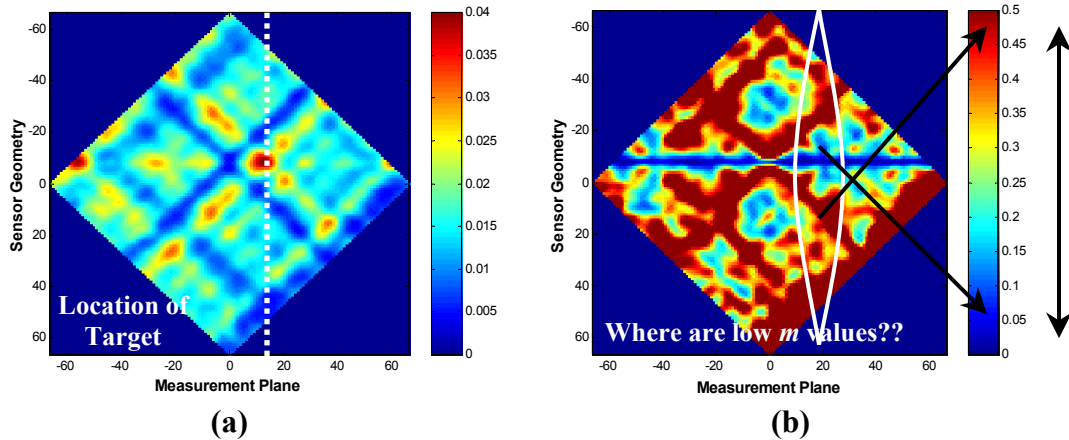
But there is one problem! Ideally, all the sensor geometries should have low symmetry measures when the measurement plane aligns with the plane of target

symmetry. But this is not the case with the  $m$  plot shown in Figure 5.2.1.3(b). It can be seen that the symmetry measures for the sensor geometries greater than 30 and lesser than  $-40$  are not as low as those for the other sensor geometries (e.g., sensor geometries in the range  $-40$  to 20). For sensor geometries greater than 30, the spacing between the two bistatic observations that constitute the sensor geometry is large (in comparison with other sensor geometries). With the measurement plane of symmetry aligned with the target reflection symmetric plane, the target will not be in close proximity to the bistatic measurements that constitute the sensor geometries greater than 30 or lesser than  $-40$ . Because of this reason, the scattering from the subsurface target will be weaker and the calculated sum value will not be as high as the sum values for other sensor geometries. In other words, the Signal-to-Noise Ratio (SNR) degrades. A decrease in the value of the sum has the effect of increasing the magnitude of the  $m$  coefficients. Therefore, some sensor geometries do not contribute significantly toward target classification.

The two requirements for developing an efficient landmine detection scheme (i.e. detecting the presence of a subsurface target and, more important, classifying it as symmetric) have been satisfied.

It remains to be seen whether the measurements on the crushed milk jug indicate that the subsurface target is asymmetric. The symmetry measure plot and sum value plot for the clutter target (crushed milk jug) are shown in Figure 5.2.1.4. If an object is buried beneath the ground, then the sum values should be high for some

measurement planes irrespective of whether the subsurface target is symmetric or asymmetric.



**(a)** Figure 5.2.1.4(a): Sum plot for crushed milk jug is shown in (a). Indicated on the sum plot is approximate location of the target.  $m$  plot for crushed milk jug is shown in (b). Note absence of measurement plane with low symmetry measures for all sensor geometries.

From the sum plot it can be inferred that high sum values exist for the measurement planes in the range 8 to 15 and sensor geometries in the range  $-10$  to  $0$ . This indicates the presence of a subsurface target, and the approximate location of the target is also indicated in (a). If the target were symmetric, then at least one of the measurement planes in the range 8 to 15 (where the sum values are high) should have low symmetry measures for almost all the sensor geometries. This is not the case, and it can be seen from the  $m$  plot for the crushed milk jug in (b) that no measurement plane exists for which the  $m$  coefficients are low for almost all the sensor geometries. Moreover, the measurement plane in the vicinity of the approximate location of the target has  $m$  values that range from low to high value for almost all the sensor geometries (as shown in (b)). Therefore, the measurements reveal the presence of a subsurface target (crushed milk jug) and it can be classified as an asymmetric target.

Thus, using GPR, the subsurface targets can be classified as symmetric and asymmetric.

Observation of the  $m$  plot for the Styrofoam disc in Figure 5.2.1.3(b) and the  $m$  plot for the crushed milk jug in Figure 5.2.1.4(b) shows there are a few sensor geometries (in the range  $-12$  to  $-8$ ) for which the symmetry measures are very low, irrespective of the measurement plane and the subsurface target. This is reflected in the symmetry measure plots for both the crushed milk jug and Styrofoam disc as a horizontal dark blue line for the few sensor geometries centered around  $-10$ . What is the reason for this?

One of the sensor geometries that yields low  $m$  values for all the measurement planes, irrespective of symmetry in the subsurface target, is shown in Figure 5.2.1.5(a). In this figure bistatic measurements  $T_X-R_X$  and  $T_X^1-R_X^1$  are mirror

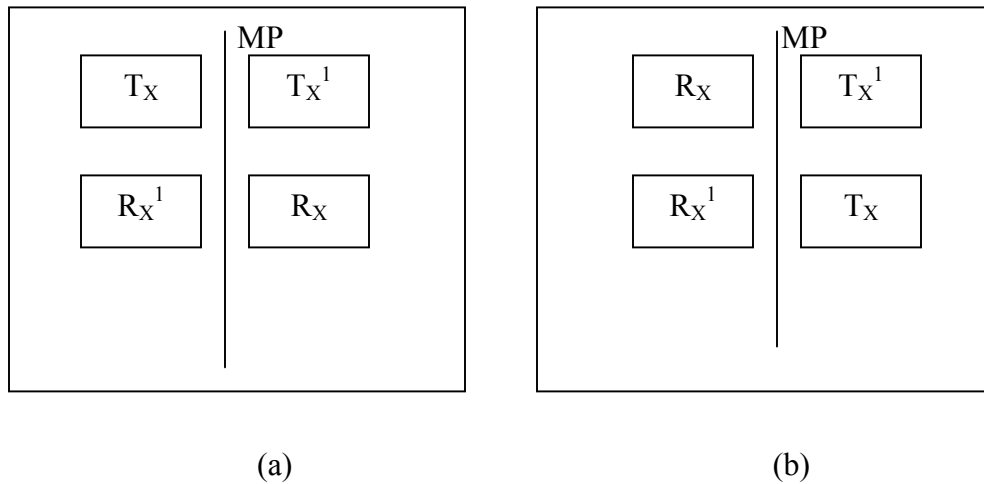


**Figure 5.2.1.5 (a): A sensor geometry for which the symmetry measure is very low for all the measurement planes irrespective of whether the subsurface target is a mine or clutter. (b) The sensor geometry depicted in (a) with  $T_X-R_X$  replaced with its reciprocal measurement.**

images across the plane MP, which is not the target reflection symmetric plane. By principle of reciprocity, the measurements obtained by  $T_X-R_X$  and its reciprocal configuration are identical. On keen observation, it can be inferred that the reciprocal bistatic measurement of  $T_X-R_X$ , which is shown in Figure 5.2.1.5 (b), is not very different from the bistatic measurement  $T_X^1-R_X^1$ . By invoking the identity property, the measurements obtained using the bistatic configurations in Figure 5.2.1.5(b) are identical. Therefore, by using the two properties of reciprocity and identity, the bistatic measurements ( $T_X-R_X$  and  $T_X^1-R_X^1$ ) in Figure 5.2.1.5 (a) are almost identical. Since the bistatic measurements are identical, the  $m$  coefficient computed using (2.4.1) is very low, irrespective of the measurement plane and the subsurface target.

For comparison purposes another sensor geometry is considered for which the  $m$  coefficient is a low value only when the measurement plane aligns with the plane of target symmetry. One such sensor geometry is shown in Figure 5.2.1.6.

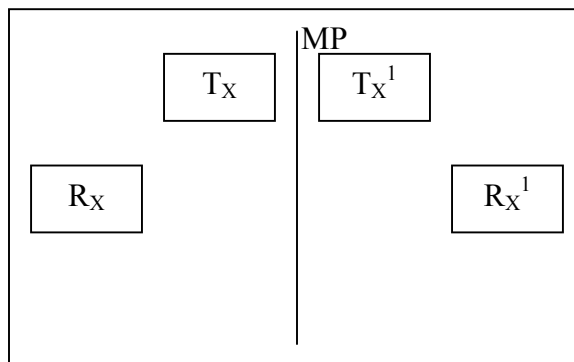


**Figure 5.2.1.6: Sensor geometry for which  $m$  coefficient is small only when the measurement plane aligns with plane of target symmetry and the subsurface target is symmetric.**

The reciprocal bistatic measurement for the bistatic pair  $T_X$ - $R_X$  is shown in Figure 5.2.1.7 and is significantly different than the bistatic measurement  $T_X^1$ - $R_X^1$ ; hence the two bistatic measurements in Figure 5.2.1.7 will be identical (within measurement error and noise) only when the subsurface target is symmetric and MP is aligned with the plane of target symmetry.

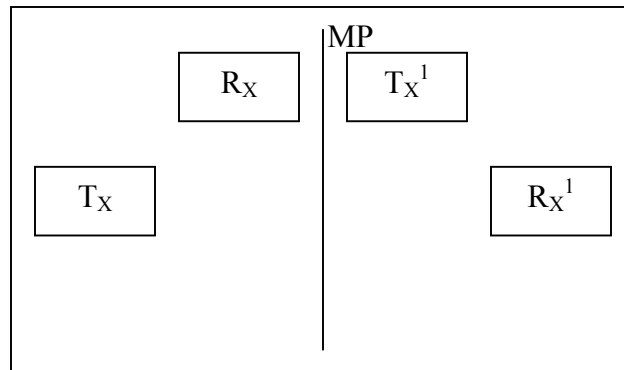


**Figure 5.2.1.7: Sensor geometry as described in Figure 5.2.1.6 with  $T_X$ - $R_X$  replaced with its reciprocal measurement.**

Therefore, using the concept of reciprocity and identity, the reason why the  $m$  values for some sensor geometries are low for all measurement planes has been explained.

Another experiment was conducted in the sandpit with the target being natural clutter, a rock. This experiment is also very crucial because it will test the capability of the detection scheme to find a natural clutter object and classify it as an asymmetric target.

The rock used for the sandpit experiments is shown in Figure 5.2.1.8. The rock is about the size of the Styrofoam disc but weighs close to 500gms. The rock

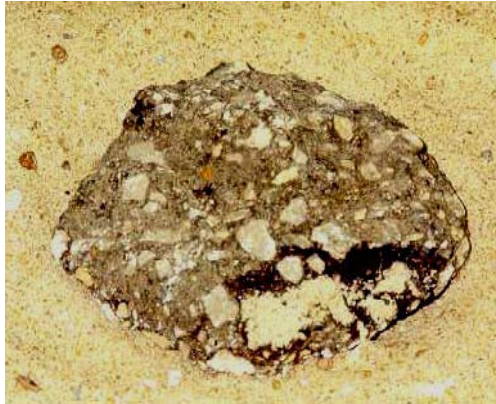


**Figure 5.2.1.8: Picture of a rock used in laboratory to simulate natural clutter targets in the sandbox experiments.**

was buried close to 8 cm below the ground and the required data were collected by performing the two scans as described in Section 4.2. The input data file was the same as used for the Styrofoam disc and the crushed milk jug; i.e., scanning and collecting 66 data points separated by 1 cm starting from the board's initial position. The data were processed following the data processing steps as described in Section 5.1, and the final results were the  $m$  and the sum plots, which are shown in Figure 5.2.1.9 along with the  $m$  and sum plots for the Styrofoam disc.

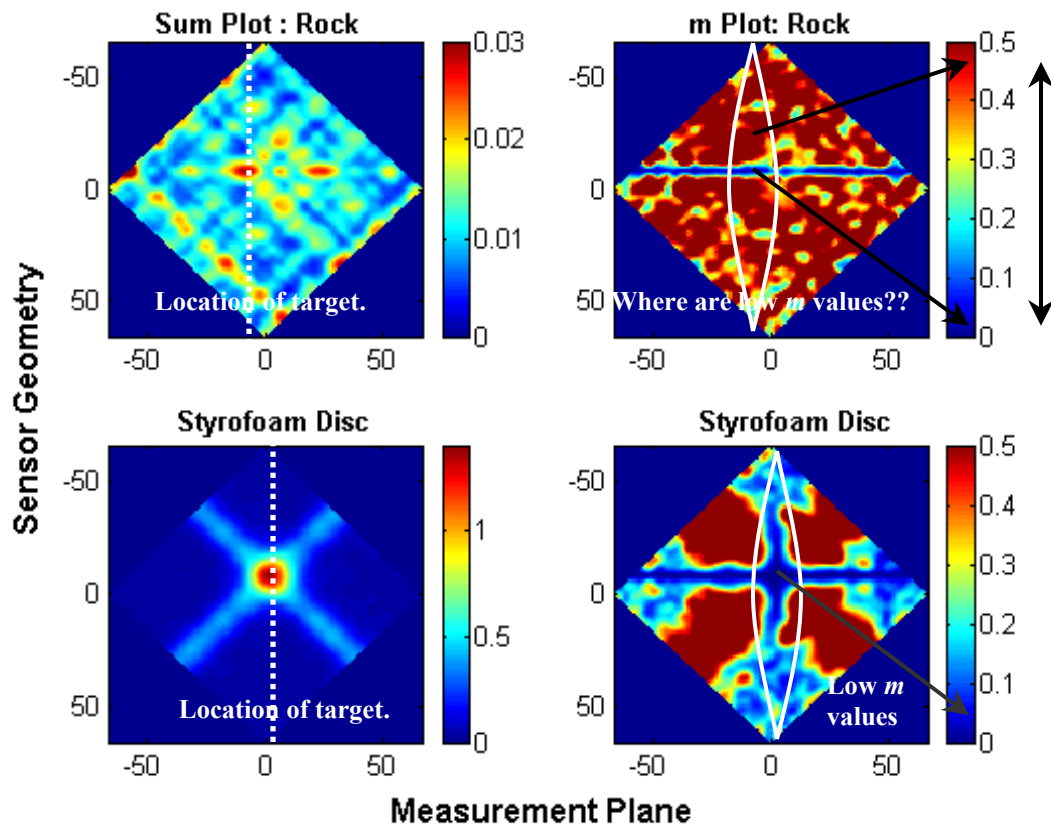


Figure 5.2.1.9: Sum and  $m$  plots for rock and Styrofoam disc. By comparing the  $m$  plots for the rock and Styrofoam disc, it can be seen that the rock can be classified as an asymmetric target and the Styrofoam disc can be classified as symmetric target.

It can be inferred from the sum and  $m$  plots for the rock that the presence of high sum values at some measurement plane indicates the presence of a subsurface target (as indicated in the sum plot for the rock). But the absence of any distinct measurement plane with low  $m$  coefficients for almost all sensor geometries indicates that the subsurface target is asymmetric. In the  $m$  plot for the rock, the  $m$  values for the measurement planes in the vicinity of the target location range from low to high values for almost all sensor geometries. This indicates that the subsurface target is a clutter object.

Thus, the experiments in the sandpit proved that GPR can be used in hand-held detectors to detect and classify subsurface targets such as, mines and natural clutter based on the concept of symmetry. An efficient data collection scheme, which was put forth in Chapter 4, has been implemented and tested in the laboratory (Sandpit). The mobile machine was taken on the field trip to collect data at the Ft. A.P. Hill test site in Virginia during August 2001. The results obtained by processing the data collected during the field experiment are explained in the next section.

### **5.2.2 Results from Field Experiment**

During August 2001, experiments were conducted at Ft. A. P. Hill, Virginia, to test the concept developed to detect and classify subsurface targets as mines or clutter based on the level of symmetry in the subsurface targets. The targets on which data were collected were anti-tank mines, anti-personnel mines and some clutter objects. Data collected on different targets were processed using the data processing steps discussed in Section 5.1 to generate color coded plots for the  $m$  coefficients and sum value matrices. Results obtained from processing the data that were collected on an anti-personnel mine (PMA-3) and irregular wood will be compared and discussed in this section.

The anti-personnel mine for which results will be presented is a PMA-3. A picture of the PMA-3 mine is shown in Figure 5.2.2.1. The physical properties of the mine have been reproduced from [8] and are shown in Table 5.2.2.1.



**Figure 5.2.2.1: PMA-3 an anti-personnel mine on which data were collected during field experiment at Ft. A.P. Hill, Virginia. Reproduced from [8].**

Such anti-personnel mines are generally found in Bosnia and Kosovo[8]. Another interesting point to note about the target PMA-3 is that it has very little metal content. Therefore, the metal detectors might be inefficient for detecting the PMA-3 mine. Hence, this target is a good test for the detection scheme based on the concept of symmetry. The target was buried at a depth of 4 cm.

**Table 5.2.2.1 Physical Properties for PMA-3. Reproduced from [8]**

Physical Property	Value for the PMA-3
Diameter	103mm
Height	36mm
Weight	183grams
Casing	Plastic
Detectability	Yes! But very low metal content
Sensitivity	3kg pressure

Since the anti-personnel mine is small, the step size for moving the board while collecting data was defined as 0.5 cm. The main reason for reducing the step size is that while scanning, the target reflection symmetric plane will not be missed. The data collection was concentrated around the location of the mine. The first data point was 34 steps from the initial position of the board, which corresponds to 17 cm relative to the initial position of the board. From this point, the board is moved in steps of 0.5 cm till it reaches 51 cm relative to the initial position of the board. The  $m$  plot and sum plot for the PMA-3 mine are shown in Figure 5.2.2.2. The horizontal axis in the  $m$  and sum plots denotes the measurement plane and the number zero corresponds to the measurement plane across which the maximum number of sensor geometries could be synthesized using the available data set.

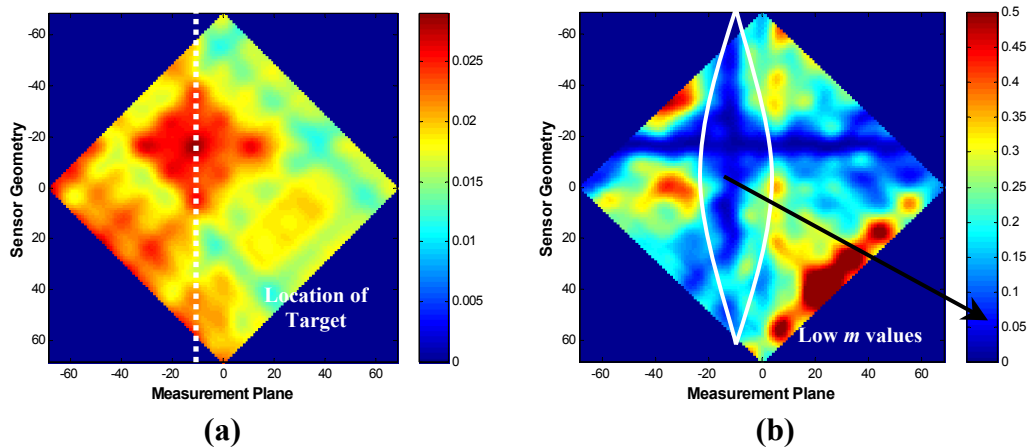


**Figure 5.2.2.2 (a): Sum plot for PMA-3. Indicated on the plot is the approximate location of the subsurface target. (b)  $m$  plot for PMA-3. Measurement plane shows low symmetry measures for almost all sensor geometries. This is an indicator that the subsurface target is a landmine.**

The sum plot for the anti-personnel mine PMA-3 is shown in Figure 5.2.2.2(a). In it, high sum values for the measurement plane in the range  $-40$  to  $+10$

and sensor geometries in the range  $-40$  to  $+15$  indicate the presence of a subsurface target. The location of target is indicated in the sum plot. The symmetry measure plot for the PMA-3 is shown in Figure 5.2.2.2(b). The  $m$  plot has a measurement plane in the region  $-20$  to  $-10$  (for these measurement planes sum values are also high), which have low  $m$  values for almost all the sensor geometries. This indicates that the subsurface target is symmetric and hence the target is classified as a mine. How does the detection scheme perform on irregular wood, a natural clutter target?

One of the natural clutter targets from the field experiment is irregular wood. The data were collected by moving the board in steps of 1 cm, the first data point being the initial position of the board. The total number of data points collected was equal to 67. The  $m$  and sum plots for irregular wood are shown in Figure 5.2.2.3.

The sum plot for the irregular wood indicates the presence of high sum values, as shown in Figure 5.2.2.3(a). This indicates the presence of a subsurface target and also an approximate location of the subsurface target in the sum plot. The  $m$  plot, (b), for the irregular wood indicates that a distinct measurement plane with low  $m$  values does not exist for almost all sensor geometries. For measurement planes in the vicinity of the target, the  $m$  coefficients range from low to high values.

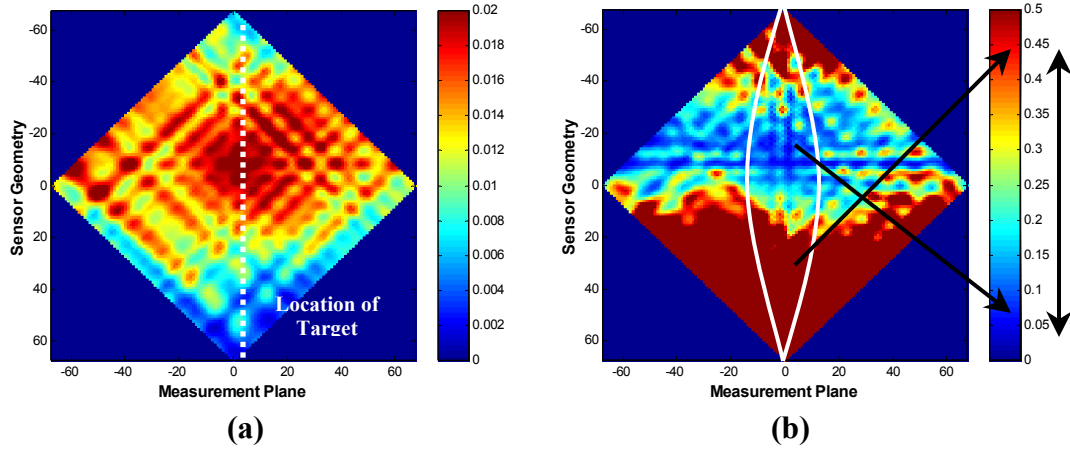


**Figure 5.2.2.3(a):** Sum plot for irregular wood, a natural clutter target. Approximate location of the target is indicated in sum plot. **(b)  $m$  plot** for irregular wood. There is no measurement plane with low  $m$  values for almost all the sensor geometries.

Although there are many values in the  $m$  plot that are low, they do not all correspond to a specific measurement plane. Therefore, it can be concluded from the  $m$  plot that the subsurface target is asymmetric and hence is clutter.

The results from the field experiment prove, as did laboratory experiments, that the GPR can be used to detect and classify subsurface targets such as mines or clutter based on the concept of symmetry. Therefore, GPR with target classification based on the symmetry in subsurface targets can be used to develop landmine detection schemes with significantly low  $P_{FA}$ .

There were some targets for which the sum plots were not conclusive with regard to detecting the presence of a subsurface target. Looking at these sum plots, one could easily see some scattered energy but could not declare that a subsurface target was present with a high level of confidence. Can this uncertainty be resolved?

### 5.3 Sensor Array

To resolve the uncertainty with regard to detecting the presence of a subsurface target, the data collected from the scans (as shown in Figures 4.2.1 and 4.2.2) will be processed in a manner that will simulate an array of sensors. The sensor array can be formed by combining different sensor measurements, and the composite measurement of the sensor array is the coherent addition of all the sensor measurements that constitutes the array. The main motive of processing the data by adding several sensor measurements coherently is to improve subsurface target detection.

To form a K-element sensor array, K successive bistatic measurements obtained during a scan performed as in Figure 4.2.1 can be combined coherently to result in a composite measurement as shown in (5.3.1)

$$\mathbf{x}_{A_i}^c = \sum_{k=i}^{i+K-1} \mathbf{x}_{A_k} \quad (5.3.1)$$

where the value of i indicates the location of the bistatic sensor measurements. Similarly a composite measurement of combined K measurements obtained by performing the scan as shown in Figure 4.2.2 is defined by (5.3.2)

$$\mathbf{x}_{B_j}^c = \sum_{k=j}^{j+K-1} \mathbf{x}_{B_k} \quad (5.3.2)$$

where the value of j indicates the location of the bistatic sensor configuration during the scan.

The  $m$  value and sum value matrices can be formed as detailed in Section 4.3. But the only difference is that the radar measurements used are a composite measurement of the sensor array with  $K$  elements.

One of the targets from the Ft. A.P. Hill field experiments, VAL-69, an anti-personnel mine, which had uncertainty with respect to target detection, was processed with sensor arrays of different sizes (e.g., 1, 4, 8 or 16 sensors in an array). The sum plots, which indicate the presence of a subsurface target, are shown in Figure 5.3.1. It can be inferred from the figure that it is far more conclusive to form a decision about a presence of the subsurface target using sum plots with more sensors in the sensor

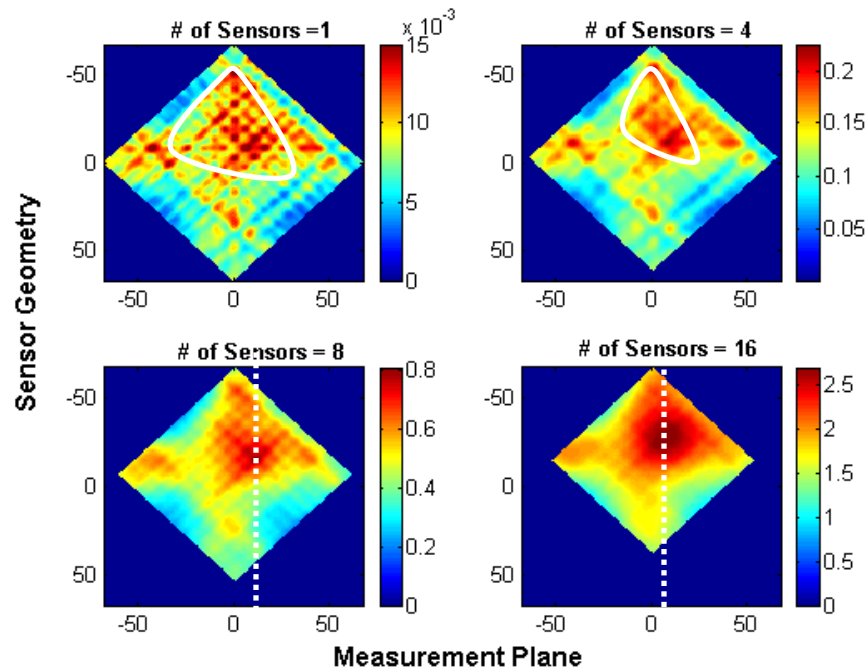


**Figure 5.3.1: Sum plots for different numbers of elements in the sensor array for target VAL-69. The sum plot with 16 elements in the sensor array detects the target with a high level of confidence.**

array. For the sensor array with a single element it is difficult to clearly locate the target since the high sum values are scattered all over the sum plot.

Using a sensor array with 16 elements, target presence can be established easily and the location of the subsurface target is shown. In Figure 5.3.1, sum plots obtained with sensor arrays with 8 and 16 sensors can be used to detect the presence of the subsurface target with a high level of confidence.

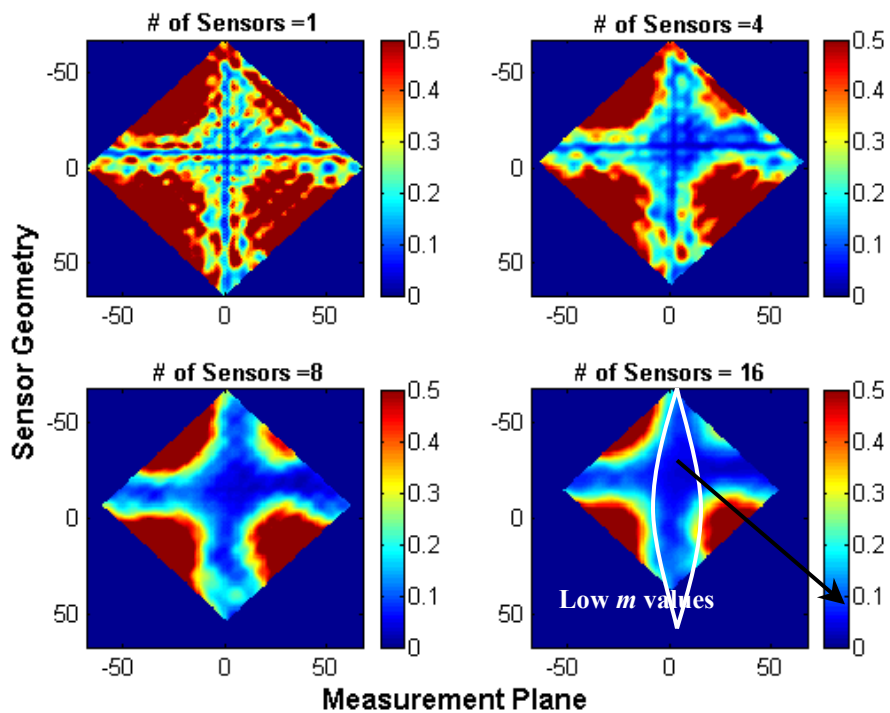


Figure 5.3.2  $m$  plots for different numbers of elements in the sensor array for target VAL-69.

The  $m$  plots have also been generated for sensor arrays with 1, 4, 8 and 16 sensors and are shown in Figure 5.3.2. The  $m$  plots show that a measurement plane with very low symmetry measures exists for almost all sensor geometries, indicating

that the subsurface target is a mine as shown in the  $m$  plot for the sensor array with 16 elements.

Thus the sum plots obtained from sensor array processing can be used to decide whether the target is present or not with a high level of confidence. It has also been observed that the higher the number of sensors in the sensor array, the better is the subsurface target detection.

Using the  $m$  and sum matrices generated by sensor array processing, we see that cascade plots are an interesting representation of the results.

### **5.3.1 Cascade Plots**

A plot in which the  $m$  values for each sensor geometry are plotted for all measurement planes is called a *cascade plot* for the  $m$  values. A similar cascade plot can be generated for sum values. If the subsurface target is symmetric, a unique measurement plane exists for which the cascade plot of the sum values for some sensor geometries peaks to its maximum and the cascade plot of the  $m$  values for almost all the sensor geometries dips to a very low value (appearing as a null in the cascade plot of the  $m$  value matrix). For an asymmetric or clutter target the sum value cascade plot should show a peak indicating high sum values about a measurement plane. This confirms the presence of the subsurface target. But as the target is asymmetric there will be no null in the  $m$  value cascade plot.

All the cascade plots in this section have been generated using the  $m$  value and sum value matrices obtained using a sensor array with eight elements. This section also serves as a summary of all the results obtained from the experiments in

sandbox and at Ft. A.P. Hill, Virginia. For each target, the color coded sum and  $m$  plots (using sum and  $m$  value matrices generated with an array of eight sensor elements) along with the sum and  $m$  cascade plots will be presented and briefly discussed. The targets for which the results will be presented in this section are the Styrofoam disc, rock, crushed milk jug, anti-personnel mines (PMA-3, VAL-69, M-14), TM-46, and irregular wood.

# 1.Styrofoam Disc

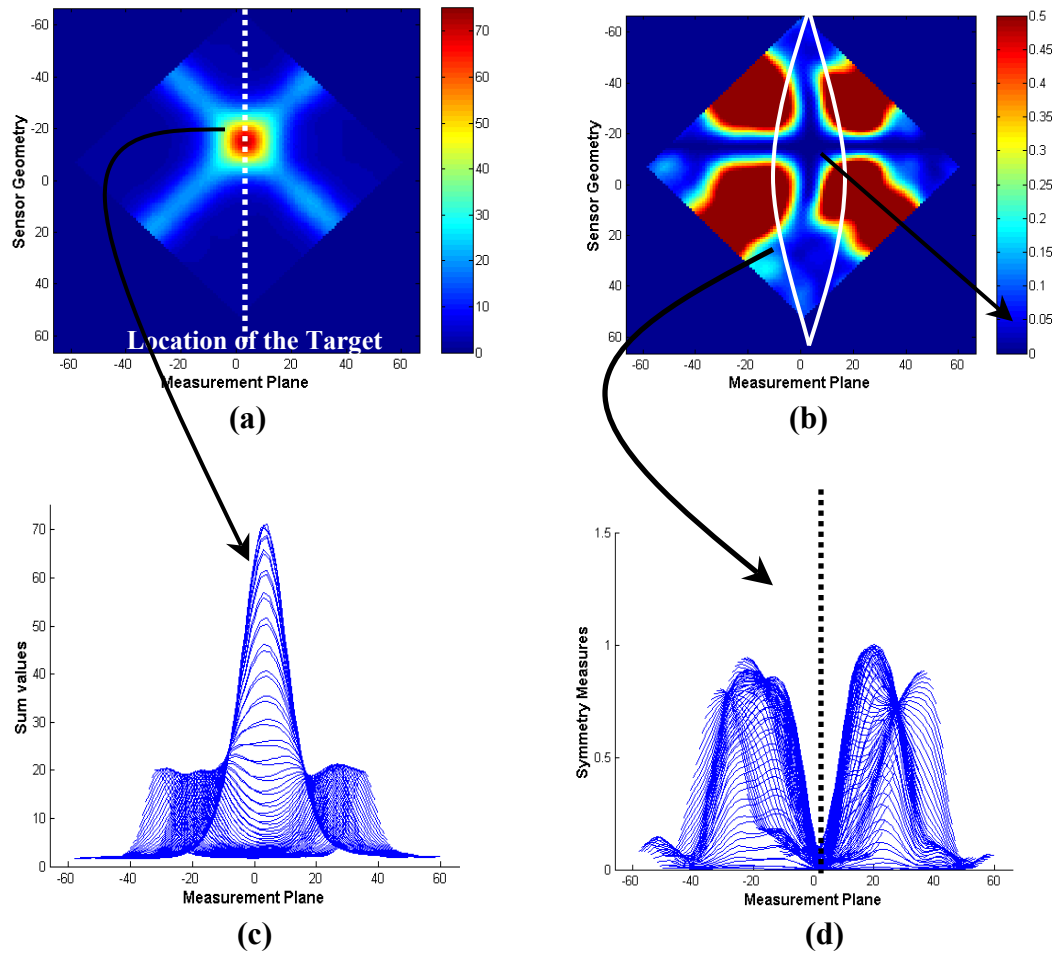


Figure 5.3.1.1(a): Sum plot for the Styrofoam disc using a sensor array with eight elements. Presence of high sum values indicated by dark red and high value pixels. (b)  $m$  plot for Styrofoam disc. Very low symmetry measures seen around measurement plane in region-5 to 5. (c) Cascade plot for sum value matrix. Presence of subsurface target confirmed by huge peak in cascade plot for sum values. (d) Cascade plot for  $m$  value matrix. The target is symmetric as cascade plot for  $m$  values indicates a deep null in the plane shown in the figure.

Figure 5.3.1.1 summarizes the results for the experiment on the Styrofoam disc. The results shown have been processed using a sensor array with eight elements in it.

The presence of high sum values in both the sum plot and the cascade plot (for the sum value matrix) indicates the presence of a subsurface target. The  $m$  plot and cascade plot (for the  $m$  value matrix) exhibit low symmetry measures for almost all sensor geometries for a measurement plane in the vicinity of the approximate location of the subsurface target. Therefore, all the results in Figure 5.3.1.1 suggest that the subsurface target is symmetric!

## 2. Rock

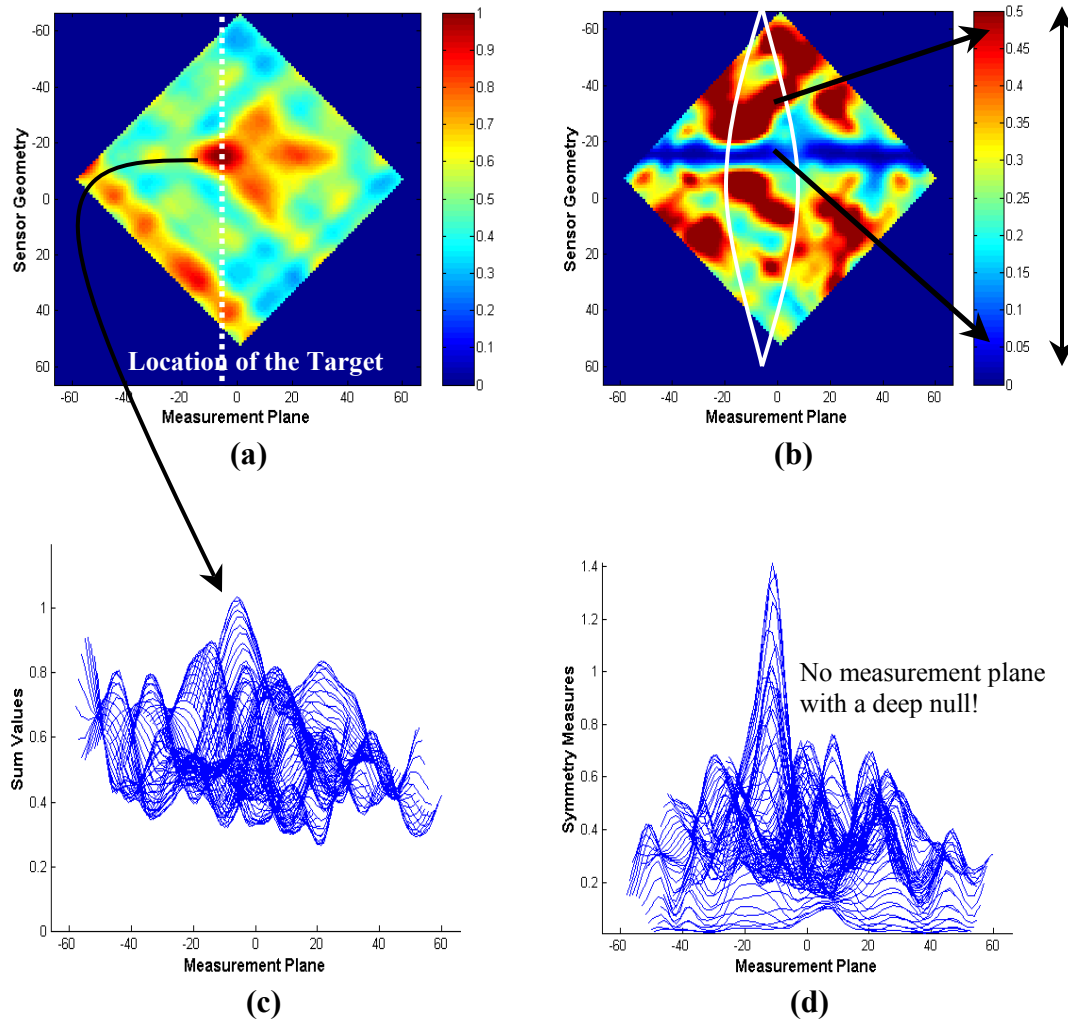


Figure 5.3.1.2(a): Sum plot for the rock using a sensor array with eight elements. Presence of high sum values indicated by dark red and high value pixels. (b)  $m$  plot for rock. Absence of measurement plane with low symmetry measures for almost all sensor geometries indicates subsurface target is asymmetric. (c) Cascade plot for sum value matrix. Presence of subsurface target confirmed by huge peak in cascade plot for sum values (d) Cascade plot for  $m$  value matrix. The null, which was present for the symmetric target, is missing. Therefore subsurface target is asymmetric.

From the sum plots and cascade plot for the sum value matrix in the Figure 5.3.1.2, the presence of a subsurface target can be established. The target can be classified as asymmetric and hence clutter, as the  $m$  plot and cascade plot for  $m$  value

matrix do not indicate a measurement plane in close proximity to the location of target for which the  $m$  values have a low magnitude. The subsurface target (i.e., rock) has been detected and classified as asymmetric using the measurements collected.

### 3. Crushed Milk Jug

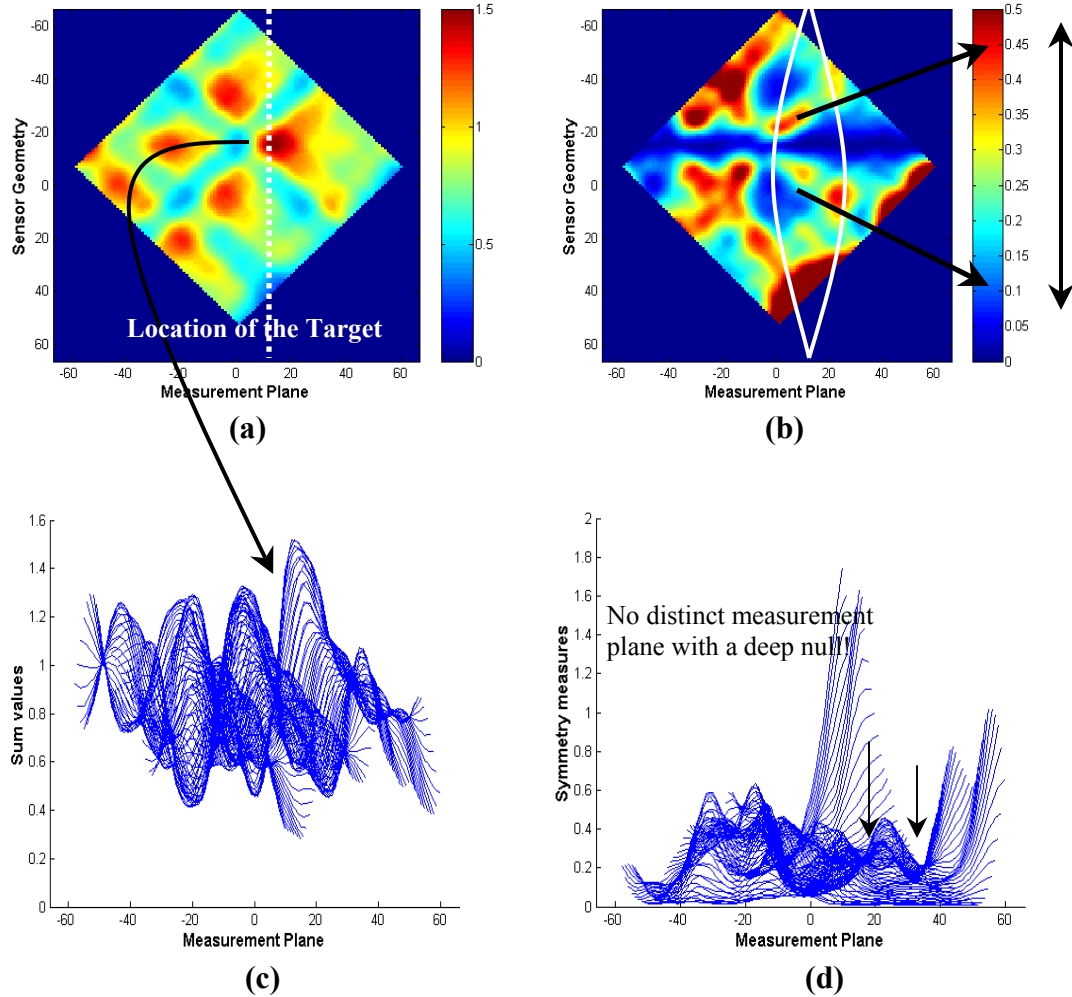


Figure 5.3.1.3(a): Sum plot for the crushed milk jug using a sensor array with eight elements. Presence of high sum values indicated by dark red and high value pixels. (b)  $m$  plot for crushed milk jug showing absence of distinct measurement plane with low symmetry measures for almost all sensor geometries. (c) Cascade plot for sum value matrix. Presence of subsurface target confirmed by huge peak in the cascade plot for sum values. (d) Cascade plot for  $m$  value matrix. Some nulls can be seen in cascade plot (shown by arrows in (d)), but they are not deep and also null does not exist for all sensor geometries.

The presence of a subsurface target is detected as the sum plot and cascade plot for sum matrix indicate high values. For target classification, it can be seen from

the  $m$  plot that there are some measurement planes for which some sensor geometries have low symmetry measures (indicated by arrows in Figure 5.3.1.3(d)). But there is no distinct measurement plane for which the  $m$  values have a low magnitude for almost all the sensor geometries. Therefore, the subsurface target can be classified as asymmetric and hence is clutter.

#### 4. PMA-3, An Anti-personnel Mine

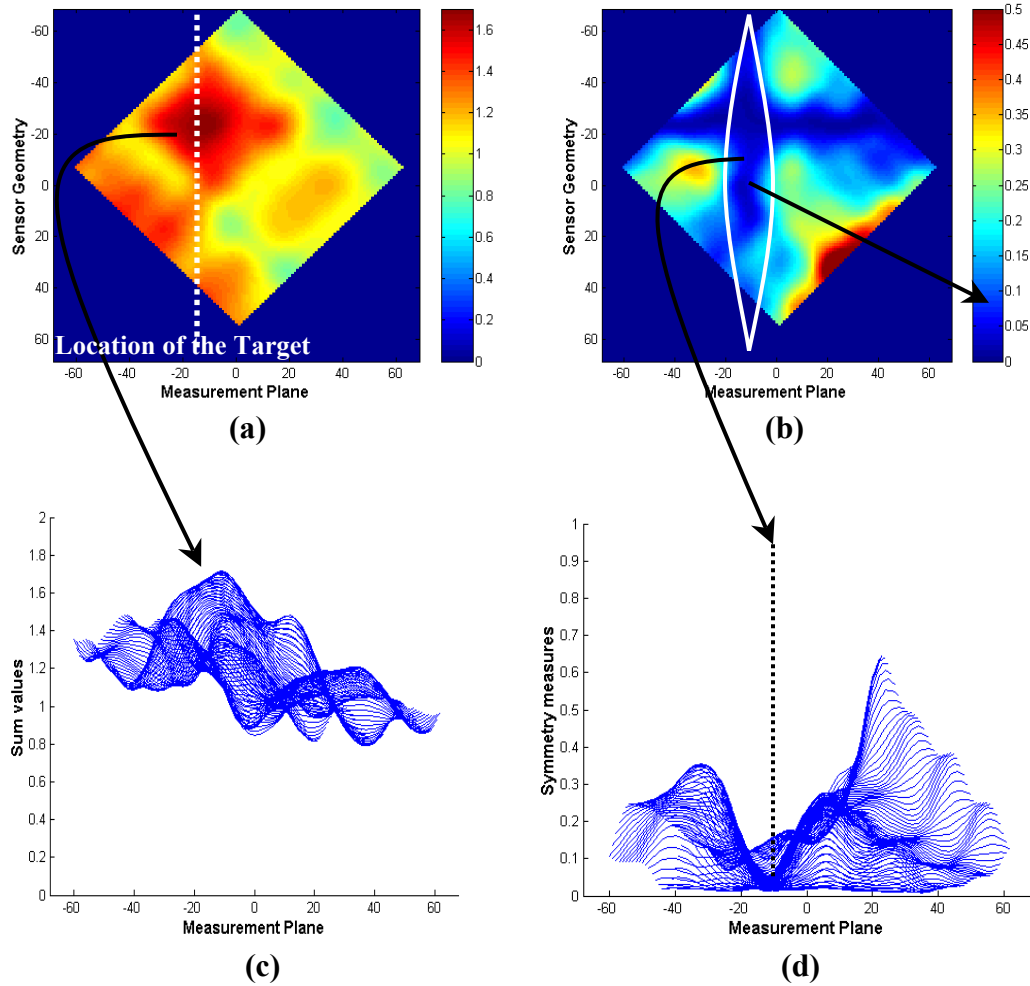


Figure 5.3.1.4 (a): Sum plot for PMA-3 using a sensor array with eight elements. Presence of high sum values indicated by dark red pixels and location of target indicated by white dotted line. (b)  $m$  plot for PMA-3. Very low symmetry measures in  $m$  plot indicated on the plot, classifying the target as symmetric object. (c) Cascade plot for sum value matrix for PMA-3. The cascade plot shows peak indicating presence of subsurface target. (d) Cascade plot for  $m$  value matrix shows deep null in the measurement plane.

The target PMA-3 is an anti-personnel mine on which data were collected during the field test at Ft. A.P. Hill test site in Virginia in August 2001. The mine has very little metal content and hence metal detectors might miss the target.

From the sum plots and the cascade plot for the sum value matrix, the presence of a subsurface target can be established based on the high intensity red pixels in the sum plot and the peak in the cascade plot in Figure 5.3.1.4(c). What remains is target classification. The subsurface target can be declared a mine with a high level of confidence, as the  $m$  plot has measurement planes that have low symmetry measures for almost all sensor geometries. Also the cascade plot in (d) has a null for the measurement plane indicated.

## 5. VAL-69, Anti-personnel Mine

VAL-69 is an anti-personnel mine on which data were collected during the field test in August 2001.

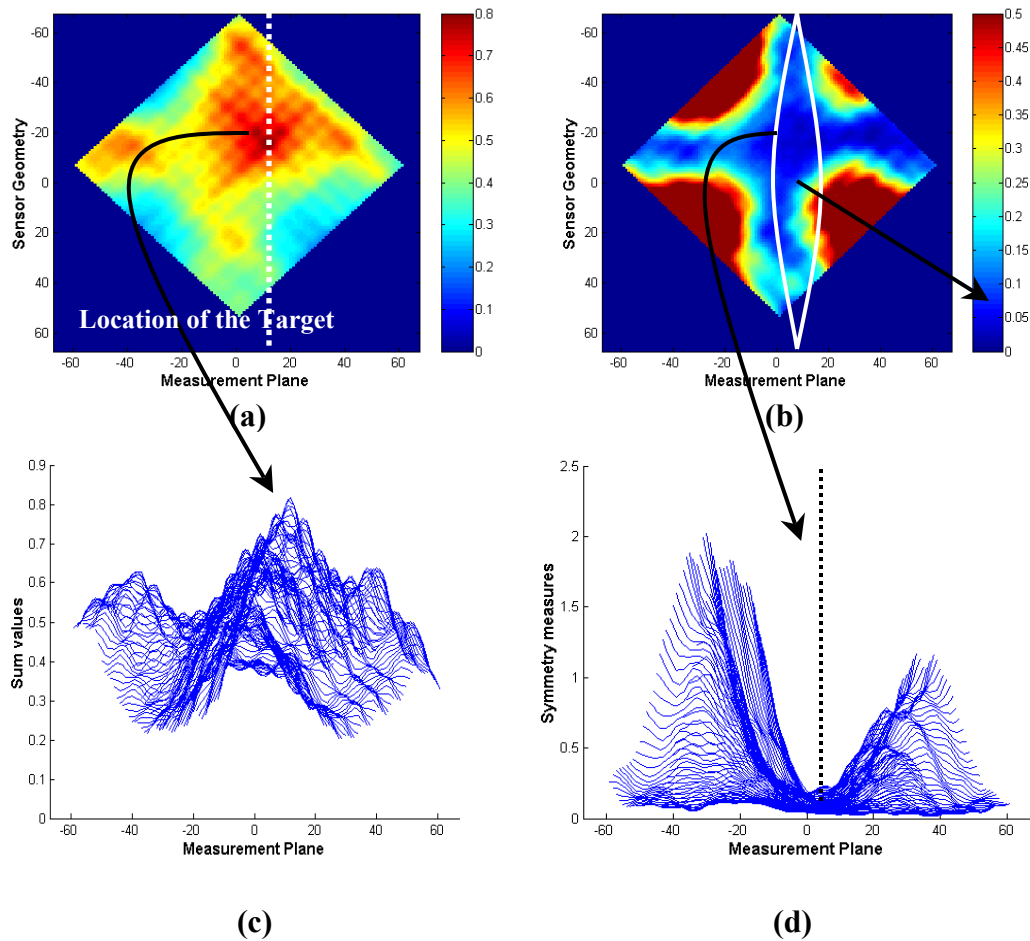


Figure 5.3.1.5 (a): Sum plot for VAL-69 using a sensor array with eight elements. Presence of high sum values indicated by dark red pixels. Location of target indicated by white dotted line. (b)  $m$  plot for VAL-69. Very low symmetry measures in  $m$  plot indicated on plot, classifying the target as symmetric object. (c) Cascade plot for sum value matrix for VAL-69. The cascade plot shows peak indicating presence of subsurface target. (d) Cascade plot for  $m$  value matrix shows deep null in the measurement plane.

The presence of the subsurface target is detected with a significant level of confidence as shown in Figure 5.3.1.5. This is the target that was used in section 5.3 to explain that sensor array processing enhanced subsurface target detection. The

cascade plot for the sum value matrix indicates a peak and hence detects the presence of subsurface target. The  $m$  plot for the VAL-69 is shown in Figure 5.3.1.5(b). The  $m$  plot indicates measurement planes with low symmetry measures for almost all sensor geometries. The cascade plot for the  $m$  value matrix shows a deep null, indicating symmetry in the subsurface target. Therefore, we conclude the subsurface target is a mine.

## 6. M-14, Anti-personnel Mine

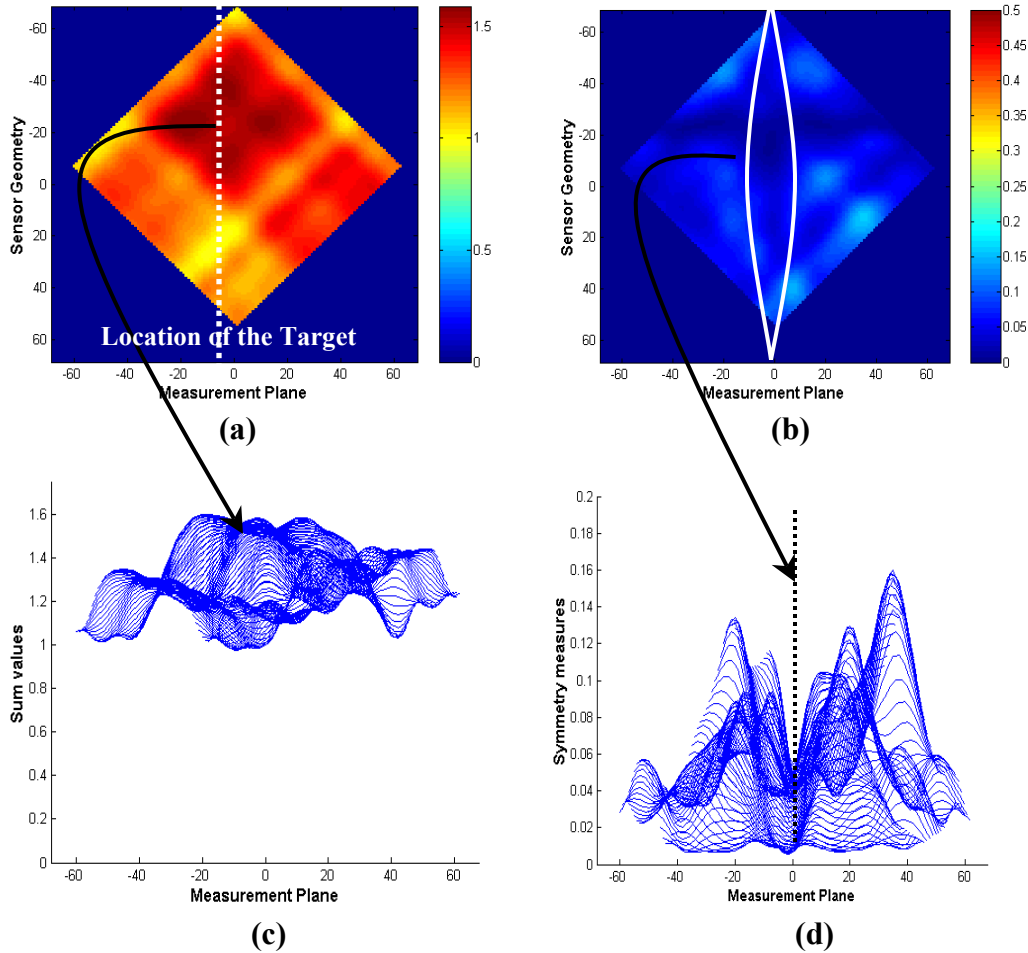


Figure 5.3.1.6 (a): Sum plot for M-14 using a sensor array with eight elements. Presence of high sum values indicated by dark red pixels. Location of target indicated by white dotted line. (b)  $m$  plot for M-14. The  $m$  plot is completely blue! Is the target symmetric? (c) Cascade plot for sum value matrix for M-14. The cascade plot shows peak indicating presence of subsurface target. (d) Cascade plot for  $m$  value matrix shows measurement plane with a null. The maximum  $m$  value for all measurements on this target is less than 0.2, which is quite low.

M-14 is an anti-personnel mine for which data were collected during the field experiment.

The sum plot and cascade plot for the sum value matrix indicate the presence of a subsurface target detection as the sum values are high. In fact the sum plot is filled with high intensity red pixels! The  $m$  plot is completely blue with no specific indication of a measurement plane that has low  $m$  values for almost all the sensor geometries. From the cascade plot for the M-14, a measurement plane exists with very low  $m$  values as indicated in Figure 5.3.1.6(d) when compared to other measurement planes. Though the target can be detected and classified as symmetric, the question remains as to why the  $m$  plot is totally blue!

The reason why the  $m$  plot could be completely blue, indicating a very low magnitude of  $m$  coefficients, is the sum plot is filled with high intensity red pixels (indicating the sum values are high). The denominator of the equation that is used to compute the symmetry measures is the sum values. Therefore, since all sum values are high, all  $m$  values turn out to have low magnitude, and this reflected as blue values in the  $m$  plot! One of the reasons for the sum values to have relatively high magnitude is that gating (or truncation) the radar responses does not mitigate the effects of surface clutter on the estimates of the scattering from the subsurface target. Is there any other method to reduce the effects of surface clutter?

## 7. Irregular Wood

Irregular wood is one of the clutter targets from the field experiments at Ft. A.P. Hill, Virginia.

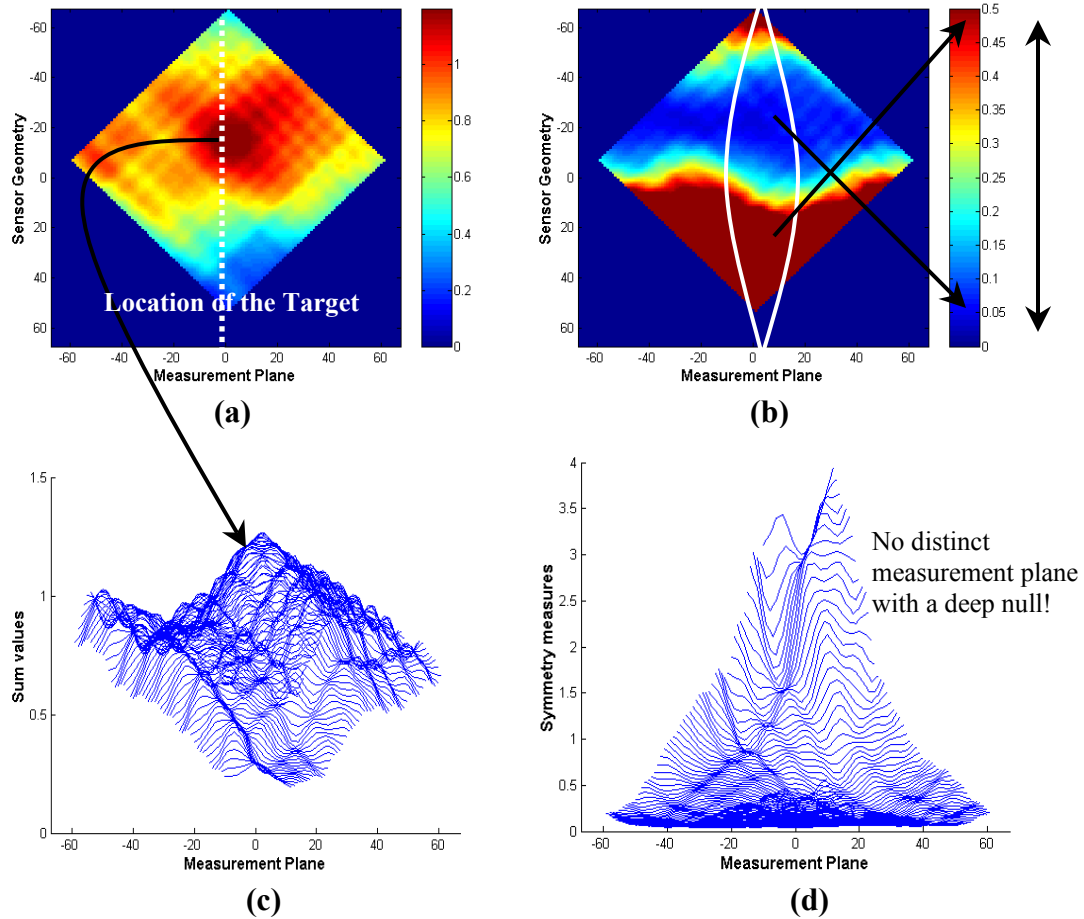


Figure 5.3.1.7 (a): Sum plot for irregular wood using a sensor array with eight elements. Presence of high sum values indicated by dark red pixels. Location of target indicated by white dotted line. (b)  $m$  plot for irregular wood. There is no distinct measurement plane for which almost all  $m$  values are low. (c) Cascade plot for sum value matrix for irregular wood. The cascade plot shows peak indicating presence of subsurface target. (d) Cascade plot for  $m$  value matrix shows no measurement plane with low  $m$  values for many sensor geometries.

The irregular wood could be detected as shown in the sum plot, Figure 5.3.1.7(a), and the cascade plot for the sum value matrix, Figure 5.3.1.7(c). From the

$m$  value plot, Figure 5.3.1.7(b), it can be inferred that the subsurface target is clutter, as no measurement plane exists with low symmetry measures for almost all sensor geometries. Thus, the subsurface target is detected and classified as clutter!

The results from various experiments show that GPR can be used for extracting the level of symmetry in the subsurface targets and hence can classify subsurface targets as symmetric (landmines) or asymmetric (clutter) objects. Chapter 4 investigated the possibility of deploying the detection scheme in the minefield by proposing a hand-held model. The basics of the hand-held model and different issues involved in developing an efficient landmine detection tool were described in Chapter 4. The simple data collection scheme proposed in Chapter 4, which can be used to synthesize multiple sensor geometry hand-held detector, was validated and tested by different experiments in the sandpit and during the field trip. Using the results, we found we could decide with a fairly high degree of confidence whether the subsurface target is a mine or clutter. To resolve the uncertainty in detecting the presence of some targets, processing with a sensor array has been proposed as a potential solution. Results from sensor array processing reveals that more sensors in the array provide better subsurface target detection. Thus, the experiments have proved that the ground penetrating radar can be used in hand-held detectors to detect and classify subsurface targets as mines or clutter based on the concept of symmetry. Were the results obtained on all the targets conclusive with regard to target detection and classification? An interesting result is detailed next.

TM-46 was a target on which the data collected during the field experiment were processed with a sensor array of eight elements. We need to decide whether it is mine or clutter based on the results that are shown in Figure 5.3.1.8.

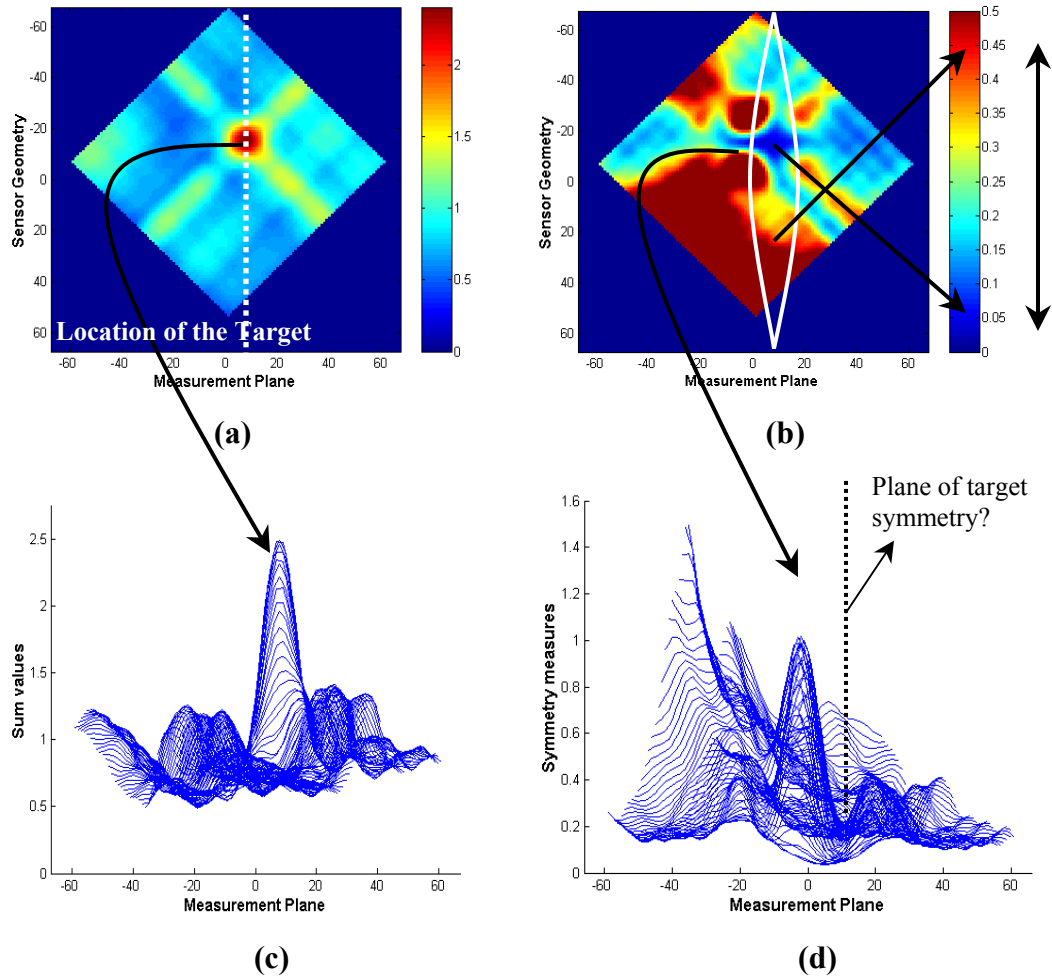


Figure 5.3.1.8 (a): Sum plot for TM-46 using a sensor array with eight elements. Presence of high sum values indicated by dark red pixels. Location of target indicated by white dotted line. (b)  $m$  plot for TM-46. Measurement planes are shown in which  $m$  values range from low to high. (c) Cascade plot for sum value matrix for TM-46. The cascade plot shows peak indicating presence of subsurface target. (d) Cascade plot for  $m$  value matrix does not show deep null.

The sum plot and the cascade plot for the sum value matrix indicate the presence of high sum values and therefore the presence of subsurface target could be

easily detected. The  $m$  plot and cascade plot for the  $m$  value matrix indicate a measurement plane in the proximity of target location, which has low  $m$  values for some sensor geometries and high  $m$  coefficients for other sensor geometries. The results suggest that the subsurface target could be detected and also be classified as a clutter object because the  $m$  values were ranging from low to high. Therefore, we could decide the subsurface target is clutter. NO! The target TM-46 is an anti-tank mine from the field experiment. Without *a priori* information of whether the target was a mine or natural clutter, the decision based on the results in Figure 5.3.1.8 would lead to a missed detection. Could there be a bias introduced in calculating the symmetry measures?

The bias in the symmetry measures can be due to either positioning errors while performing the scans to collect the data or due to improper gating of the radar responses (as explained in Section 2.3). If the data collection system were inaccurate, then bias in symmetry measures would have been reflected in all the  $m$  plots for symmetric targets. Since the results for the other symmetric targets are good, we conclude that the data collection system is accurate. Is the gating of the radar response inducing the error in symmetry measures? Gating the radar responses obtained after matched-filter processing will lead to accurate symmetry measures only if the matched filter minimizes the effects of interference (i.e., direct coupling, noise and, more important, the dominant ground response) on the scattering from the subsurface target. Is the matched filter an optimum signal processor for the application of subsurface target detection?

## 5.4 Matched Filter for Subsurface Target Detection

A matched filter is the conventional signal-processing algorithm in the field of radar signal processing. The matched filter has the feature of maximizing the signal-to-noise ratio. In this section, simulations will be performed to analyze the performance of the matched filter for the application of subsurface target detection.

For the simulations, radar data were simulated and assumed to have scattering only from the ground and the subsurface target. The ground is at a delay of 2.2 ns with a scattering of 30 dB, and the subsurface target is assumed to be at a delay of 6.5 ns with a scattering of 5 dB. Matched-filter processing was performed to obtain the scattering as a function of time and is shown in Figure 5.4.1.

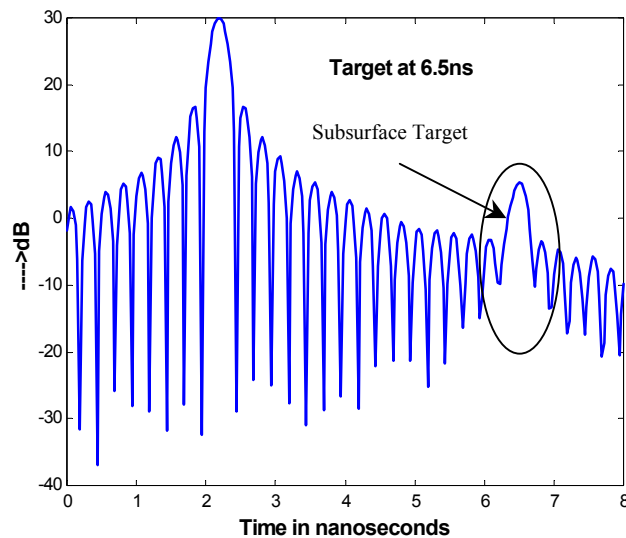


**Figure 5.4.1: Scattering as a function of time generated using matched filter. The ground is at a delay of 2.2 ns and the subsurface target is at a delay of 6.5 ns.**

It can be seen from Figure 5.4.1 that the subsurface target could be easily detected at a delay of 6.5 ns with accurate estimates of scattering. The matched filter

is giving good results with regard to subsurface target detection. Can't we use the matched filter for the problem at hand?

For the application of landmine detection and in general detection of shallow subsurface targets, the targets are at a differential delay of less than 1 ns from the delay of the ground response. This is the scenario for which the matched filter has to work.

Therefore, the position of the subsurface target in the simulated radar data was moved to 2.75 ns with a scattering of 5 dB. Matched-filter processing was performed and the scattering as a function of delay is shown in Figure 5.4.2.

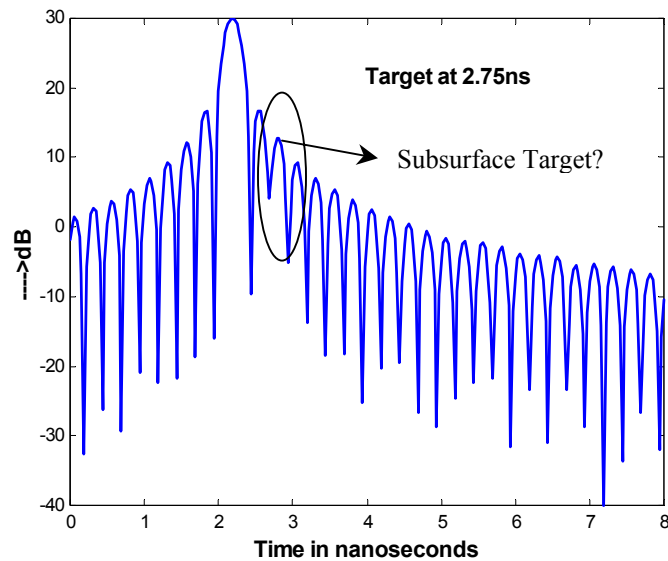


**Figure 5.4.2: Scattering as a function of time generated using matched filter. The ground is at a delay of 2.2 ns and the subsurface target is at a delay of 2.75 ns. The time-domain side lobes of the dominant scatterer mask the subsurface target.**

It can be seen from Figure 5.4.2 that the matched filter is not able to detect the presence of a subsurface target at a delay of 2.75 ns. This is because the time-domain side lobes of the dominant scatterer (i.e., ground response) mask the weak scattering

from the subsurface target. Moreover, the scattering estimate at a delay of 2.75 ns has an error of close to 5 dB. Even if the time gate is applied, this will not serve the purpose of mitigating the effects of interference. This is because the scattering estimate errors due to clutter have already been induced as the signal-processing algorithm used was not optimum.

The matched filter maximizes the signal-to-noise ratio, but does not consider the effects of clutter. In the application of landmine detection, scattering from the ground is considered clutter. Clutter dominates the interference for the problem of detecting shallow subsurface targets. Hence, the optimum signal processor is the one that minimizes the adverse effects of clutter, or in other words maximizes the Signal-to-Interference Ratio (SIR) and not just SNR. Can a robust signal processor that maximizes SIR be developed?

## Chapter 6

### Minimum Mean-Squared Error GPR Processor

The challenge in detecting shallow subsurface targets is to mitigate the effects of dominant ground response on weak subsurface scattering. The time-domain side lobes due to the dominant scatterer might mask the weak scattering from the subsurface target. The signal-processing algorithm that was used for processing our data was a conventional matched filter. It has been shown in Section 5.4 that the matched filter is not an efficient signal-processing algorithm for the application of landmine detection and, in general, detecting the presence of shallow subsurface targets. Can we develop a better signal-processing algorithm that can perform better than the matched filter with regard to subsurface target detection? What is the basis for investigating the development of a robust signal-processing algorithm?

In this chapter, a robust signal-processing algorithm with a performance superior to that of the matched filter with regard to subsurface target detection will be developed. The signal-processing algorithm proposed will be optimum in the mean-squared error sense. The estimate errors in the scattering coefficients as a function of depth (or delay) will be minimized using the Minimum Mean-Squared Error (MMSE) criterion. This chapter will detail the need for a different signal-processing algorithm than a matched filter, develop a minimum mean-squared error GPR processor and evaluate its performance using simulations in MATLAB. The processor we

developed will then be used to process the measured data and results will be explained.

## **6.1 Background and Motivation**

The conventional signal-processing algorithm in the field of radar is the matched filter. The feature of the matched filter is to maximize the signal-to-noise ratio but it does not specifically try to minimize the effects of clutter. In the case of landmine detection, the clutter is the ground (specular) response and the energy associated with it is high compared to that of the subsurface target. Therefore, if the adverse effects of the clutter are not minimized, the result can be large estimate errors. It has been shown in Section 5.4 that the matched filter is not able to minimize the estimate errors due to clutter and hence it is not an optimum signal processor for the problem of detecting weak subsurface targets. To minimize the estimate errors, the signal-to-interference ratio parameter must be maximized when the interference includes both clutter and noise.

Scattering as a function of time obtained using the matched filter has time-domain side lobes of the dominant scatterer, which mask the weak subsurface scatterer. The conventional method for suppressing the time-domain side lobes is the windowing technique. The time-domain side lobes due to the ground or specular response can be suppressed by applying a window to the frequency-domain data and then performing matched-filter processing. But this technique will not provide a complete solution to the problem of detecting shallow subsurface targets. Using

windowing functions to reduce the side lobe level has the down side of degrading the resolution (or broadening the main lobe). If the subsurface target is buried at a very shallow depth beneath the ground surface, the main lobe itself can mask the scattering from the subsurface target. To illustrate that windowing is not an efficient solution, a simulation was performed with simulated radar data. The ground was assumed to be at a delay of 2.2 ns with a scattering of 30 dB and the subsurface target was at a delay of 2.75 ns with a scattering of 5 dB. This is the same simulated radar data that was used to prove that the matched filter was inefficient in Section 5.4. The option of windowing was investigated for this simulation with Hamming and Blackman windows. The result of the simulation is shown in Figure 6.1.1.

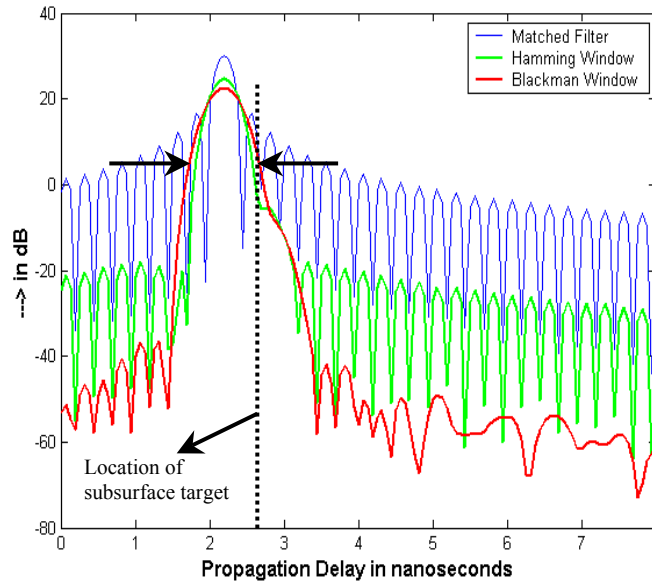


**Figure 6.1.1: Simulation results with Hamming and Blackman windows to reduce the time-domain side lobe problem. The main lobe widens and masks the subsurface target.**

It can be inferred from Figure 6.1.1 that there is a reduction in side lobe level, but the degradation of resolution (broadening of main lobe) is showing its adverse

effects. The subsurface target is very close to the ground, and the main lobe itself masks the weak subsurface scatterer.

Therefore the option of windowing the frequency-domain data, followed by a matched-filter processing though suppresses the time-domain side lobes, degrades the resolution. With landmine or clutter buried a few centimeters below the surface of the ground, resolution cannot be sacrificed. What is the solution to the problem? Is there a robust signal processor that mitigates the effects of surface scattering on the weak subsurface scattering? If so, how do we develop a signal processor with performance superior to the matched filter with regard to subsurface target detection? As a solution to this problem, a signal-processing algorithm that minimizes the error in the scattering estimates using the MMSE criterion has been proposed.

In the development of the MMSE GPR processor, the *a priori* knowledge about the radar measurements and the scattering as a function of delay plays a very important role. Regarding scattering, we know that the response from the subsurface target follows the response from the ground in time and also that the ground response is far higher in magnitude than the weak scattering from the target beneath the ground. This *a priori* information will be used in developing an estimator, which is intended to perform better than the matched filter [10].

To derive an expression for the estimator, the first step is to develop an appropriate model for the radar response.

## 6.2 Radar Response Model

The targets illuminated by the ground penetrating radar can be considered different layers separated by the time resolution. The time resolution  $\Delta\tau$  is defined by the bandwidth of operation of the radar ( $\Delta\tau = \frac{1}{2B}$ ). The scenario is shown in Figure 6.2.1. The delay corresponding to the maximum unambiguous range is denoted by  $\Delta\tau_{\max}$ . Therefore the total number of targets illuminated by the radar is given by  $\Delta\tau_{\max}/\Delta\tau$ .

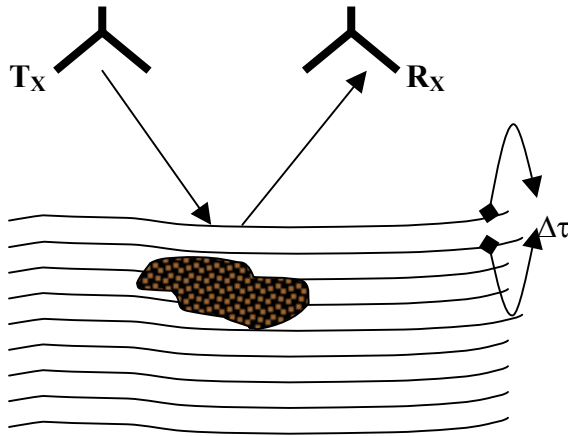


**Figure 6.2.1:** The targets illuminated by the radar are considered as different layers separated by  $\Delta\tau$ , the time resolution.  $T_x$ - $R_x$  is the bistatic radar measurement.

Each illuminated target has a scattering coefficient associated with it, which is a function of delay, that is,  $\gamma(\tau)$ . Each of the layers (or targets), also called range bins, can be considered a linear time invariant system. Each of the range bins has an impulse response  $h(\tau)$ , a function of delay, which means each range bin has a

different impulse response. If  $s(t)$  is the signal transmitted, then the response from a range bin at a delay  $\tau_1$  is the convolution of the impulse response  $h(\tau_1)$  with the transmitted signal  $s(t)$ . The convolution sum has to be weighted with the scattering coefficient of the target at the delay  $\tau_1$ . The composite radar response can be modeled as the superposition of responses from all the range bins (or layers). The composite radar response can be expressed as follows [11]

$$\mathbf{r}(\mathbf{t}) = \iint \gamma(\tau) \mathbf{h}(\tau; \mathbf{t} - \mathbf{t}') \mathbf{s}(\mathbf{t}') d\mathbf{t}' d\tau + \mathbf{n}(\mathbf{t}) \quad (6.2.1)$$

Equation (6.2.1) is a mathematical representation of adding all the responses from individual range bins;  $\gamma$  is the complex scattering coefficient and is a function of the delay and  $\mathbf{n}(\mathbf{t})$  is the noise associated with the radar measurement. Equation (6.2.1) can be rewritten as (6.2.2)

$$\mathbf{r}(\mathbf{t}) = \gamma(\tau) \boldsymbol{\rho}(\tau; \mathbf{t}) + \mathbf{n}(\mathbf{t}) \quad (6.2.2)$$

where  $\boldsymbol{\rho}(\tau; \mathbf{t})$  is the normalized response of the target at a delay  $\tau$ . In the rest of the thesis, the following notations are used for equations involving linear algebra: small letters with regular style are used to represent constants, bold-faced lowercase letters indicate vectors, and bold-faced uppercase notations are used for matrices. Using linear algebra, the (6.2.2) can be written as

$$\mathbf{r} = \sum_j \gamma_j \boldsymbol{\rho}_j + \mathbf{n} \quad (6.2.3)$$

where  $j$  includes all the illuminated targets, which are separated by time resolution  $\Delta\tau$ .

If we consider that the radar measurements have been collected as a function of frequency, the normalized response matrix is a matrix in which each column is the normalized response as a function of frequency for a different delay. The complex scattering is a column vector with each entry being the scattering coefficient corresponding to a different delay. This will reduce (6.2.3) to

$$\mathbf{r} = \mathbf{P}\boldsymbol{\gamma} + \mathbf{n} \quad (6.2.4)$$

where  $\mathbf{P}=[\boldsymbol{\rho}_1, \boldsymbol{\rho}_2, \boldsymbol{\rho}_3, \dots, \boldsymbol{\rho}_{\tau_{\max}}]$  is the normalized response matrix,  $\boldsymbol{\gamma}=[\gamma_1, \gamma_2, \gamma_3, \dots, \gamma_{\tau_{\max}}]^T$  is a vector of scattering coefficients (which is a function of delay), and  $\mathbf{n}$  is the noise.

Thus, (6.2.4) compactly models the radar response model. This model will be used to develop an estimator that will minimize the mean-squared error of the estimate of the scattering coefficients.

### 6.3 MMSE Estimator

Using the radar response model developed in Section 6.2, an estimator has been developed that minimizes the mean-square error in the estimate of the scattering vector  $\boldsymbol{\gamma}$ . Let the estimator that satisfies the criterion of minimizing the mean-squared error be denoted as  $\mathbf{W}_{\text{EST}}$ . The estimator or the Minimum Mean-Squared Error (MMSE) filter  $\mathbf{W}_{\text{EST}}$  is a matrix with weight vectors as a function of frequency for each of the delays. The radar data are multiplied with this weight matrix to produce the estimate of the scattering coefficients ( $\hat{\boldsymbol{\gamma}}$ ). The scattering estimate can be expressed as

$$\hat{\boldsymbol{\gamma}} = \mathbf{W}_{\text{EST}} \mathbf{r} \quad (6.3.1)$$

where  $\hat{\gamma}$  is the estimate of scattering from different targets and  $\mathbf{r}$  is the radar data.

The estimate error is defined as the difference between the actual scattering and the estimated scattering given in (6.3.1). The estimate error can be expressed as

$$\boldsymbol{\varepsilon} = \boldsymbol{\gamma} - \hat{\boldsymbol{\gamma}} \quad (6.3.2)$$

Using the principle of orthogonality, which states that the error vector is orthogonal to the data, an expression for the estimator can be derived. The orthogonality principle can be mathematically represented as follows [11]

$$\mathbf{E}\{\boldsymbol{\varepsilon}\mathbf{r}'\} = \mathbf{E}\{(\boldsymbol{\gamma} - \mathbf{W}_{\text{EST}}\mathbf{r})\mathbf{r}'\} = \mathbf{E}\{\boldsymbol{\gamma}\mathbf{r}'\} - \mathbf{W}_{\text{EST}}\mathbf{E}\{\mathbf{r}\mathbf{r}'\} = \mathbf{0} \quad (6.3.3)$$

Consider the term  $\mathbf{E}\{\boldsymbol{\gamma}\mathbf{r}'\}$  in equation (6.3.3)

$$\begin{aligned} \mathbf{E}\{\boldsymbol{\gamma}\mathbf{r}'\} &= \mathbf{E}\{\boldsymbol{\gamma}(\mathbf{P}\boldsymbol{\gamma} + \mathbf{n})'\} = \mathbf{E}\{\boldsymbol{\gamma}\boldsymbol{\gamma}'\}\mathbf{P}' + \mathbf{E}\{\boldsymbol{\gamma}\mathbf{n}'\} \\ &= \mathbf{E}\{\boldsymbol{\gamma}\boldsymbol{\gamma}'\}\mathbf{P}' \end{aligned} \quad (6.3.4)$$

The second term in (6.3.4) vanishes because the noise and the scattering are independent, and the noise is assumed to be a zero-mean white Gaussian process.

Consider the term  $\mathbf{E}\{\mathbf{r}\mathbf{r}'\}$  in (6.3.3)

$$\begin{aligned} \mathbf{E}\{\mathbf{r}\mathbf{r}'\} &= \mathbf{E}\{(\mathbf{P}\boldsymbol{\gamma} + \mathbf{n})(\mathbf{P}\boldsymbol{\gamma} + \mathbf{n})'\} \\ &= \mathbf{E}\{\mathbf{P}\boldsymbol{\gamma}\boldsymbol{\gamma}'\mathbf{P}'\} + \mathbf{E}\{\mathbf{n}\mathbf{n}'\} \\ &= \mathbf{P}\mathbf{E}\{\boldsymbol{\gamma}\boldsymbol{\gamma}'\}\mathbf{P}' + \mathbf{E}\{\mathbf{n}\mathbf{n}'\} \\ &= \mathbf{P}\mathbf{K}_{\boldsymbol{\gamma}}\mathbf{P}' + \mathbf{K}_{\mathbf{n}} \end{aligned} \quad (6.3.5)$$

where  $\mathbf{K}_{\boldsymbol{\gamma}}$  is the correlation matrix representing the correlation between the scattering from different targets. This gives the coupling between the targets. The diagonal

elements of the target correlation matrix give the variance of the scattering (in other words, the energy scattered) from the illuminated targets. The diagonal elements of the matrix  $\mathbf{K}_\gamma$  can be divided into two regions, the ground response and the subsurface target region. Using an *a priori* knowledge of the scattering from the ground and subsurface target, the diagonal elements of the  $\mathbf{K}_\gamma$  matrix can be formed.  $\mathbf{K}_n$  is the noise covariance matrix, which is a diagonal matrix, and the diagonal elements are equal to the variance of noise.

Substituting (6.3.5) and (6.3.4) into (6.3.3) and solving for  $\mathbf{W}_{\text{EST}}$ , the estimator is given by (6.3.6)

$$\mathbf{W}_{\text{EST}} = \mathbf{K}_\gamma \mathbf{P}' [\mathbf{P} \mathbf{K}_\gamma \mathbf{P}' + \mathbf{K}_n]^{-1} \quad (6.3.6)$$

where the  $[\ ]^{-1}$  operator indicates the pseudo inverse of a matrix and  $[\ ]'$  indicates the conjugate transpose of the matrix. Equation (6.3.6) describes the estimator, which has to be used so that the mean-squared error in the estimates of scattering can be minimized. The matrix  $\mathbf{K}_\gamma$  is the *a priori* information provided to the MMSE estimator in (6.3.6), that was not provided when the matched filter was used. In the case of the matched filter, the weight matrix used is the conjugate transpose of the normalized expected response matrix ( $\mathbf{P}$ ).

Having developed a mathematical expression for the new processing algorithm, it has to be validated. Computer simulations should help in providing a good insight into the performance of the MMSE GPR processor and also in comparing its performance to that of the matched filter.

## 6.4 Simulation and Results

The MMSE GPR processor we developed will be validated in this section. Simulations in MATLAB were performed to validate the performance of the MMSE GPR processor and also to compare its performance to that of the matched filter. The simulation model must first be set up. Different parameters for the simulations need to be defined, such as the radar bandwidth, number of frequency points, and so forth.

### 6.4.1 Simulation Model

To develop a simulation model, defining the parameters to be used in the simulations is essential. The parameters chosen for the simulations were:

**Table 6.4.1.1 Radar Parameters for Simulation**

Radar Parameters	Values chosen for simulation
Bandwidth of operation	2 GHz-6 GHz
Number of Frequency points	201
Delay after Which a Target is Not Expected	8 ns

The radar operates from 2 GHz – 6 GHz with a frequency step size that corresponds to 20 MHz. The frequency step size sets the unambiguous range of the radar. The delay of 8 ns corresponds to a distance of approximately 1.5 m. The problem that is being addressed is that of shallow subsurface target detection. Moreover, it is reasonable to assume that no landmines are buried at a depth greater than 1.5 m.

Simulation parameters such as bandwidth and number of frequency points were set equal to the specific values as indicated in Table 6.4.1.1 because these were the values that were used for conducting experiments in the sandpit and during the field trip.

In computer simulations the user simulates the radar data. It is an ideal case where only the scattering from the ground and the subsurface target are non zero. The scattering from all other targets is set equal to zero. This is an unreasonable assumption and such a data set has been used only to validate the algorithm. The simulated radar data are formed by extracting the columns in the normalized response matrix, which correspond to the delay of the ground and the subsurface target, and weighting them with the scattering from the ground and the subsurface target, respectively. The noise in the radar data has been modeled as a zero-mean white Gaussian random process. The variance of the noise is set to a low value for simulation purposes. Since the noise is considered as uncorrelated, the noise covariance matrix is diagonal.

Another important parameter to be modeled correctly is the target correlation matrix. The targets illuminated by the radar can be divided into two regions, namely the ground response region and the subsurface target region. The scattering from the ground region is expected to be larger than the scattering from the subsurface target region. The diagonal elements of the target correlation matrix are the variance of the scattering ( $E\{\gamma\gamma'\}$ ) that indicates the amount of energy scattered from each of the range bins. The target correlation matrix is changed according to the delay of the

target for which the scattering is estimated. Consider that the target correlation matrix for the purpose of estimating the scattering from a target at a delay  $\tau$  is being formed. First it should be seen whether the target is in the ground response region or the subsurface target region. Since this is a simulation, the user will have the exact information of the energy scattered from the ground and the subsurface target. But this information should not be used in the target correlation matrix. Therefore an estimate of the scattered energy from the delay  $\tau$ , is assumed to be equal to 5 dB larger than the actual value. The other range bins in the ground region and in the subsurface target region are assigned energy 5 dB less than the actual values.

Using the target correlation matrix for a delay  $\tau$ , an optimum weight vector for the delay  $\tau$  is obtained using the developed estimator. This weight vector is used for calculating the scattering estimate for that delay using the equation (6.3.1).

Thus, for each of the delays, the scattering estimates are obtained by changing the target correlation matrix accordingly and calculating the estimates using (6.3.1). After looping through all the delays up to the maximum delay at which the subsurface target can be expected, the scattering as a function of time is generated.

Using this simulation model, different simulations were performed to create a comparative study between the performance of the MMSE GPR processor and the matched filter.

## 6.4.2 Simulation Results

Simulations were performed in MATLAB to evaluate the performance of the MMSE GPR processor and compare its performance with that of the matched filter. The performance metric will be efficient detection of subsurface targets buried at shallow depths beneath the ground. Several simulations were performed, and in each case the results obtained from the MMSE GPR processor were compared with the performance of the matched filter. Simulations were also used to explain the reasons for the MMSE signal-processing algorithm's superior performance when compared to the matched filter.

A simulation was performed with the ground at 2.2 ns and the subsurface target at 3 ns. The variance of the scattering ( $E\{\gamma\gamma'\}$  or the energy scattered) from the ground is set as 30 dB and the variance of scattering from the subsurface target is set as 0 dB. The simulation was set up according to the explanation in Section 6.4.1 and the performance of the MMSE GPR processor was compared to that of the matched filter. Figure 6.4.2.1 compares the performance of the MMSE GPR processor (in blue) to that of the matched filter (indicated in red).

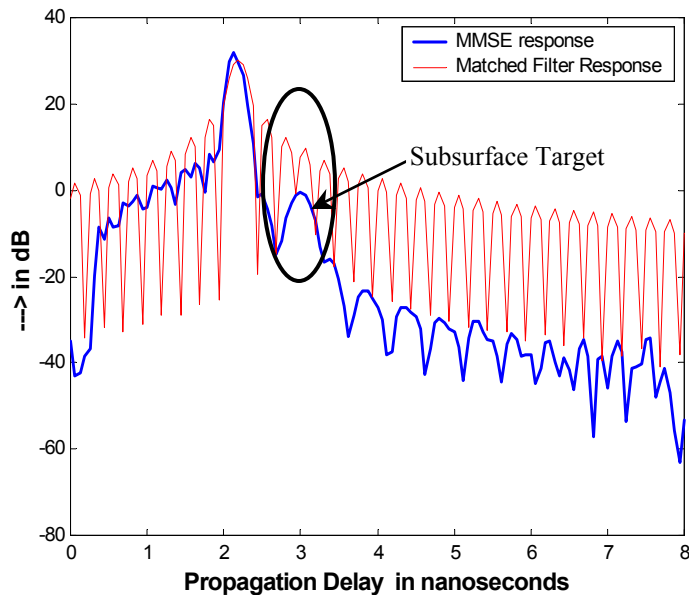


**Figure 6.4.2.1: Comparison of performance of MMSE GPR processor and matched filter on subsurface target buried at a depth that corresponds to a delay of 3 ns. The ground is at a delay of 2.2 ns.**

It can be inferred from Figure 6.4.2.1 that the MMSE GPR processor detects the target with good estimates of subsurface scattering. When matched filter was used, the time-domain side lobes of the dominant scatterer completely masked the subsurface target. Therefore, this simulation shows that the MMSE GPR processor performs better than the matched filter with regard to detecting the presence of a subsurface target.

Thus, with these simulations, the algorithm developed has been validated and we see that the MMSE GPR processor performs better than the matched filter. But can the question of why the MMSE GPR processor is exhibiting superior performance than the matched filter be answered using simulations?

An intuitive analysis as to why the MMSE signal-processing algorithm performs better than the matched filter can be obtained using simulations. If  $\mathbf{W}$  is the estimator, then the estimate of the scattering as a function of delay is obtained as given here

$$\hat{\boldsymbol{\gamma}} = \mathbf{W}\mathbf{r} \quad (6.4.2.1)$$

But it has already been shown that the radar response can be considered as a superposition of responses from targets at different delays and can be compactly represented by using (6.2.4). Using the compact radar data expression in 6.4.2.1 the estimate of the scattering can be written as

$$\begin{aligned} \hat{\boldsymbol{\gamma}} &= \mathbf{W}(\mathbf{P}\boldsymbol{\gamma} + \mathbf{n}) \\ &= \mathbf{W}\mathbf{P}\boldsymbol{\gamma} + \mathbf{W}\mathbf{n} \\ &= \mathbf{A}\boldsymbol{\gamma} + \mathbf{W}\mathbf{n} \end{aligned} \quad (6.4.2.2)$$

In 6.4.2.2,  $\mathbf{A}$  is a square matrix with dimension equal to the number of targets illuminated. The rows of the matrix  $\mathbf{A}$  are MMSE (weight vector) filter responses for the different targets illuminated, as a function of delay. As an ideal case the matrix  $\mathbf{A}$  should be a diagonal matrix so that there is no estimate errors when calculating the scattering from the different targets illuminated. Simulations were performed to study why the MMSE GPR processor was performing better than the matched filter.

A simulation was performed with the ground target at a delay of 2.2 ns and the subsurface target at a delay of 3.9 ns. The energy scattered from the ground is 30 dB and that from the subsurface target is -15 dB. The matrix  $\mathbf{A}$  for this simulation has

been computed and the MMSE filter response for the target at a delay of 3.9 ns is shown in Figure 6.4.2.2 (a) and compared with the performance of the matched filter.

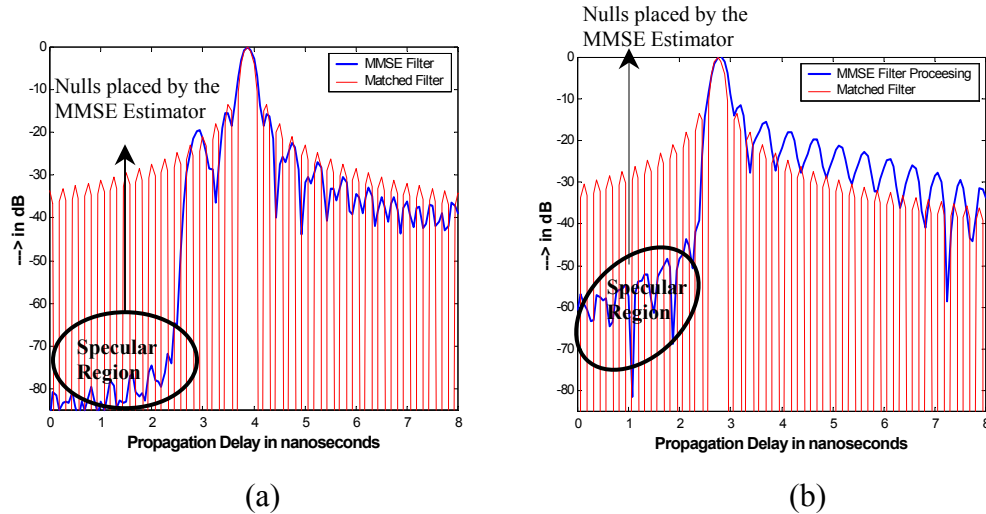


**Figure 6.4.2.2: Filter response for MMSE filter (in blue) and matched filter (in red). (a) For a target at a delay of 3.9 ns and (b) for a target at a delay of 2.75 ns.**

From Figure 6.4.2.2(a), it can be inferred that when calculating the scattering estimate of the subsurface target at 3.9 ns, the matched filter reduces the effects of the dominant scattering by 30dB, whereas the MMSE filter reduces the same by 75dB. The scattering from the ground in this simulation is 30dB and, even though the matched filter reduces the effects of the specular response by 30dB, it is not enough to avoid the estimate errors (when estimating the scattering from the subsurface target). On the other hand, the MMSE GPR processor avoids estimate errors due to the specular response while estimating scattering from the subsurface target by placing deep nulls in the specular region.

Another simulation was conducted with the subsurface target very close to the surface of the ground. The ground was assumed to be at a delay of 2.2 ns with a

scattering of 30 dB, and the subsurface target was at a delay of 2.75 ns with a scattering of 0 dB. Even when the target is close to the dominant scatterer, the MMSE filter is able to null out the adverse effects of the clutter, thereby providing a better signal-to-interference ratio than the matched filter, as shown in Figure 6.4.2.2(b). Therefore, the MMSE filter is able to reduce the effects of dominant surface scattering even when the target is very close to the dominant scatterer. Scattering as a function of propagation delay for the simulation with the ground at 2.2 ns and the subsurface target at 2.75 ns is shown in Figure 6.4.2.3. With the matched-filter processing (in red), the time-domain side lobes mask the response from the

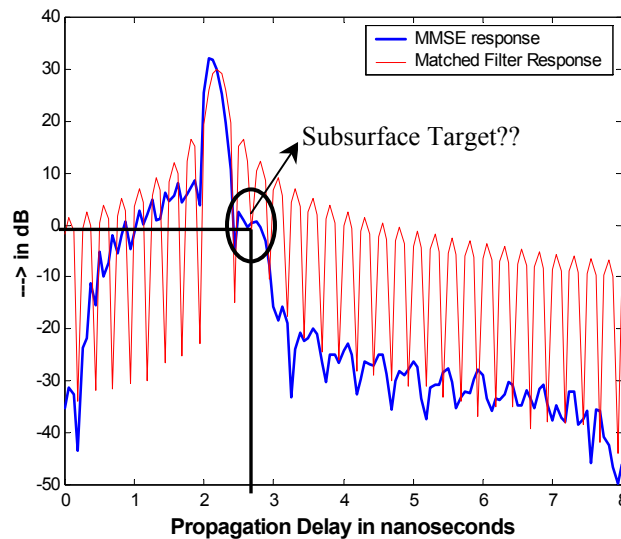


**Figure 6.4.2.3: Comparison of MMSE (in blue) and matched filter (in red) response when the subsurface target is at very shallow depths (2.75 ns).**

subsurface target. Even with the MMSE GPR processor, the subsurface target at a delay of 2.75 ns is not distinguishable from the ground response. The estimate of scattering from the subsurface target is approximately equal to 0 dB, which is actual value of the scattering used in this simulation. Therefore, though scattering estimates

were correct, the target is not distinctly visible in Figure 6.4.2.3. This problem of not being able to see the subsurface target distinctly persisted when the target was assumed to be buried at very shallow depths beneath the ground.

Thus, the simulations that were performed revealed that having *a priori* information about the scattering scenario could help develop a robust signal-processing algorithm that performs better than the matched filter with regard to subsurface target detection. In the simulations, scattering from targets other than ground and subsurface targets has been considered as zero, which is an unreasonable assumption. This assumption was made only to validate the algorithm using computer simulations. The MMSE algorithm must be tested on measured data.

## **6.5 Results on Measured Data**

The algorithm that was developed and validated for efficient subsurface target detection was used for processing measured data. The data, collected on the TM-46 anti-tank mine during the field experiment in Virginia, were processed using the MMSE GPR processor. This is the anti-tank mine which gave erroneous symmetry measures (shown in Figure 5.3.1.8(b, d)) and gave a direction to developing signal-processing algorithms that perform better than the matched filter.



**Figure 6.5.1: TM-46 anti-tank mine, a target from the field experiment in Ft. A.P. Hill, Virginia. Reproduced from [8].**

A picture of the TM-46 anti-tank mine, which was one of the mines used in the former Soviet Union, is shown in Figure 6.5.1, and its properties are given in Table 6.5.1. Data collection scans were performed in steps of 1 cm and the first point being the initial position of the board. The total number of data points collected is 68.

**Table 6.5.1 Physical Properties of TM-46. Reproduced from [8]**

Property	Typical Value for TM-46
Height	110mm
Diameter	304mm
Weight	8.4Kg
Casing	Steel casing
Sensitivity	120Kg Pressure

It would take a very long time to process all the data sets using the MMSE GPR processor. Therefore the data set to be processed was selected by using the sum

plot for the TM-46 (generated using the matched-filter processing). The sensor geometry and the measurement plane combination that produced maximum subsurface scattering was identified, and this bistatic measurement was processed using the MMSE GPR processor.

For processing this data file using the MMSE GPR processor, the diagonal elements of the target correlation matrix should be initialized. The estimates of the scattered energy (variance of the scattering  $E\{\gamma\gamma'\}$ ) in the ground response region and the subsurface target region were obtained from the matched-filter processing and are equal to  $-5$  dB and  $-15$  dB, respectively. The estimates of the scattered energy used for the target correlation matrix were 5 dB higher than the values obtained using the matched filter. Using these values, the MMSE signal-processing algorithm was used to process the TM-46 anti-tank mine data file.

Figure 6.5.2 shows the scattering profile as a function of delay for the data file processed using both the matched filter and the MMSE GPR processor for the anti-tank mine TM-46. From Figure 6.5.2, it can be inferred that the target is at a delay of about 4.5 ns. The target can be more distinctly identified in the scattering profile obtained from the MMSE processing algorithm than from the matched-filter processing.

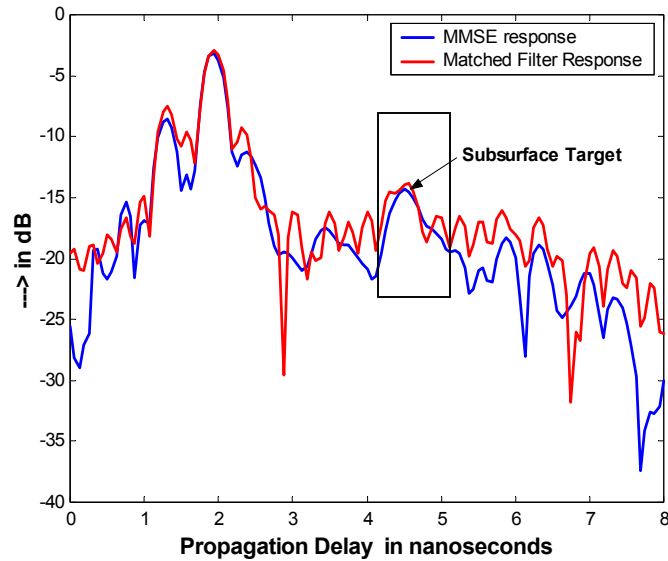


**Figure 6.5.2: MMSE GPR and matched-filter responses for TM-46, anti-tank mine. The target seems to be present at a delay equal to 4.5 ns.**

The MMSE filter reduces the effects of the dominant scatterer, i.e., ground, on the estimate of scattering from the subsurface target. The estimate errors in scattering from the subsurface target due to ground response can lead to an error in the symmetry measures. This needs to be avoided; the MMSE signal-processing algorithm can be used for this. This is why the  $m$  plot for the TM-46 was not reflecting low symmetry measures although the subsurface target could easily be detected from the sum plot. The  $m$  plot and sum plot for the TM-46 with matched-filter processing are shown in Figure 5.3.1.8. It will take much processing time to generate sum and  $m$  plots for the TM-46 with the radar responses obtained using the MMSE GPR processor.

Generally, the computation of the inverse is a time consuming operation (but it is required to implement the MMSE estimator). Especially in radar signal

processing, computing the inverse of large matrices can greatly slow down the processing speed. An iterative implementation of the MMSE algorithm can be developed where the radar data can be split into smaller segments to reduce processing time. Does an iterative algorithm help solve the problem of computational load and processing speed?

Another problem encountered with the MMSE GPR processor was that it could not distinguish the subsurface target from the ground response if the target was very close to the dominant scatterer (such as the one shown in Figure 6.4.2.3). Will an iterative algorithm provide better results than the MMSE GPR processor with regard to subsurface target detection in cases where the subsurface targets are buried at very shallow depths beneath the ground?

The Kalman filter algorithm, an iterative implementation of the MMSE algorithm, will be developed to answer these questions in the next chapter.

## Chapter 7

### Kalman Filter Implementation

The MMSE GPR processor has been proven as a potential solution for efficient detection of subsurface targets buried at shallow depths. But the computation of the inverse of large matrices slows down the processing speed of the algorithm. Is there a solution to improve the speed of the algorithm? By implementing an iterative algorithm and working on small pieces of data at a time, the computational load can be reduced.

In this chapter we develop a Kalman filter implementation of the MMSE signal-processing algorithm. The general concept of the Kalman filter and how it is useful for the application of subsurface target detection has been discussed in this chapter. As in the case of the MMSE GPR processor, simulations will be used in validating the Kalman algorithm. The performance of the Kalman filter algorithm will be compared to those of the matched filter and MMSE GPR processor (when the subsurface target is buried at very shallow depths beneath the ground).

#### 7.1 Kalman Filter Model

The iterative implementation of the MMSE GPR processor using the fundamentals of the Kalman filter will be developed in this section to address the problems of computational load and processing speed. The Kalman filter algorithm we develop will be validated using simulations and will be tested on measured data.

### 7.1.1 Fundamentals of Kalman Filter Algorithm

The Kalman filter algorithm is an iterative algorithm in which the estimate of the required parameter (state variable) is updated in every iteration using the new set of data. There are two fundamental equations that form the basis for the Kalman filter algorithm.

The state equation describes the relationship between the estimates of the state variable in successive iterations. The state equation is written as

$$\mathbf{x}(n+1) = \mathbf{A}(n)\mathbf{x}(n) + \mathbf{u}(n) \quad (7.1.1.1)$$

The matrix  $\mathbf{A}(n)$  is the state transition matrix, which reflects the changes in the value of the state variable  $\mathbf{x}(n)$  from an instant  $n$  to  $n + 1$ . The state transition matrix should be modeled perfectly so as to produce no errors in predicting the value of  $\mathbf{x}(n+1)$  using the available value of the state variable  $\mathbf{x}(n)$ . Any amount of accurate modeling of the state transition matrix will not reduce the prediction errors to zero. The term  $\mathbf{u}(n)$  added in (7.1.1.1) models the uncertainty in modeling the state transition information.

The other fundamental equation is the observation equation, which describes the observation vector. The observation vector in many cases is the data measured and is given by (7.1.1.2)

$$\mathbf{y}(n) = \mathbf{C}(n)\mathbf{x}(n) + \mathbf{n}(n) \quad (7.1.1.2)$$

where  $\mathbf{C}$  is a known matrix and  $\mathbf{n}$  is the noise associated with the observation. In 7.1.1.1 and 7.1.1.2 the variable  $n$  keeps track of the current iteration in the Kalman algorithm.

Using these two basic equations the Kalman filter algorithm is developed. The state equation and the observation equation have been described in general in this section. How can these fundamental equations be used to develop the Kalman filter algorithm for the problem at hand?

### 7.1.2 Kalman Filter Implementation

In this section the Kalman filter model specific to the applications in radar signal processing will be developed, and an iterative implementation will be proposed to address the issues of processing speed and computational load.

The main goal of implementing the Kalman filter is to reduce the time for computing the inverse of large matrices. For this reason the radar data are divided into smaller segments. Let the radar data be segmented into small sections with each section having  $N$  data points. The radar data are a function of frequency and therefore each segment of the data will have  $N$  frequency points of the measurement. Let  $n$  be the variable indexing the Kalman filter iterations.

The radar data, which are a superposition of the responses from the different range bins, can be compactly written in the form

$$\mathbf{r}(n) = \mathbf{P}(n)\boldsymbol{\gamma}(n) + \mathbf{n}(n) \quad (7.1.2.1)$$

where  $\mathbf{P}(n)$  is the normalized response matrix,  $\mathbf{n}$  is the noise associated with the radar measurement, and  $\boldsymbol{\gamma}(n)$  is the scattering coefficient. This equation, which models the radar data, is similar to the observation equation. Comparing (7.1.2.1) and (7.1.1.2),

it can be seen that the known matrix  $\mathbf{C}$  is the normalized response matrix that has been scaled down so that the matrix has  $N$  rows and, columns equal to total number of targets illuminated by the radar, the state variable  $\mathbf{x}(n)$  is the scattering coefficients ( $\gamma(n)$ ), and  $\mathbf{y}(n)$  represents the radar data ( $\mathbf{r}(n)$ ). The radar data  $\mathbf{r}(n)$  have  $N$  frequency points. Using the radar data, scattering as a function of delay needs to be estimated.

The state equation that describes the changes in the state variable from one iteration to another is given in (7.1.1.1). The state equation for the problem at hand, for which the state variable is the scattering coefficient, is expressed as

$$\gamma(n) = \mathbf{A}(n)\gamma(n-1) + \mathbf{u}(n) \quad (7.1.2.2)$$

where  $\gamma$  is the scattering and  $\mathbf{A}$  is the state transition matrix. The state variable in general changes with  $n$ . The state transition matrix expresses this change from  $n-1$  to  $n$ . For our problem, the index  $n$  corresponds to a different radar data segment or a change in the set of radar measurements. The radar measurement is a function of frequency. The scattering from the targets illuminated can be assumed to be constant between successive iterations. Owing to this fact, the state transition matrix can be considered to be an identity matrix.

Therefore the state equation can be written as

$$\gamma(n) = \gamma(n-1) + \mathbf{u}(n) \quad (7.1.2.3)$$

Hence the two fundamental equations, which are used to implement the Kalman filter for the problem of estimating the scattering as a function of delay, are the observation equation as in (7.1.2.1) and the state equation as in (7.1.2.3). The Kalman filter

process can be solved [9, 12] and the set of equations that implement the iterative Kalman filter algorithm, are shown in Figure 7.1.2.1.

$$1. \mathbf{K}_\gamma(n | n-1) = \mathbf{K}_\gamma(n-1 | n-1) + \mathbf{K}_u(n)$$

where  $\mathbf{K}_\gamma(n) = E\{\gamma(n)\gamma'(n)\}$  and  $\mathbf{K}_u(n) = E\{\mathbf{u}(n)\mathbf{u}'(n)\}$

$$2. \mathbf{G}(n) = \mathbf{K}_\gamma(n)\mathbf{P}'(n)[\mathbf{P}(n)\mathbf{K}_\gamma(n | n-1)\mathbf{P}'(n) + \mathbf{K}_n(n)]^{-1}$$

where  $\mathbf{K}_n$  is the noise covariance matrix and  $\mathbf{G}(n)$  is the Kalman gain.

3. The Innovation Process

$\mathbf{v}(n) = \mathbf{r}(n) - \mathbf{P}(n)\hat{\gamma}(n-1 | n-1)$  Using the scattering estimate of the previous iteration, an estimate of the data is evaluated for the next iteration. When the new data arrive the error between the new data and their estimate is the new information called **Innovation**.

4. The estimate of the scattering

$\hat{\gamma}(n | n) = \hat{\gamma}(n-1 | n-1) + \mathbf{G}(n)\mathbf{v}(n)$  This estimate is computed with the data  $\mathbf{r}(n)$ .

5. The updated target correlation matrix is

$$\mathbf{K}_\gamma(n | n) = [\mathbf{I} - \mathbf{G}(n)\mathbf{P}(n)]\mathbf{K}_\gamma(n | n-1)$$

**Initial conditions must be set to initiate the Kalman filter**

Figure 7.1.2.1: Iterative algorithm for Kalman filter processing.

The novel aspect of the Kalman filter algorithm is the concept of innovation. The estimate of the radar data  $\hat{\mathbf{r}}(n)$  for the  $n^{\text{th}}$  iteration is calculated using the scattering estimate from the previous iteration say,  $n-1$ , and the normalized response

matrix for the  $n^{\text{th}}$  iteration. When the next segment of radar data  $\mathbf{r}(n)$  arrives, the difference between the estimate from the previous iteration ( $\hat{\mathbf{r}}(n)$ ) and the new data is the new information or “innovation.” In every iteration, the innovation is calculated and is used in updating the estimate of the scattering coefficients. To start the iterative Kalman filter algorithm some initial conditions have to be set. Simulations have to be performed to validate the performance of the Kalman filter and to test whether an iterative algorithm helps in reducing the computation time. Simulation parameters and the initial conditions required to initiate the Kalman filter algorithm will be discussed in the next section.

## **7.2 Simulation and Results**

The motivation for implementing the iterative Kalman filter is to reduce the computation time of the inverse of large matrices. Simulations were performed to prove that the iterative algorithm helps in reducing the time required for processing. To perform simulations and to evaluate the performance of the algorithm, developing a simulation model is essential. This section will highlight the development of a simulation model for the Kalman filter implementation and also explain the results obtained from simulations.

### **7.2.1 Simulation Model**

In this section the different parameters used to set up the simulation are dealt with. The radar parameters used for the simulation are similar to those used for the MMSE GPR processor simulations. The bandwidth has been assumed as 4 GHz

spanning from 2 GHz - 6 GHz and the number of frequency points is set equal to 200. The value of 200 was chosen so the radar data, which are a function of frequency, can be easily split into smaller segments.

In addition to setting the radar parameters, the initial conditions under which to initiate the Kalman filter algorithm also must be defined. These are initial scattering vector  $\gamma$ , the initial target correlation matrix  $\mathbf{K}_\gamma$  and the error covariance matrix  $\mathbf{K}_u$ .

The initial scattering is set equal to zero. The scattering coefficients are a function of delay and will be a vector with a dimension equal to the number of targets illuminated.

Two definite regions have been defined for specifying the target correlation matrix; i.e., the ground and the subsurface target region. The initial target correlation matrix is a diagonal matrix. Since the user defines the energy scattered from the ground and the subsurface targets in the simulation, the diagonal elements of the target correlation matrix have been set at 10 dB greater than the actual values used for both the ground and the subsurface target regions.

The error covariance matrix is considered to be a diagonal matrix with the diagonal elements equal to the variance of the uncertainty. For the simulations, this variance has been assumed to be small and is equal to 0.01.

The radar data are simulated by extracting the normalized response for the delays corresponding to the specular and subsurface targets and scaling them with their respective scattering coefficients. The noise has been modeled as white Gaussian

noise with a very low variance. The value of the variance of noise used in the simulation is  $-50$  dB.

Using this model, simulations were performed to evaluate the performance of the Kalman filter algorithm.

### **7.2.2 Simulation Results**

The initial simulations were performed to prove that the iterative algorithm will reduce the computation time, thereby increasing the processing speed. Simulations were conducted in which the radar data were segmented into smaller sections with each section having a set of frequency points. The number of frequency points in each section was varied from 1 (smallest segment) to 200 (the available data are considered to be one big segment). The total number of iterations the algorithm must run through is equal to the total number of frequency points divided by the number of frequency points in each radar segment.

We could see from the simulations performed that, as the number of iterations increases, the time required to complete the iterative algorithm first drops and then increases. The time to complete the algorithm initially reduces because the inverse must be computed for matrices that are smaller in dimension than if the whole radar data were considered to be a single segment. As the number of iterations increases, which implies that the radar data segments are becoming smaller in dimension, the time taken to compute the inverse reduces. However, the number of computations to complete the algorithm increases, thereby increasing the total time required to complete the iterative algorithm. To test the performance of the Kalman filter with

regard to target detection, we had to decide the optimum number of iterations for performing the simulations.

A simulation was performed with the ground at 2.2 ns with a scattered energy of 30 dB and the subsurface target at 4.3 ns with the energy scattered from it being equal to -15 dB. The variance of noise in the simulation was set equal to -50 dB. The initial conditions for the iterative algorithm were set as described in Section 7.2.1. The simulation was performed for cases where the number of frequency points in the radar data segment varied from 1 to 200 (specific values for the length of the radar data segment are 1, 2, 10, 50, 100 and 200), which means the number of iterations to complete the iterative algorithm vary from 200 to 1 (200, 100, 20, 4, 2 and 1 iterations respectively). The radar response as a function of delay using the Kalman filter algorithm for a specific length of radar data segment is the scattering estimate at the end of all the iterations as a function of propagation delay. The radar responses for different cases (different radar data segment lengths) were considered and are shown in Figure 7.2.2.1.

It can be inferred from Figure 7.2.2.1 that the scattering profile for the simulation in which the length of the radar data segment was equal to one gave good results when compared to all other cases with regard to subsurface target detection. The subsurface target is distinctly seen and clearly distinguished from the noise floor.

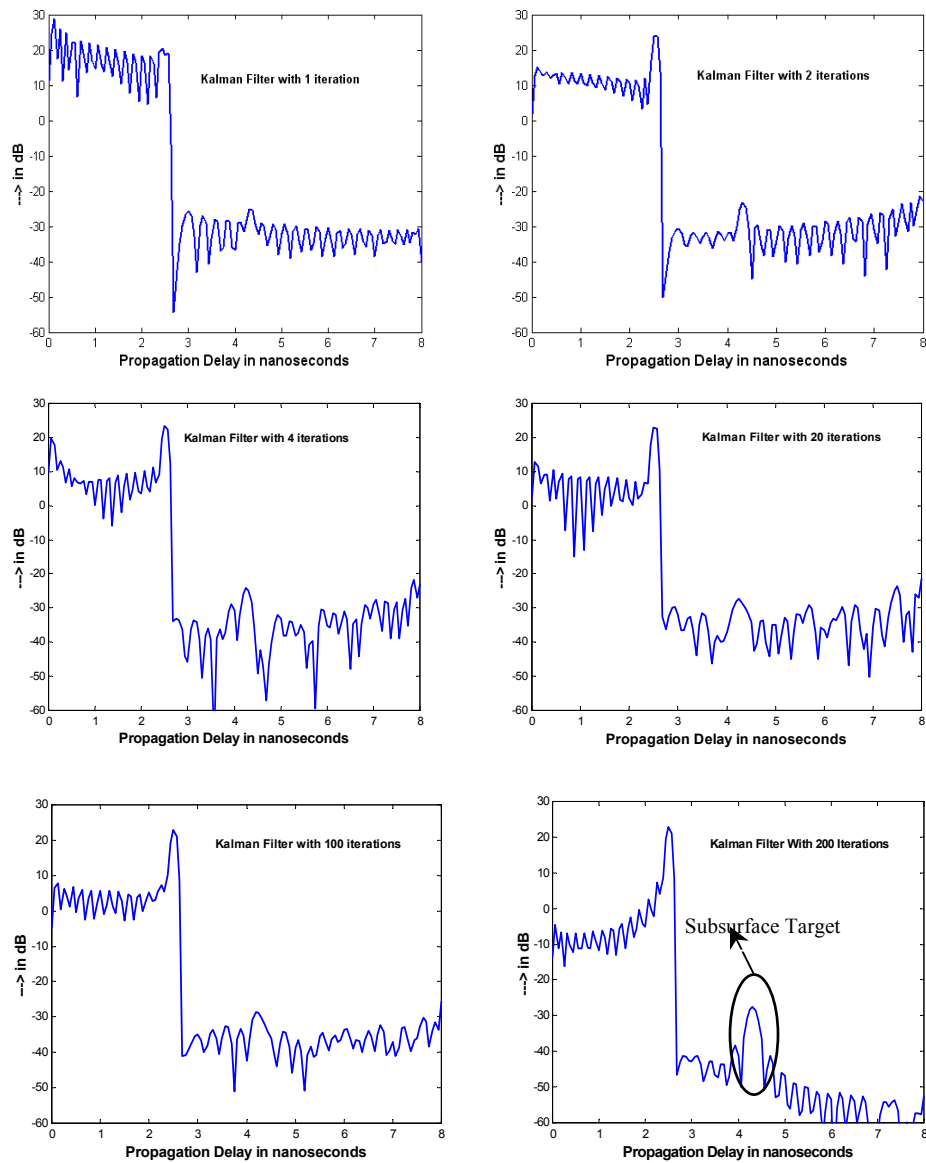


**Figure 7.2.2.1: Results of Kalman filter processing as a function of numbers of iterations. The number of frequency point in a single radar data segment changes with the number of iterations. Optimum number of data points in the radar data is 1.**

Using the information gathered from the experiments conducted, a simulation was performed to compare the performance of the matched filter and the Kalman filter with regard to detection of shallow subsurface targets.

The ground is at 2.2 ns and subsurface target at 3 ns. The energy scattered from the ground is equal to 30 dB and the energy scattered from the subsurface target is set to 0 dB. The initial conditions for the simulations were set using the description in Section 7.2.1. Each segment of data has one frequency point. Figure 7.2.2.2 shows the scattering profile as a function of propagation delay for different signal-processing algorithms; i.e., matched filter, Kalman filter, and the matched filter with prior windowing of the frequency-domain data with Blackman and Hamming windows.

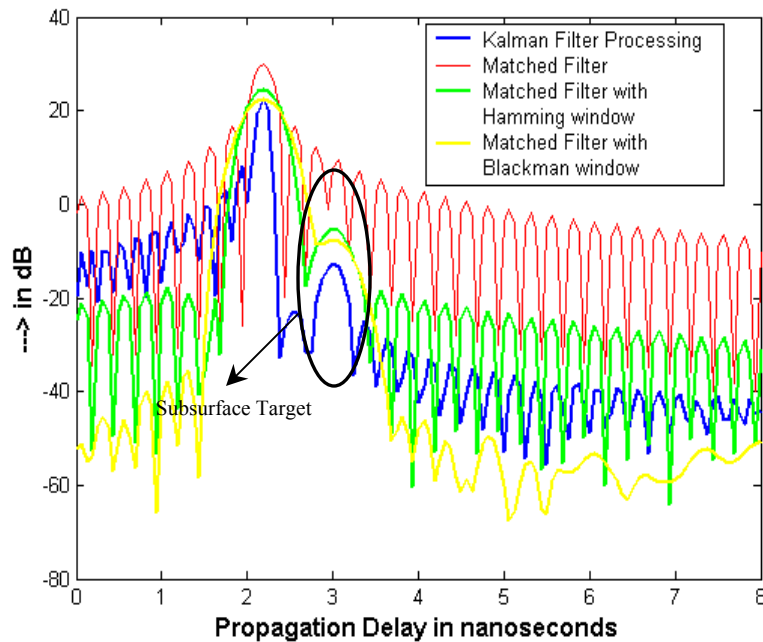


**Figure 7.2.2.2: Performance of Kalman filter compared to matched filter and matched filter with prior windowing of the frequency-domain data with Hamming and Blackman windows. Target at a delay of 3 ns.**

The performance of the Kalman filter is better than the matched filter. The time-domain side lobes of the ground response mask the response from the subsurface

target in the matched filter. To suppress the time-domain side lobes, the windowing technique was investigated. The windowing technique also proves effective (only in the case of a Hamming window) as the subsurface scatterer is not very close to the ground. In the case of Blackman window, the main lobe almost masks the subsurface target. The value of the scattering estimates from the Kalman filter processing is not close to the actual values of the subsurface target or the ground. There is an estimate error due to the Kalman filter but the subsurface target can be easily detected.

One of the motivations for investigating the option of an iterative implementation of the MMSE GPR processor is whether the Kalman filter helps in improving the target detection, especially when the subsurface targets are buried at very shallow depths beneath the ground. The MMSE GPR processor (as detailed in the Chapter 6) was not able to distinguish between the ground and the subsurface target when the subsurface scatterer was very close to the dominant scatterer. How does the Kalman filter perform in this case? The simulation with the ground at 2.2 ns and the target at 2.75 ns was performed using the Kalman filter. The scattered energy from the ground was set equal to 30 dB and the scattered energy from the subsurface target at 0 dB. The Kalman filter algorithm was initiated and the scattering as a function of delay at the end of all the iterations is shown in Figure 7.2.2.3. The scattering profile obtained from the Kalman filter is compared with that obtained from the matched filter. From Figure 7.2.2.3 it can be inferred that the Kalman filter is robust enough to detect the target that is buried at very shallow depths beneath the

ground. It can be seen that the option of using Hamming and Blackman windows to suppress the time-domain side lobes is inferior to using the Kalman filter. The poor

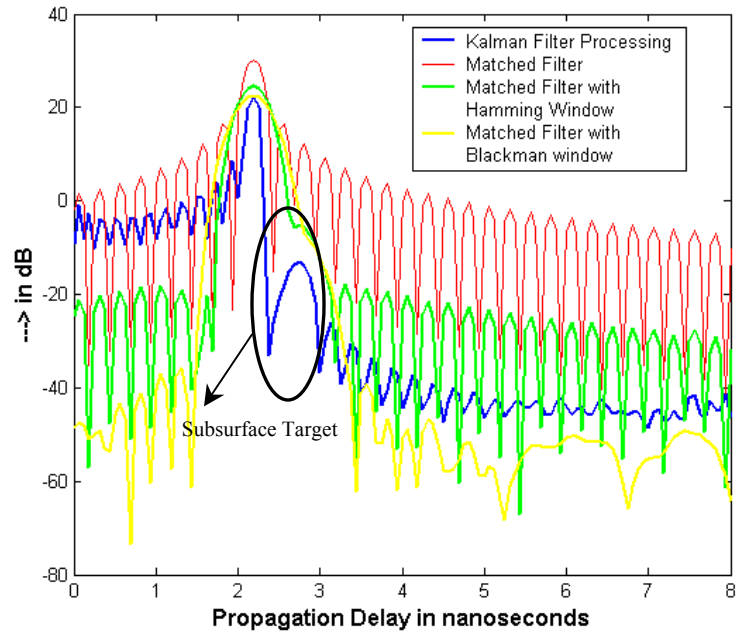


**Figure 7.2.2.3: Comparison of Kalman filter response with matched filter and matched filter with prior windowing of the frequency-domain data with Hamming and Blackman windows. Target at a delay of 2.75 ns.**

performance of the windowing can be attributed to the degradation of resolution and, with subsurface target very close to the dominant scatterer, the broadening of the main lobe masks the subsurface target.

Thus, the simulations performed revealed that the Kalman filter performance is superior to that of the matched filter, and it also performs better when compared to the MMSE GPR processor with regard to detection of subsurface objects at very shallow depths. Another important conclusion from the simulations is that the

iterative algorithm with a single data point (only one frequency point) in each radar data segment gives good results with regard to subsurface target detection.

The simulations performed validated the Kalman filter algorithm; now it must be tested on measured data.

### **7.3 Kalman Filter Processing on Measured Data**

Having developed the Kalman filter model using the state equation and the observation equation and also having validated the iterative implementation using simulations, the Kalman filter performance needs to be tested on measured data. The number of iterations that have to be performed before the algorithm converges to a good solution has been shown (in Section 7.2.2) to be equal to the total number of data points in the radar data (which means that each segment of the radar data has only one frequency point).

The data set that was selected for processing was collected on a TM-46, an anti-tank mine from the Virginia field experiment (the anti-tank mine that started our investigation into development of a better signal-processing algorithm than the matched filter). The ground region is from 0 ns to 2.2 ns and the subsurface target region is from 2.2 ns to 8 ns. The estimates of the energy scattered from the ground and the subsurface target are set using the matched-filter response. The rough estimates of the scattering from the ground and the subsurface targets are  $-5$  dB and  $-15$  dB, respectively. The estimates of the scattered energy given to the diagonal elements of the initial target correlation matrix (for initiating the Kalman filter

algorithm) in the specular and subsurface target regions are 10 dB higher than the rough estimates obtained using the matched-filter response. The Kalman filter processing was performed and its response is compared with the matched-filter response in Figure 7.3.1.

It can be seen from Figure 7.3.1 that the Kalman filter performance is superior to that of the matched filter with regard to subsurface target detection. The Kalman filter suppresses the time-domain side lobes, and the target can be seen distinctly at a delay of about 4.5 ns. Therefore the processing on the measured data as well as

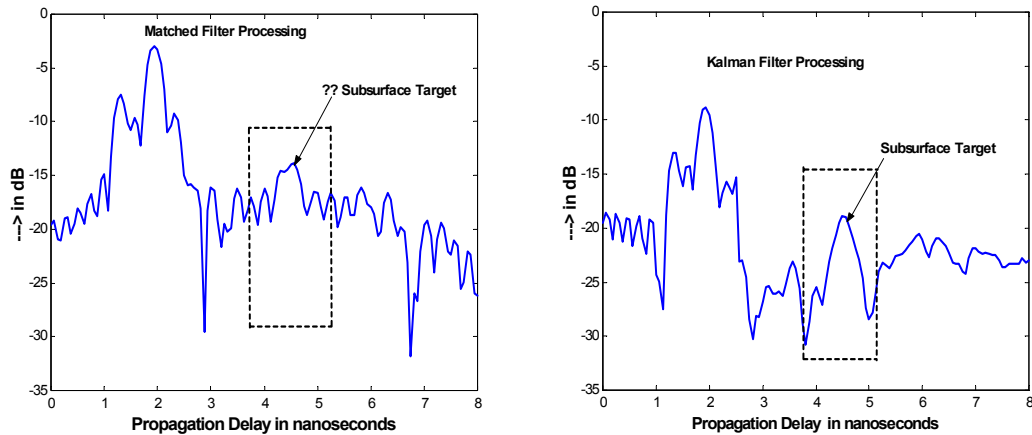


**Figure 7.3.1: Comparison between Kalman filter and matched-filter response for TM-46, an anti-tank mine from the field experiment.**

simulated data revealed that the Kalman filter algorithm’s performance is superior to the matched filter’s.

All the data files for the anti-tank mine (i.e., TM-46 from the Virginia field experiment) were processed using the Kalman filter algorithm. Using the radar responses (as a function of delay) obtained from the Kalman filter, the  $m$  plot and the

sum plot were generated using the sum and  $m$  value matrices (with a single-element sensor array) as detailed in Chapters 4 and 5. The sum and  $m$  plots generated using the Kalman filter and matched filter (with a Hamming window on the frequency-domain data) are compared in Figure 7.3.2.

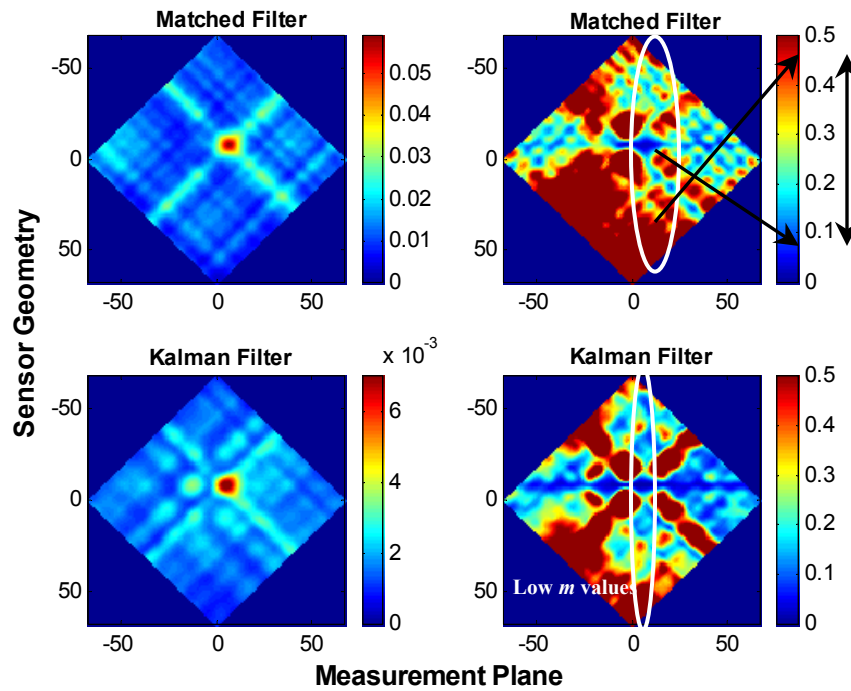


**Figure 7.3.2:** Comparison of sum and  $m$  plots obtained from Kalman and matched-filter processing. The  $m$  plot for the Kalman filter has low  $m$  values, indicating that the target is symmetric.

The  $m$  plot generated using the Kalman filter processing exhibits a distinct measurement plane with low symmetry measures for almost all the sensor geometries, which is not present in the  $m$  plot generated using the matched-filter processing. The performance improvement due to the Kalman filter with regard to extracting symmetry information from subsurface targets can be more clearly observed in the cascade plots for the  $m$  value matrices as shown in Figure 7.3.3.

From Figure 7.3.3 we can see that the measurement plane for which the  $m$  values for almost all sensor geometries are low can be seen more distinctly in the

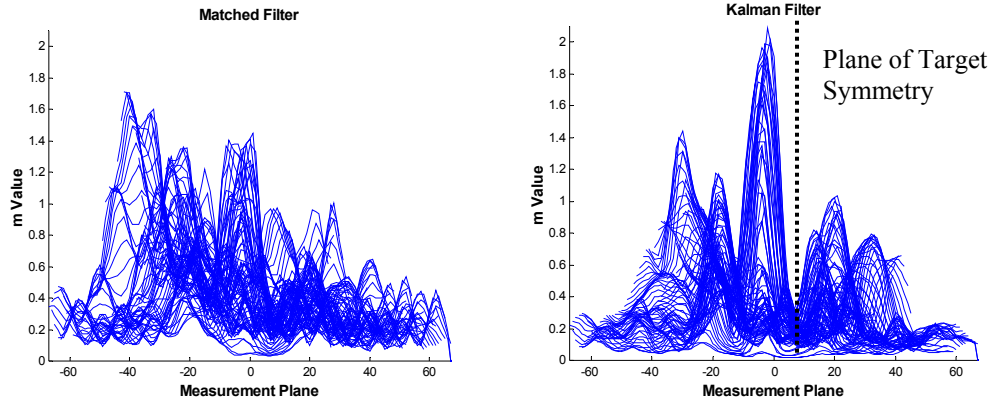


**Figure 7.3.3: Cascade plot of  $m$  values for TM-46 with matched filter and Kalman filter. A deep null can be seen in the cascade plot using Kalman filter, indicating that the target is a mine.**

cascade plot generated using the Kalman filter than in the cascade plot generated using the matched filter. Moreover, decisions based on use of the  $m$  plot and the cascade plot for  $m$  value matrices generated using the matched filter can lead to a significant probability of missed detection.

The improvement in performance due to the Kalman filter processing can be attributed to the fact that the Kalman filter suppresses the time-domain side lobes from the dominant scatterer, thereby minimizing the estimate errors due to the ground response while estimating the scattering from the subsurface target. In other words the Kalman filter maximizes the signal-to-interference ratio. Since the matched filter does not maximize SIR, it can lead to estimate errors and hence can lead to erroneous symmetry measures as discussed in the case of the TM-46 anti-tank mine.

A Kalman filter implementation of the MMSE GPR processor was developed to increase processing speed by reducing computation time for computing the inverse of matrices (by reducing the size of the matrix). But optimum performance with respect to subsurface target detection was achieved only when the radar data segment had only one frequency point. This means that the Kalman filter must go through the maximum number of iterations possible for given radar data before it generates good results.

It has been validated through simulations that the Kalman filter algorithm performs better than the matched filter with regard to target detection. It also performed better than MMSE GPR processor when the target was buried at very shallow depths beneath the ground. The validated algorithm was tested on measured data. TM-46 data, an anti-tank mine from the Ft. A.P. Hill, Virginia field experiment, were processed using the Kalman filter. The Kalman filter processing was seen to yield better symmetry measures than the matched filter. This improvement can be attributed to the fact that the Kalman filter reduces the effect of the ground response on the subsurface target signature.

## Chapter 8

### Conclusions and Future Work

#### 8.1 Summary

It has been proved by the experiments conducted and the results presented in this thesis that ground penetrating radar can be used for developing an efficient landmine detection scheme that exploits the property of reflection symmetry present in almost all the landmines buried across the world. The possibility of deploying the landmine detection scheme in the minefield based on a hand-held model has been investigated. The results shown in Chapter 5 indicate that the simple hand-held model we developed gave conclusive results with regard to subsurface target detection and classification in both laboratory and field experiments. The hand-held model could be implemented commercially with accurate positioning systems.

The need for better signal-processing algorithms than the conventional matched filter (correlator) for the application of detecting shallow subsurface targets has been investigated. A robust signal-processing algorithm based on the MMSE criterion has been developed, validated using simulations, and tested on measured data. The MMSE GPR processor performs better than the matched filter with regard to detection of shallow subsurface targets. To address the shortcomings in the MMSE GPR processor, an iterative implementation of the MMSE processor based on the principles of a Kalman filter was developed and tested. The Kalman filter performs better than the matched filter. It also performs better than the MMSE GPR processor,

especially in the case where the target is at a very shallow depth (a depth corresponding to a delay of 0.5 ns later than the dominant scatterer).

Therefore, with *a priori* knowledge of the scattering scenario, it has been proved that signal-processing algorithms can be developed for the detecting shallow subsurface targets that perform better than the conventional matched filter.

## 8.2 Suggested Future Work

To implement the highly efficient data collection scheme that helps synthesize a hand-held detector, an accurate positioning system is needed. This is a requirement for good results, as any positioning error can destroy the symmetry in the measurements and hence lead to erroneous results. As future work the antennas could be attached to the arms of a robot that can scan from one end of a minefield to the other with accurate positioning.

An assumption made during the Kalman filter implementation was that the scattering coefficient  $\gamma$  (state variable) was assumed to be constant between iterations. Using this assumption, the state transition matrix was modeled as an identity matrix. Is this assumption reasonable? In the Kalman filter implementation, each radar data segment consisted of radar measurements for a few frequencies. The total length of radar data (used in the simulations) had 200 frequency points in the bandwidth from 2 GHz – 6 GHz. If the radar data were divided into four segments, each radar data segment would span a frequency of 1 GHz and if the radar data were divided into 200 segments, each radar data segment would span 0.02 GHz. The assumption that the

scattering coefficient is constant between iterations is valid more when the radar data segment corresponds to a small span in frequency than when it corresponds to a span in frequency on the order of 500 MHz or 1 GHz. This might be the reason why the Kalman filter gave optimum performance with regard to subsurface target detection when the radar data segment had only one frequency point (which means each radar data segment corresponded to a frequency span of 20 MHz). The scattering coefficient does not change appreciably for a 20 MHz change in frequency in the bandwidth of interest (2 GHz to 6 GHz). As future work, the state transition matrix could be modeled differently to incorporate the variations in scattering coefficients as a function of frequency.

One of the problems with the Kalman filter algorithm implemented in this thesis is that it was not able to produce accurate estimates of scattering from the ground and the subsurface targets, though its performance was superior to the matched filter with regard to subsurface target detection. On the other hand, the MMSE GPR processor gave accurate scattering estimates but was not able distinguish targets buried at very shallow depths beneath the ground. As future work, a combination of the MMSE GPR processor and the Kalman filter algorithm could be implemented to get the best out of both processing algorithms.

### **8.3 Conclusions**

The model for the compact landmine detector developed in this thesis is essential for successful deployment of the detection scheme in the minefield. The

detection scheme proposed uses the feature of reflection symmetry in the landmines, which is absent in clutter targets. Therefore, the detection scheme we developed is independent of the shape and size of the mine, the casing of the mine, metal content in the mine, chemicals used as explosives in the mine, depth at which the mine is buried, and soil characteristics. This suggests that the detection scheme we developed as part of this research effort has a potential of low  $P_{FA}$ . The results obtained from different experiments suggest that the compact hand-held detector we proposed, along with the detection scheme (which has a potential of low probability of false alarm), could well be one of the key developments to boost the global effort for a world free of the *Hidden Killers*.

## References

- [1] Office of Humanitarian Demining Programs, *Hidden Killers: The Global Landmine Crisis*, Report by United States Department of State, Bureau of Political-Military Affairs,  
[http://www.state.gov/www/global/arms/rpt\\_9809\\_demine\\_toc.html](http://www.state.gov/www/global/arms/rpt_9809_demine_toc.html),  
September 1998.
- [2] U.S. Army Mobility Equipment Research and Development Command, *MERADCOM Mine Detection Program: 1960-1980, A Technical Report*,  
March 1980, Fort Belvoir, VA 22060.
- [3] <http://www.unfoundation.org/campaigns/landmines/index.asp>
- [4] James. M. Stiles, Abhijit Apte and Beng Beh, “A Group Theoretic Analysis of Symmetric Target Scattering with Application to Landmine Detection,” *IEEE Trans. Geoscience and Remote Sensing*, vol.40, no.8, pp.1802-1814, 2002.
- [5] Abhijit Apte, “Landmine Detection Using Ground Penetrating Radar,” *M.S. Thesis*, The University of Kansas, August 2000.
- [6] Merrill. I. Skolnik, *Introduction to Radar Systems*, New York, NY, McGraw Hill, 2001.
- [7] Keigo Lizuka, Alois. P. Fruendorfer, Kam Hung Wu, Hirotaka Mori, Hisango Ogura and Van-Khai Nguyen, “Step-Frequency Radar,” *Journal of Applied Physics*, vol.56, no.9, pp.2572-2583, November 1984.
- [8] <http://angola.npaid.org>

- [9] K. Sam Shanmugan and A. M. Breipohl, *Random Signals: Detection, Estimation and Data Analysis*, New York, NY, John Wiley & Sons, Inc., 1988.
- [10] Nathan Goodman and James M Stiles, "A MMSE Filter for Range Side Lobe Reduction," *Proceedings of the IEEE International Geoscience and Remote Sensing Symposium*, Honolulu, Hawaii, vol.5, pp. 2365-2367, July 2000.
- [11] James. M. Stiles, Nathan Goodman and Guruvayurappan, "Minimum Mean-Squared Error GPR Processor for Resolving Shallow Objects," *Proceedings of the SPIE Conference on Detection and Remediation of Mines and Minelike Targets*, SPIE, vol.4394, Orlando, Florida, pp.797-805, April 2001.
- [12] Simon Haykins, *Adaptive Filter Theory*, Upper Saddle River, NJ, Prentice Hall, 2001.